

Lyman- α transmission spikes as probes of cosmic voids, the intergalactic medium, and reionization

MASTER'S THESIS

for acquisition of the academic degree

Master of Science

in the Master's program

Astrophysics

Submitted by

Fabian Pascal Emmerich

Produced at

Institute of Physics and Astronomy

Supervisor

Prof. Dr. Christoph Pfrommer

Second Referee

Prof. Dr. Philipp Richter

Assisting Supervisor

Dr. Ewald Puchwein

Potsdam, March 5, 2021

Abstract

The large cosmic voids which evolved between galaxies embedded in filaments and clusters are a fundamental part of the formation of large-scale structures as we observe them in the present Universe. Lyman- α ($\text{Ly}\alpha$) forest spectra of high-redshift quasi-stellar objects (QSOs) might enable probing intergalactic gas residing in cosmic voids near the Epoch of Reionization – a phase in the early Universe in which the cosmic gas transitioned from entirely neutral to being almost fully ionized. We use data from a selection of runs of the SHERWOOD RELICS simulation suite to investigate cosmic voids and the intergalactic medium (IGM) during and immediately after the Epoch of Reionization from transmission spikes in synthetic $\text{Ly}\alpha$ spectra of QSOs. The runs deploy different assumptions such as patchy and homogeneous ultraviolet radiation backgrounds, varying IGM temperature, and photoionization and -heating rates. We construct and analyze mock $\text{Ly}\alpha$ spectra along 5 000 random lines of sight (LOSs) through each simulation box at different redshifts $z = (5.0 - 6.4)$. Along these LOSs, we detect all transmission spikes and underdense regions and their properties (width and height), and extract the gas properties in the areas of the IGM which produce the spikes. For the spike width measurement we employ a fixed flux threshold, whereas for the underdensity widths we use an adaptive, redshift-dependent threshold. We find a linear correlation with slope ~ 1 between spike and underdensity widths along the LOS. By investigating the contribution of individual locations to absorption in underdense regions, we infer that $\text{Ly}\alpha$ transmission spikes probe the central contents of voids with a growing contribution by outer regions with increasing IGM temperature. Spike widths show a weak, negative correlation to the density and neutral hydrogen fraction of the IGM, whereas spike heights show a strong negative correlation to both quantities. Adding realistic noise as present in observational data corresponding to a signal-to-noise ratio $S/N = 30$ does not significantly affect our results. $\text{Ly}\alpha$ transmission spikes are hence a powerful tool to study the properties of cosmic voids and their gas contents.

Contents

1	Introduction	7
2	Theoretical background	11
2.1	Cosmic structure formation	11
2.1.1	The homogeneous universe	11
2.1.2	The inhomogeneous universe	12
2.2	Cosmic voids	14
2.2.1	Void properties	14
2.2.2	Density and velocity profiles of voids	15
2.2.3	Void evolution	17
2.3	The intergalactic medium and its reionization	18
2.3.1	Reionization of the cosmic gas	18
2.3.2	Observables of the high-redshift universe	19
2.3.3	Sources of ionizing radiation	20
2.3.4	Radiation background modeling in cosmological simulations	21
2.3.5	Thermal evolution	22
2.4	Quasar absorption systems	23
2.4.1	The Lyman- α forest	24
2.4.2	Broadening of spectral lines	26
2.4.3	Optical depth of a gas cloud in the IGM	29
3	The SHERWOOD RELICS simulations	31
3.1	Properties of the simulations	31
3.2	Homogeneous and patchy UVB models	33
3.3	Available simulation data	35
4	Methods	37
4.1	Synthetic quasar spectra	37
4.2	Scaling the spectra to observed effective optical depths	38
4.3	Measuring transmission spike and underdensity properties	40
4.3.1	Detection criteria	40
4.3.2	Detection algorithm	41
4.3.3	Connecting spikes to the transmitting, underdense regions	41
4.4	Using a fixed threshold for spike and a dynamical for underdensity width measurement	43
4.5	Adding noise to create realistic spectra	46

5	Results	49
5.1	Evolution of transmission spike number density and neutral hydrogen fraction	49
5.2	Contribution of individual pixels to absorption in underdensities	52
5.3	Properties of transmission spikes and underdense regions	61
5.4	Relation of spike and underdensity widths	63
5.5	Comparing patchy and homogeneous UVB models	65
5.6	Influence of IGM temperature	70
5.7	Effect of ionization history and mean transmission on spike properties . .	74
5.8	Impact of realistic noise on the results	78
6	Summary and discussion	81
	Bibliography	85
	Appendices	95
A	Spike and void width distribution	97
B	Relation between spike shapes and gas properties	99

Chapter 1

Introduction

During the history of the Universe, the baryonic matter created shortly after the Big Bang has gone through various stages until it evolved into its present state. According to estimates, more than 99% of the observable matter in the cosmos is ionized (Kallenrode 2004; Gurnett & Bhattacharjee 2005) and resides in filaments and clusters embedded in the cosmic web. The empty regions between these structures – the *cosmic voids* – account for most of the spatial volume. When the Universe was still relatively young, though, this matter was predominantly neutral and almost perfectly uniformly distributed. The questions of how, when, and why this transition took place is crucial to understanding structure formation during the evolution of the cosmos.

Throughout its early evolution, while being extremely dense and hot, the Universe was still opaque when leptons (mainly electrons) and quarks were created. The latter later formed hadrons (mainly protons and neutrons) as the Universe expanded and cooled. When the temperature dropped below ~ 3500 K, atomic nuclei (consisting of protons and neutrons) and electrons almost fully recombined to form the first atoms, predominantly hydrogen and helium. This event is known as Cosmic Recombination and took place roughly 380 000 years ($z \approx 1100$, Planck Collaboration et al. 2018) after the birth of the Universe. Its aftermath, the Cosmic Microwave Background (CMB), can still be observed today and was first discovered in 1965 (Penzias & Wilson 1965; Dicke et al. 1965). As inferred from CMB anisotropies, the matter distribution in the cosmos at the time of recombination was almost perfectly homogeneous (Sachs & Wolfe 1967; Smoot et al. 1991, 1992). With recombination fading, the Universe became transparent to photons as it transitioned into the dark ages (Rees 1997), where the cosmic gas was predominantly neutral. This era ended with the formation of the first luminous astronomical objects such as stars and quasi-stellar objects, i.e. quasars (QSOs), in the first galaxies, which originated from matter being evacuated from less dense regions hence aggregating in structures enclosed in the filaments and galaxy clusters of the cosmic web. Eventually, initially less dense areas had developed into extremely large voids.

In order to reionize neutral hydrogen (HI) by overcoming its binding energy, electromagnetic radiation with an energy above 13.6 eV is needed to dissolve atoms into protons and free electrons. Ultraviolet (UV) photons from stars in the first star-forming galaxies likely provided the necessary radiation which continuously started to reionize their surrounding gas (Bolton et al. 2005; Faucher-Giguère et al. 2008; Becker & Bolton 2013; Ferrara & Pandolfi 2014). Other objects such as QSOs (Shapiro et al. 1994; Willott et al.

2010; Masters et al. 2012; Kulkarni et al. 2019b) and X-ray binaries (Eide et al. 2018) seem to have marginally contributed to this process at $z > 5$. With the density of H I dropping, the gas became increasingly penetrable for the ionizing UV radiation. Consequently, it could reach further and further out into their surrounding medium, forming growing bubbles of ionized gas. Additionally, with the Universe aging, more and more galaxies hosting star-forming regions formed. These processes continued until the bubbles began to overlap and, eventually, the cosmic gas became almost entirely ionized. This phase of the Universe in which the cosmic gas went from neutral to being virtually fully ionized is called the *Epoch of Reionization* (EoR).

Observations of CMB anisotropies constrain the mid-point redshift of cosmic reionization to be $z \approx (7.7 \pm 0.7)$ (Planck Collaboration et al. 2018) while the study of spectra from high- z QSOs with redshifts up to $z \approx 6.42$ suggest that the process completed at $z \approx 6$ (Fan et al. 2006; Schroeder et al. 2013; McGreer et al. 2015) and may possibly even have lasted until $z \lesssim 5.5$ (Kulkarni et al. 2019a). Thus, the EoR probably lasted from $z \approx (5.5 - 10)$ if its progress was symmetric. The study of absorption lines in the spectra of distant QSOs has proven to be a very powerful tool to investigate the properties of the intergalactic medium (IGM) along the lines of sight (LOSs) towards them. However, the study of absorption lines also encounters difficulties.

QSOs are surrounded by extremely hot, luminous accretion discs and are among the most luminous sources to be found in the cosmos (Padovani et al. 2017). These accretion discs produce a continuum emission which continuously redshifts through the Lyman- α ($\text{Ly}\alpha$) transition at $\lambda = 1215.67 \text{ \AA}$ as it propagates towards an observer. While traveling, the spectrum interacts with intervening gas (e.g. intergalactic gas or galaxy halos) with a fraction of the emission getting absorbed depending on the density of neutral hydrogen in the gas. In fact, the cross-section of $\text{Ly}\alpha$ absorption is so high that even very small amounts of H I cause strong absorption features in the spectrum (Meiksin 2009). Due to the continuous redshifting, these absorption lines appear at different wavelengths in the spectrum depending on the spatial position of the absorbing systems along the LOS. Since the number density of intervening $\text{Ly}\alpha$ absorbers grows with increasing redshift (i.e. distance), the spectra of high- z QSOs show many different H I absorption lines. This prominent feature is known as the $\text{Ly}\alpha$ forest (Weymann et al. 1981).

During the EoR, the neutral gas fraction was still relatively high even towards its tail end. Therefore, emission of high- z QSOs is so strongly absorbed by intermediate gas that almost no absorption features can be identified in their spectra. Instead they show only very few regions where parts of their light was transmitted. These are visible as spikes: the so-called *Ly α transmission spikes*. Such spikes are traces of areas along the LOS where the gas density and neutral gas fraction is particularly low (Barnett et al. 2017; Chardin et al. 2018; Keating et al. 2020). Hence, the $\text{Ly}\alpha$ forest at redshifts shortly after the completion of the cosmic reionization process provides an opportunity to directly observe the most underdense regions of the Universe, i.e. cosmic voids. Voids can be studied with the aim of inferring the gas properties within them or, e.g., confirming whether their properties agree with the expectations of cosmological models such as the Λ cold dark matter (Λ CDM) theory, which proposes the existence of cold dark matter and a cosmological constant. Furthermore, they can be used to investigate the properties of the IGM during the reionization era.

In addition to this, there are other techniques that may be useful to study cosmic voids.

Alonso et al. (2018), for example, used the thermal Sunyaev-Zeldovich effect (Sunyaev & Zeldovich 1972), which describes the spectral distortion of CMB photons due to inverse Compton scattering off of hot high-energy electrons. They measured the relative signal between voids and filaments or walls. However, since the absolute signals are unknown, and the signal in voids is very weak, this technique does not allow any constraints about voids. Furthermore, recent studies have shown that matter underdensities acting as gravitational lenses can be investigated through their lensing signals, although only when averaging over a large sample of voids (Melchior et al. 2014; Sánchez et al. 2017; Vielzeuf et al. 2021). Void lenses are therefore not eligible to study individual voids in detail. Other observables such as Ly α absorption lines at lower redshifts probe dense gas systems such as clouds, galaxies, or galaxy halos. Ly α transmission spikes, however, result from areas with very low density, which applies for central regions of voids. This makes them a very promising tool to study cosmic voids and, thereby, the state of the IGM during reionization. In fact, Ly α transmission spikes in high- z QSO spectra are likely to be the only observable of cosmic void contents.

Previously, Garaldi et al. (2019) investigated synthetic Ly α quasar spectra at $z > 5$ extracted from radiation-hydrodynamic simulations from the Cosmic Reionization On Computers (CROC) suite of Gnedin (2014) (see also Gnedin & Kaurov 2014) to study Ly α transmission spikes. In particular, they focused on whether they could find any connection of the spike shapes to the properties of the IGM and their potential ability to constrain reionization models. According to their results, the height of a spike correlates with the gas density and ionization fraction of the spike-producing regions. Furthermore, they find a linear, redshift-dependent correlation between spike width and width of the underdense regions along the LOS, which declines with redshift.

In this work, we use cosmological simulations from the SHERWOOD RELICS suite by (Puchwein et al. 2021 in prep., also see Gaikwad et al. 2020) to investigate the end of the EoR using Ly α transmission spikes in synthetic, high- z QSO spectra in the redshift range $5.0 \leq z < 6.5$. For three redshift bins $6.0 \leq z_1 < 6.5$, $5.5 \leq z_2 < 6.0$, and $5.0 \leq z_3 < 5.5$, similarly to Garaldi et al. (2019), we survey whether the shape of spikes is connected to the extent of the underdense regions generating the spikes and the gas properties in these voids (i.e. the IGM). By comparing different simulations with varying conditions such as UV background (UVB), IGM temperature, and photoionization and -heating rate, we probe how they affect spike shapes and their relation to the gas properties. We also investigate which parts of voids contribute to the transmission of flux and how this changes for different IGM temperatures. By studying the impact of realistic noise on our results, we check whether the methods we use for idealized simulation data are also applicable to real observations of the Ly α forest during the tail end of HI reionization. While generally speaking about “reionization”, we only focus on HI reionization.

The thesis is organized as follows: in Chap. 2 we provide the theoretical background to this work, and answer the questions: how are areas almost completely devoid of gas produced, what are their observed properties and dynamics, and how can they be used to understand the formation of cosmological structures and cosmic reionization. In Chap. 3, the SHERWOOD RELICS simulations will be explained in more detail. The construction and analysis of synthetic spectra, and how we detect spikes and underdensities along each LOS is described in Chap. 4. Finally, we elaborate and discuss the results of our aims in Chap. 5 and 6, respectively.

Chapter 2

Theoretical background

In this chapter, we will begin by discussing the emergence of cosmic voids in the context of cosmological structure formation in Sect. 2.1. Then, we will focus on cosmic voids and their properties in particular, and how they serve to study cosmological problems in Sect. 2.2. The major physical processes in the (post-)reionization IGM and the sources of reionization will be discussed in Sect. 2.3. In Sect. 2.4, we will explain the origin of the Ly α forest appearing in QSO spectra and its importance for studying regions with low H I column densities, i.e. the IGM and cosmic voids.

2.1 Cosmic structure formation

Two of the fundamental assumptions of cosmology are that the Universe is homogeneous and isotropic. Here, homogeneity implies that, on sufficiently large scales, matter in the Universe is uniformly distributed. The measure for the homogeneity of the matter distribution is the density deviation from the average density in the Universe at a certain position, which is given by the density contrast

$$\delta = \frac{\delta\rho}{\rho} = \frac{\rho - \bar{\rho}}{\bar{\rho}} = \Delta_b - 1, \quad (2.1.1)$$

where $\bar{\rho}$ is the mean matter density of the Universe and Δ_b the baryon density in units of the cosmic mean. Meanwhile, isotropy describes that, independent of the position of an observer, the Universe looks identical in all directions, i.e. measured large-scale quantities are equal in every direction. Under these two assumptions the dynamics of the Universe are described by the Friedmann equations.

2.1.1 The homogeneous universe

The discovery and subsequent measurements of the CMB revealed that the Universe was almost perfectly homogeneous at the time of cosmic recombination – also known as the surface of last scattering – where the CMB photons were created. The first detailed measurements were provided by the Cosmic Background Explorer (COBE) mission in 1991 (Mather et al. 1990), which showed a large scale isotropy of the Universe (Smoot et al. 1992). These observations were extended by the Wilkinson Microwave Anisotropy Probe

(WMAP) launched in 2001, which helped determining fundamental properties of the Universe (see e.g. Bennett et al. 2013; Hinshaw et al. 2013). The Planck mission (Planck Collaboration et al. 2011), which started with the launch of the Planck satellite in 2009, was the latest program to contribute. Figure 2.1 shows a full-sky image of the CMB published with the first data release of the Planck mission in 2013. It shows an almost perfect Planck spectrum at a temperature $T = (2.72548 \pm 0.00057) \text{ K}$ (Fixsen 2009). At first sight, though, the image seems to depict an inhomogeneous distribution. However, the fluctuations indicated by different color shades are of order $\delta T/T \sim \delta \sim 10^{-5}$ (Smoot et al. 1991, 1992). Hence, at the time of cosmic recombination the Universe was approximately homogeneous.

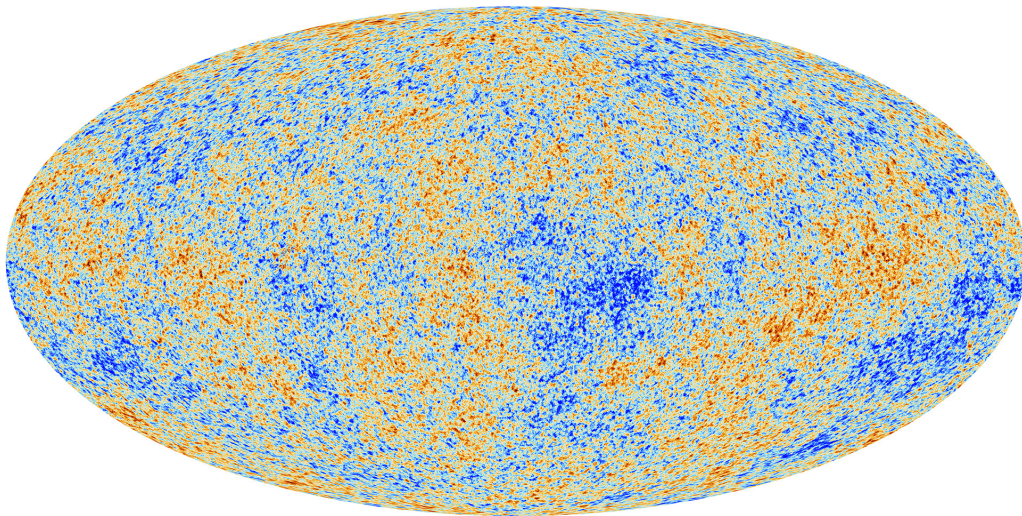


Figure 2.1. All-sky image of the CMB radiation as obtained by the Planck satellite. The radiation is ~ 13.83 Gyrs old (Planck Collaboration et al. 2018) and has an average temperature of $\sim 2.725 \text{ K}$ (Fixsen 2009). The color differences indicate temperature fluctuations of order 10^{-5} representing tiny density variations in the primordial cosmic matter distribution (Smoot et al. 1991, 1992). Source: European Space Agency. Available from: https://www.esa.int/ESA_Multimedia/Images/2013/03/Planck_CMB (date of last access: November 20, 2020 04:54 pm).

2.1.2 The inhomogeneous universe

On scales smaller than $\sim 100 \text{ Mpc}$, the observed density distribution of galaxies, groups of galaxies, and clusters reveals that the local Universe is in fact inhomogeneous. An image composed of a sample of about 10^6 galaxies at $z \lesssim 0.14$ taken throughout the runtime of the Sloan Digital Sky Survey (SDSS) is shown in Fig. 2.2. It shows that galaxies group together, leaving areas where there are virtually none. At first glance, this may seem to be in conflict with the density distribution inferred from the CMB.

Fluctuations as observed in Fig. 2.1 represent tiny primordial gravitational potential deviations as first predicted by Sachs & Wolfe (1967). These macroscopic fluctuations were a result of cosmic inflation – a phase in the Universe expected to have appeared very shortly after the Big Bang. Figure 2.1, though, shows temperature fluctuations very close to homogeneity. The Hubble radius $r_H(z) = c/H(z)$, where c is the speed of light and $H(z)$ the Hubble expansion rate, represents the horizon within which different parts of the

Universe can be in casual contact, i.e. interact with each other. In order to reach a state of thermal equilibrium as observed in the CMB, the cosmic matter had to be in casual contact before the surface of last scattering. In a radiation or matter dominated universe, though, this is impossible since r_H grows faster than space expands. The principle of inflation yields a solution to this so-called horizon problem: it describes a period in which r_H stayed constant, while space rapidly expanded. Thereby, during the onset of inflation, everything could interact to reach a state of approximate thermal equilibrium while being inside r_H . With inflation progressing, structures expand to distances far beyond the horizon. As a consequence, quantum fluctuations resulting from the inflation field grew to macroscopic density deviations and stopped growing as they lacked casual contact. After inflation, r_H continues to grow and structures entering the horizon of an observer show the same properties.

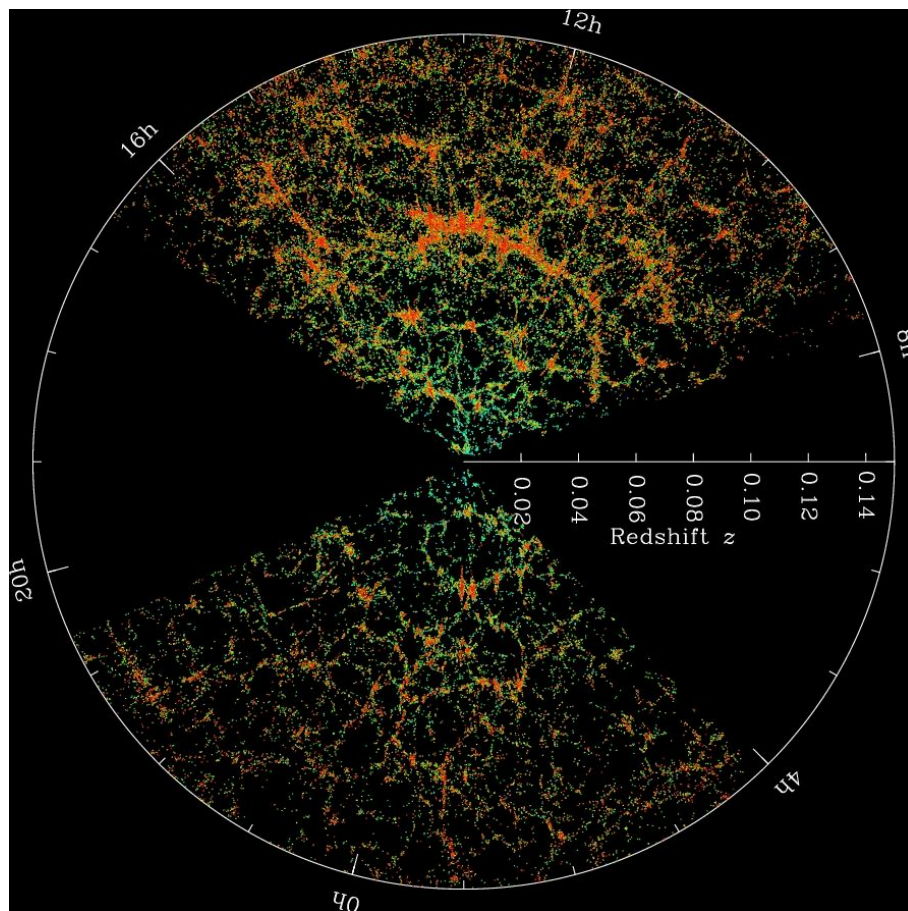


Figure 2.2. Image of large-scale structures in the local Universe at $z \lesssim 0.14$ obtained throughout the operation of the SDSS mission. The data cover $\sim 25\%$ of the northern hemisphere and contain a sample of $\sim 10^6$ galaxies. While the majority of the matter is concentrated in the cosmic web structures, most of the volume is occupied by cosmic voids. Source: SDSS. Available from: <https://dev.sdss.org/wp-content/uploads/2014/06/orangepie.jpg> (date of last access: November 18, 2020 02:23 pm).

After inflation, while r_H continuously increases, the scale at which objects can be in casual contact grows. Therefore, density perturbations lead to growing instabilities amplified by (self-)gravitation. Hence, during the evolution of the Universe, areas with a

slightly higher density resulted in an accumulation of mass forming filaments of galaxies, galaxy groups, and clusters, whereas less dense regions continuously grew to form large volumes almost devoid of gas. The entirety of these structures form the cosmic web – as can be seen in Fig. 2.2. In general, density perturbation modes can be described as plane waves with wave length λ . Modes enter the Hubble horizon when $\lambda = r_H$. Hence, smaller modes enter the Hubble horizon earlier and start to grow since they are in casual contact. The larger a mode, the later it enters the horizon. Thus, Λ CDM cosmology predicts that structures grow bottom up: small scale structures develop first, large scales later. This is known as hierarchical structure formation.

According to modern cosmological models and latest measurements, cold dark matter (see e.g. Blumenthal et al. 1984) accounts for $\sim 85\%$ of the matter in the Universe (Planck Collaboration et al. 2018). Unlike ordinary baryonic matter, dark matter only interacts through gravitation. Hence, in an early phase, where the Universe was still radiation dominated, perturbations in the dark matter distribution entering the Hubble horizon could grow faster than baryonic matter structures. When matter started to dominate in the Universe, i.e. after radiation-matter equality at $z \approx 3400$ (Planck Collaboration et al. 2018), baryonic matter began to collapse and reside in dark matter potential wells that had previously formed, which led to the emergence of the first stars, galaxies, and clusters. The dark matter accumulations meanwhile grew linearly until reaching a critical density at which point they collapsed into virialized dark matter halos. Thereafter, these halos grew non-linearly through mass accretion and merging with other halos, which resulted in subhalo structures (see e.g. Vegetti et al. 2010, 2012; Nierenberg et al. 2014).

2.2 Cosmic voids

While the matter surrounding galaxies was continuously and increasingly attracted by galaxies, clusters, and their hosting dark matter halos, the density of the intergalactic and intracluster medium dropped. In an expanding universe the density scales as $\rho \propto a^{-3} = (1+z)^3$ and, thus, the IGM density gets further reduced due to cosmic expansion progressing with time. As a result of this, primordial underdense regions were almost entirely evacuated from matter (Colberg et al. 2005) to form large *voids*. Cosmological voids are almost entirely devoid of galaxies and clusters (Einasto et al. 1980; Kirshner et al. 1981). Observations of the Local Universe have shown that most of the mass is tied to virialized objects, whereas most of the volume is made up by voids (see Fig 2.2). Hence, voids are an integral component of the galaxy and matter distribution on Mpc scales, i.e. the cosmic web. It has to be noted, though, that some voids are hosts to galaxies – the so-called void galaxies – which are also an aim of various studies (see e.g. Goldberg et al. 2005; Kreckel et al. 2011, 2012; Beygu et al. 2013, 2016, 2017).

2.2.1 Void properties

Cosmic voids have typical sizes of $10 - 50 h^{-1}$ Mpc (Hoyle & Vogeley 2002; Plionis & Basilakos 2002) and are, hence, structures at the largest scales. Voids are typically non-spherical and prolate, although they tend to become more spherical with time (Platen et al. 2008). However, they are not able to reach a state of perfect sphericity since they encounter their encapsulating overdense structures – and also due to external tidal forces. In

contrast to collapsing overdense regions, voids typically grow in size. Similarly, though, voids evolve according to hierarchical structure formation: bigger voids formed by merging and absorbing of subvoids (Gottlöber et al. 2003). During the evolution of voids, matter in the void center moves outwards faster than matter at the void edges (Hamaus et al. 2014). The so-called shellcrossing marks the transition from quasi-linear to a non-linear stage occurring when the inner mass shells pass across outer shells. Consequently, the interior develops an almost uniform density field asymptotically approaching $\delta = -1$ while matter concentrates in layers around the void. Thus, when subvoids connect, their shells form dense walls and filaments along which the matter continues to evacuate towards the ambient boundaries of the growing void. Substructures therefore align along specific directions with time, which is also very present in images e.g. of the Millennium Simulations (Springel et al. 2005; Boylan-Kolchin et al. 2009). This illustrates how inhomogeneous distributions in the density field influence a void's shape and evolution and that of its surroundings – the cosmic filaments and clusters. Understanding the structure and evolution of cosmic voids is therefore very important to properly understand the formation and dynamics of the cosmic web.

That cosmic voids allow constraints on cosmological parameters and models, the evolution of cosmic structure formation, or, for example, modified gravity has already been shown in a number of studies (see e.g. Colberg et al. 2005; Biswas et al. 2010; Bos et al. 2012; Park et al. 2012; Clampitt et al. 2013). How cosmic voids influence dynamics of galaxies and clusters in our local universe was, for example, pointed out by Tully et al. (2008), who analyzed the peculiar velocity of the Local Group, which they measured to be $\sim 631 \text{ km s}^{-1}$ with respect to the CMB. They claim that the Local Void (Tully & Fisher 1987) is responsible for $\sim 259 \text{ km s}^{-1}$ of the Local Group motion.

2.2.2 Density and velocity profiles of voids

As mentioned above, voids formed from tiny discrepancies in the primordial density field. Figure 2.3 illustrates the development of two different void density profiles with time. The left column shows a so-called tophat profile, i.e. the underdensity shows a sharp trough at the edge of the void. With time, the void expands while its interior approaches $\delta = -1$ due to matter getting attracted away from the void center. Hence, the density within the void decreases continuously as it expands. Meanwhile, the density at the edge increases drastically: the void forms a very sharp envelope (or wall) of matter. This process becomes strictly non-linear (shellcrossing). The right column of Fig. 2.3 depicts a radial-averaged, spherically symmetric density profile for a trough in a Gaussian random field of cold dark matter density fluctuations, more representative of cosmological circumstances in a Λ CDM universe. Initially, the density profile is smoother and gradually increases towards the void edge. Similarly to the tophat profile, the internal density decreases with time while the matter gets pulled outwards to form an extended envelope whose density increases. However, the envelope is less sharp and shows a smooth profile which only forms a wall of high-density matter if the density gradient is sufficiently steep. Ultimately, most void configurations evolve to a sharp tophat density profile (Sheth & van de Weygaert 2004).

The density and velocity profiles of voids in cosmological Λ CDM N -body simulations are shown in Fig. 2.4. The left column shows the stacked real-space density profile

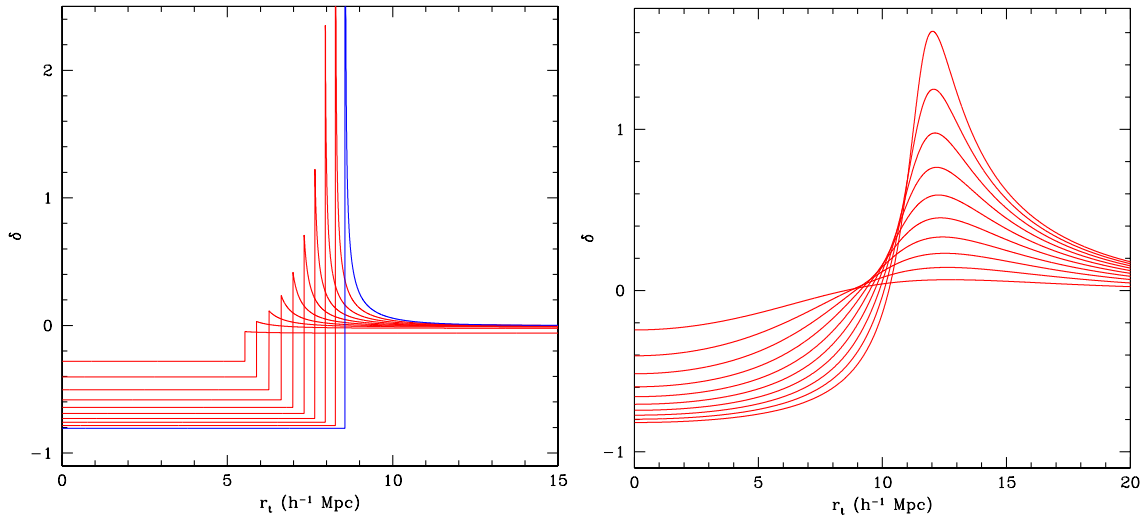


Figure 2.3. Density profile evolution of a spherical, isolated void with a tophat (left panel) and spherically symmetric cold dark matter (right panel) profile with initial comoving radii $R = 5 h^{-1}$ Mpc. Both configurations develop a wall of matter at the void edge with time. Adopted from [van de Weygaert & Platen \(2011\)](#).

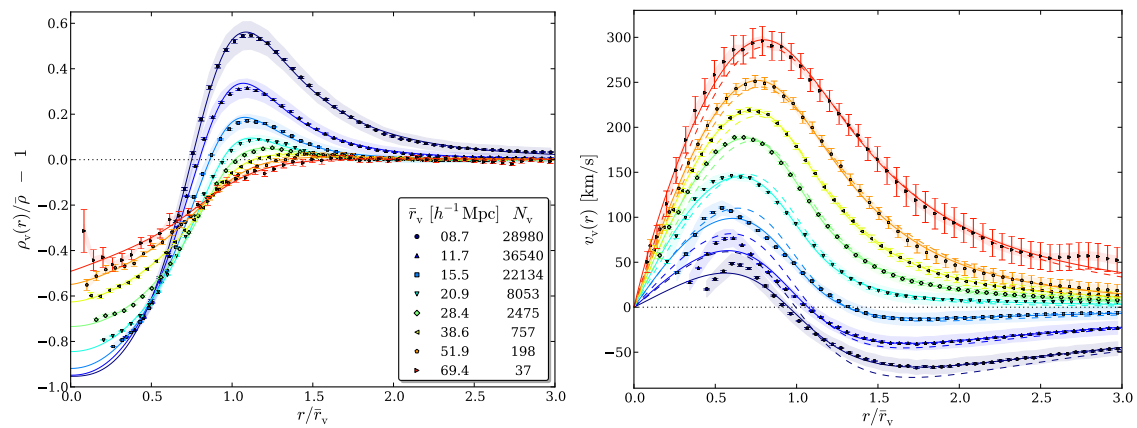


Figure 2.4. Stacked real-space density (left panel) and velocity (right panel) profiles of voids at $z = 0$ from Λ CDM N -body simulations. Mean effective radii and void counts are indicated in the left column inset. Shaded regions indicate the standard deviation σ within the stacks, and error bars show standard errors on the mean profile $\sigma/\sqrt{N_v}$. Solid and dashed lines represent best-fit solutions and linear theory predictions for velocity obtained from the density stacks, respectively. Voids that are sufficiently underdense in their center develop a wall of matter at their edge. While the gas moves outwards of large voids, smaller voids face to collapse due to infalling gas. Adopted from [Hamaus et al. \(2014\)](#).

of a large sample of voids of different sizes. Small voids show a very steep density profile with an extended accumulation of mass, while large voids show a much smoother profile. Thus, with decreasing void size, the density profile gets steeper and the density peak at the void edge intensifies. The void size here simply defines the evolution steps of a void: the density profiles correspond to the evolution of the spherically symmetric cold dark matter profile depicted in the left column of Fig. 2.3. At large distances, voids of all sizes approach the mean cosmic density. Generally, they still reflect how voids build mass-enriched envelopes while they evolve and expand. The right column of Fig. 2.4 shows the velocity profile of the respective voids. Here, positive velocities reflect outflowing gas while negative velocities represent inflowing gas. At large distances, the gas velocities approach zero. Large voids, though, show an outflow of gas throughout the entire range which peaks closely before the effective radius. The increasing velocity towards the effective radius in all void sizes represents the increasing influence of the void wall. Small voids, on the other hand, show much lower velocities with a sign change shortly after their effective radius, indicating an inevitable collapse.

2.2.3 Void evolution

As mentioned previously, voids usually expand and result from matter collapsing into filaments and clusters, thereby forming a supercluster-void network (Frisch et al. 1995; Einasto et al. 2012). While large voids expand, small voids surrounded by overdense regions disappear due to the surrounding matter collapsing (Ceccarelli et al. 2013; Paz et al. 2013). The major scenarios of void evolution are illustrated in Fig. 2.5. Here, the evolution with time is represented by the left and right column. The top row shows the so-called cloud-in-void setting in which an initially overdense region within a large void forms filaments within the void through its gravitational collapse and the intrinsically connected expansion of the surrounding voids. This scenario reflects the origin of void galaxies. The void-in-void setting is depicted in the middle row. Here, a large void forms through mergers of smaller subvoids, which demonstrates how bigger voids result from hierarchical structure formation. The bottom row describes the void-in-cloud scenario. It shows how voids surrounded by overdensities shrink due to ambient matter collapsing, potentially removing the void. This effect is responsible for the lack of small voids, i.e. a cutoff of the void size distribution at small scales (Sheth & van de Weygaert 2004).

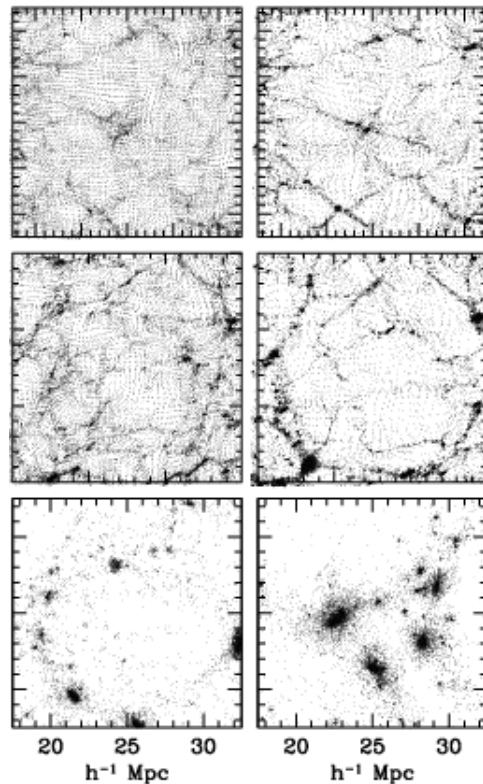


Figure 2.5. Time evolution of the particle distribution for three different hierarchical clustering scenarios of cosmic voids. The three rows show the cloud-in-void (top), void-in-void (middle), and void-in-cloud (bottom) processes. Adopted from [Sheth & van de Weygaert \(2004\)](#).

2.3 The intergalactic medium and its reionization

The IGM is the region between galaxies containing low-density gas. In the present state of the Universe, $\sim 30 - 40\%$ of the cosmic baryons reside in the so-called warm-hot IGM with temperatures ranging $T \sim (10^5 - 10^7)$ K ([Davé et al. 2001](#)). In the early ages of the Universe, though, no galaxies had formed yet. The first stars and galaxies had likely formed just recently before the EoR ([Bromm & Larson 2004](#); [Naoz et al. 2006](#); [Bromm & Yoshida 2011](#)). Thus, the term pre-galactic medium is more appropriate at earlier times.

2.3.1 Reionization of the cosmic gas

Subsequent to the Big Bang, at $z \simeq 1100$, after photon decoupling created the CMB, the fraction of neutral gas in the pre-galactic medium decreased abruptly ([Peebles 1968](#); [Seager et al. 2000](#)) and, thereafter, remained so for a very long period. Figure 2.6 shows a schematic development of the EoR with time after the decoupling of photons until its present state. During the dark ages of the cosmos ([Rees 1997](#)), the hot and dense pre-galactic medium predominantly filled with H I and neutral helium (He I) then cooled as the Universe expanded and structure formation progressed. The first stages of reionization of the pre-galactic medium most likely took place as a result of stellar feedback processes from the first stars ([Bolton et al. 2005](#); [Faucher-Giguère et al. 2008](#); [Becker & Bolton 2013](#)), which initiated the ending of the dark ages. As a result of this process, the low-

density gas near overdensities populated with ionizing sources reionized earlier than gas in large-scale voids (Trac et al. 2008). With the amount of neutral gas around the ionizing sources dropping, the radiation could reach out further and further into space, forming expanding bubbles of reionized gas that grew until they eventually overlapped to fill the whole space.

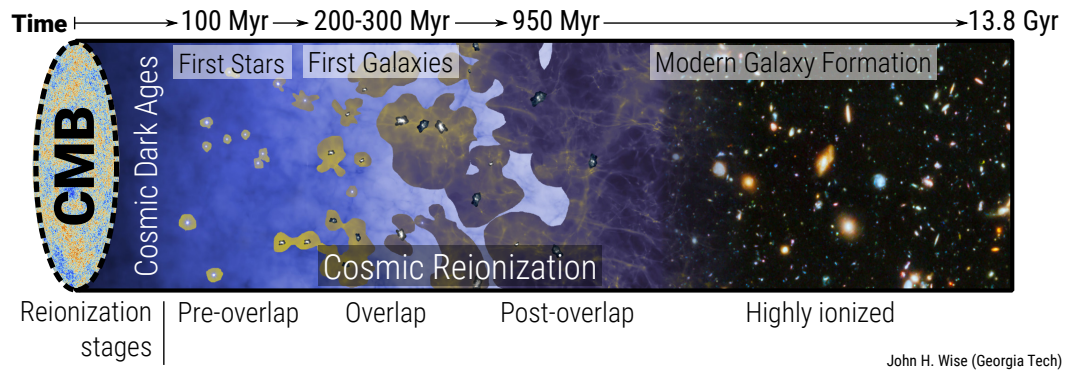


Figure 2.6. Evolutionary timeline of the EoR after photon decoupling. Ionizing sources distributed in space start to reionize their surrounding gas. As a consequence, they form bubbles of reionized gas which expand to eventually fill the whole Universe. Adapted from Wise (2019).

The EoR, i.e. the reionization of H I and He I, lasted from about $z \approx (6 - 10)$. The end of He II reionization likely occurred at $z \approx 3$ (Becker et al. 2011; Worseck et al. 2011, 2016). The onset of cosmic reionization, however, is still very unclear in terms of redshift, although it is very likely to have finished at $z \approx 6$ according to measurements of QSO spectra at $z > 6$ (Fan et al. 2006). As inferred from radiative transfer simulations, it may even have lasted until $z \lesssim 5.5$ (Kulkarni et al. 2019a). Planck Collaboration et al. (2016) estimated the average redshift at which reionization occurs to be in the range of $z \approx (7.8 - 8.8)$, while Planck Collaboration et al. (2018) measure the reionization midpoint to appear at $z \approx (7.7 \pm 0.7)$.

2.3.2 Observables of the high-redshift universe

The investigation of early phases in the EoR is very difficult because there are very few currently known observables. One such possibility is measuring anisotropy in the CMB (see e.g. Bennett et al. 2013; Planck Collaboration et al. 2014, 2016, 2018). Besides providing constraints on cosmic reionization, this is also an excellent tool to measure a variety of cosmological quantities. An option for the late stage of cosmic reionization is the Ly α forest of high- z QSO spectra. However, there are limits to this method: a drastic increase of the IGM optical depth prevents transmission of background emission at $z > 6$ such that Ly α forest features are no longer observable except for the near zone of QSOs. A very promising alternative to study also early phases of the EoR is the 21-cm radiation from the hyperfine transition of H I (Madau et al. 1997; Pritchard & Loeb 2012). In fact, it might give the opportunity to probe the high- z IGM beyond the EoR (Ciardi & Madau 2003) and possibly even the pre-galactic medium up to $z \approx 200$ (Furlanetto et al. 2006). However, even with state-of-the-art instruments the 21-cm signal shows substantial contamination by (extra-)galactic sources preventing measurements of signals from primordial gas (Di Matteo et al. 2002; Oh & Mack 2003). This might change with

next-generation radio telescopes such as the Square Kilometre Array (SKA) (Weltman et al. 2020).

2.3.3 Sources of ionizing radiation

The first stars in the early star-forming galaxies were so-called Population III stars. These are extremely metal-poor while consisting almost entirely of H I and He I (Bromm & Larson 2004). The low-mass parts of their follow-up generation – the metal-poor Population II stars – are still observed in the Milky Way halo and satellite dwarf galaxies, and provides the opportunity to study the chemical nature of the earliest stars and galaxies in our cosmos (see Frebel & Norris 2015). The gas in the IGM was continuously heated by soft X-ray photons emitted by Population III stars (Madau et al. 1997); an effect that might potentially be observable utilizing the 21-cm hyperfine line of H I (Furlanetto et al. 2006). Besides photoheating, Population III stars also produced UV photons with energies $E_\gamma > 13.6 \text{ eV}$, which started to reionize the gas in their surrounding medium. However, to heat and reionize gas far out in the IGM, a significant fraction of the stellar UV photons must have been able to escape from galaxies. Simulations yield photon escape fractions of $f_{\text{esc}} = (0.01 - 0.8)$ (Gnedin et al. 2008; Wise & Cen 2009; Kimm & Cen 2014; Ma et al. 2015), while observations at $z \gtrsim 3$ yield escape fractions for bright galaxies of just a few per cent, e.g. $f_{\text{esc}} \gtrsim 0.04$ (Iwata et al. 2009; Siana et al. 2010) and $f_{\text{esc}} \approx (0.1 - 0.4)$ for faint Ly α emitters (Cooke et al. 2014; Nestor et al. 2013). It is therefore unclear how many photons actually could escape the primordial galaxies into the IGM in order to reionize it.

A decent measure of the contribution by galaxies is their luminosity in the UV band, which is an estimate of the number of ionizing photons available for reionization. The luminosity function for galaxies, which represents the density of galaxies with a certain luminosity L per unit volume (e.g. per Mpc^3), is described by the Press-Schechter fit (Schechter 1976) as

$$\phi(L) dL = \phi_* \left(\frac{L}{L_*} \right)^\alpha \exp\left(-\frac{L}{L_*}\right) \frac{dL}{L_*}, \quad (2.3.1)$$

where ϕ_* denotes the normalization number density per unit volume, L_* a characteristic luminosity (with a characteristic absolute magnitude M_*) at which the luminosity function shows a rapid change in the slope, and α the slope of the function at $L \ll L_*$. As of today, the UV luminosity function is very well known at $z \approx (4 - 8)$ and has been measured multiple times from different galaxy samples (Bowler et al. 2014, 2015; Bouwens et al. 2015; Finkelstein et al. 2015). Figure 2.7 shows the rest-frame UV luminosity functions derived by Bouwens et al. (2015) from a sample of $\gtrsim 10,000$ galaxies at $z \approx (6 - 10)$ assembled by the Hubble Space Telescope. It shows that there is, in fact, a decline in UV luminosity of galaxies with increasing redshift. However, Finkelstein et al. (2015) claim that their sample match a reionization history beginning at $z \gtrsim 10$ and fading at $z \gtrsim 6$, having its midpoint ($x_{\text{HI}} = 0.5$) somewhere between $z = (6.4 - 9.7)$.

As well as stars, QSOs were first proposed as contributors to the ionizing radiation field by Arons & McCray (1970). At high redshifts $z > 4$, though, the observed quantity of QSOs suggests that their abundance is not sufficient to drive the reionization of the IGM (Shapiro et al. 1994; Willott et al. 2010; Masters et al. 2012). This argument is also supported by their observed UV luminosity function at $z < 7.5$ (Kulkarni et al. 2019b),

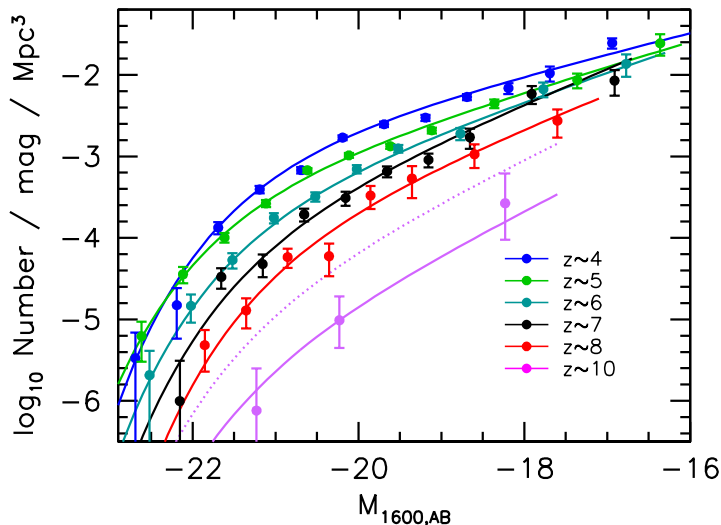


Figure 2.7. Galaxy rest-frame UV luminosity functions at $z \sim 4$ (blue), $z \sim 5$ (green), $z \sim 6$ (cyan), $z \sim 7$ (black), $z \sim 8$ (red), and $z \sim 10$ (magenta) derived from a sample of $\geq 10,000$ galaxies at $z \approx (4 - 10)$. The data points with error bars and the solid lines represent the measurements and best-fit Schechter functions (Eq. 2.3.1), respectively. The dotted, magenta line depicts the expected luminosity function at $z \sim 10$ when extrapolating it from the luminosity function at $z \approx (4 - 8)$. The observations reveal a decline in UV luminosity of galaxies with redshift. Adopted from Bouwens et al. (2015).

which suggests a marginal contribution to H I ionization. On the contrary they substantially drove He II reionization, accounting for half of the ionizing radiation at $z < 0.5$. This was argued against, though, by Giallongo et al. (2015), who observed a population of 22 QSOs at $z \approx (4.5 - 6)$ in the Chandra Deep Field South and claimed that this could produce an emissivity of photoionizing radiation sufficient to provide a major contribution to the cosmic reionization process. Their observations caused further investigations of a possible quasar-driven reionization model (see e.g. Chardin et al. 2015; Madau & Haardt 2015), which found that a contribution of QSOs would have completed He II reionization at $z \approx 4$. Measurements of the He II Ly α forest, however, indicate that this reionization took until $z \lesssim 2.7$ (Shull et al. 2010), suggesting that the model is incompatible with observations. Further ionizing sources which may have helped to reionize the IGM have also been suggested, such as high-mass X-ray binaries (Mirabel et al. 2011), X-rays originating from supernovae (Johnson & Khochfar 2011), or inverse Compton scattering of cosmic rays (i.e. relativistic electrons) created by supernovae in the earliest star clusters (Oh 2001).

2.3.4 Radiation background modeling in cosmological simulations

The early galaxies were likely populated by sources that filled the Universe with ionizing radiation, which eventually reionized the entire IGM. These sources provided a background of ionizing photons of different energies – the cosmic UVB. In order to retain the gas in the IGM in an ionized region in its ionization state, the ionization by the photon flux of the UVB ($H + \gamma \rightarrow p^+ + e^-$) and collisional ionization ($H + e^- \rightarrow p^+ + 2e^-$) have to

balance the number of recombinations ($p^+ + e^- \rightarrow H$). Only taking into account hydrogen, ionized regions fulfill the equation of ionization equilibrium

$$\Gamma_{\text{HI}} n_{\text{HI}} + n_{\text{HI}} n_e \Gamma_e(T) = \alpha(T) n_{\text{HII}} n_e, \quad (2.3.2)$$

where n_{HI} , n_{HII} , and n_e are the number densities of H I, H II, and electrons, respectively, α the recombination coefficient, Γ_{HI} the H I photoionization rate provided by the cosmic UVB, and Γ_e the collisional ionization rate. At very low densities as they exist in the IGM, the photoionization rate should dominate compared to the collisional ionization, i.e. $\Gamma_{\text{HI}} \gg \Gamma_e$, hence

$$\Gamma_{\text{HI}} n_{\text{HI}} \approx \alpha(T) n_{\text{HII}} n_e. \quad (2.3.3)$$

Thus, the ionization equilibrium represents a state in which the ionization of H I and recombination of H II and electrons (i.e. $H + \gamma \leftrightarrow p^+ + e^-$) are in equilibrium. Γ_{HI} can be understood as the number of ionizing photons available for reionization per unit time and is defined as

$$\Gamma_{\text{HI}}(z) = \int_{\nu_0}^{\infty} \frac{4\pi J(\nu, z)}{h\nu} \sigma_{\text{HI}}(\nu) d\nu, \quad (2.3.4)$$

where J is the UV flux irradiance in units $W m^{-2} s^{-1} sr^{-1}$ per unit frequency interval, and σ_{HI} the photoionization cross section. The first fraction converts energy flux to photon flux, i.e. the number of photons per unit area per unit time per unit frequency. The lower integral boundary ν_0 here represents the frequency of a photon with the minimum required energy to ionize hydrogen, i.e. the bounding energy of hydrogen $E_0 = 13.6 \text{ eV}$.

If a photon has an energy $E > E_0$, the energy difference to the excitation threshold of hydrogen is converted into the kinetic energy of the freed electron, which characterizes its thermal energy through its thermal velocity. Hence, the electrons get heated by the amount of energy excess $E - E_0 = h\nu - h\nu_0$. Thus, similarly to the photoionization rate, this energy excess defines the H I photoheating rate as

$$\epsilon_{\text{HI}}(z) = \int_{\nu_0}^{\infty} \frac{4\pi J(\nu, z)}{h\nu} \sigma_{\text{HI}}(\nu) (h\nu - h\nu_0) d\nu. \quad (2.3.5)$$

Both Γ_{HI} and ϵ_{HI} change with time, hence are redshift dependent because J is intrinsically connected to the star-formation history, which changes with the evolution of galaxies. Observations confirm a relatively flat evolution of Γ_{HI} at $z \approx (2 - 5)$ (Becker & Bolton 2013; Bolton et al. 2017). Assuming a spatially homogeneous UVB, models yield results convincingly consistent with observations at redshifts after H I reionization completes. The cosmic UVB after the end of reionization is nearly spatially homogeneous, whereas during reionization at $z \gtrsim 5$ the radiation field is rather patchy due to ionized bubbles populated with ionizing sources and entirely neutral regions (Fan et al. 2006; Becker et al. 2015; Eilers et al. 2018). Recent projects, such as the SHERWOOD RELICS simulations investigated in this work, model the process of reionization and, thereby, the high- z Ly α forest using a combination of cosmological simulations with radiative transfer simulations to mimic a realistic evolution of the H I fraction of the IGM.

2.3.5 Thermal evolution

At the time of photon decoupling, when the CMB was created, the CMB and gas temperature were approximately equal, i.e. $T_{\text{gas}} \approx T_{\text{CMB}}$. The expansion of the Universe

then cooled the gas and the photons after recombination, where the temperatures were coupled to one another. At $z \approx 200$, the gas and CMB temperature decoupled and the cooling process became adiabatic (Zaroubi 2013), hence the cosmic gas and CMB photon cooling can be described by an adiabatic equation: since $p \propto \rho^\gamma$ for an adiabatic gas, the temperature scales with $T \propto \rho^{\gamma-1}$. Considering that the density drops with redshift due to cosmological expansion as $\rho \propto (1+z)^3$ yields

$$T \propto (1+z)^{3(\gamma-1)}, \quad (2.3.6)$$

where γ is the adiabatic index of the relation. Thus, it follows that $T \propto (1+z)$ for the CMB ($\gamma = 4/3$ for photons), and $T \propto (1+z)^2$ for the H I- and He I-dominated IGM ($\gamma = 5/3$ for a mono-atomic gas). Hence, after recombination the cosmic gas cools faster than the CMB photons.

Hui & Gnedin (1997) have shown that the temperature-density ($T - \Delta_b$) relation at low densities (i.e. the IGM) after the EoR can typically be described by a simple power law dependent on the cosmic baryon density

$$T(\Delta_b) = T_0 \Delta_b^{\gamma-1}, \quad (2.3.7)$$

where T_0 is the temperature at mean density. The index of the above relation, however, is still debated. Towards the end of reionization, the $T - \Delta_b$ relation may well be an inverted power law with slope $(\gamma - 1) \lesssim -0.2$ (Furlanetto & Oh 2009; Trac et al. 2008). After reionization, though, the slope might correspond to $(\gamma - 1) \sim 0.5$ (Trac et al. 2008), which is close to the value calculated by Hui & Gnedin (1997). At lower redshifts $z \simeq (2 - 2.8)$, at least the slope and T_0 are constrained by measurements of H I absorption profiles in the Ly α forest as $(\gamma - 1) \sim 0.5$ and $T_0 \sim 10^4$ K, respectively (Rudie et al. 2012; Bolton et al. 2014). Other studies find consistent results for T_0 : it increases from $\sim (6 - 8) \times 10^3$ K at $z \sim 5.4$ to reach $\sim 14 \times 10^3$ K at $z \sim 3.4$ and drops to $\sim 7 \times 10^3$ K again at $z \sim 1.8$ (Boera et al. 2019; Walther et al. 2019). The observed evolution of T_0 suggests that the heating of the IGM predominantly happened after H I reionization, most likely due to He II reionization (Hiss et al. 2018). However, according to Walther et al. (2019) the slope of $T - \Delta_b$ might even be $(\gamma - 1) \sim 0.6$ at $z \sim 2.8$.

2.4 Quasar absorption systems

On its way to an observer, the light of a QSO passes through various different systems such as gas clouds, galaxies, or galaxy halos, which are distributed in the cosmic web structures. Any system appearing in a QSO spectrum has different properties that affect the transmitted light. These properties are defined by the physical characteristics that result from the systems' composition. Absorption and emission features are influenced by quantities such as the abundance of elements, their column density and respective degree of ionization, temperature, turbulence of the gas as well as, of course, the cosmological redshift at which the respective system exists. Hence, the spectra of QSOs are a powerful tool to investigate these intervening systems.

2.4.1 The Lyman- α forest

The Ly α line is one of the lines appearing in the Lyman series, which results from electrons transitioning from higher orbits n to the ground state $n = 1$ in the hydrogen atom or, more generally, in single-ionized atoms. If a transition occurs, the electron loses energy by photon emission. The Ly α line in particular appears when an electron transits from $2 \rightarrow 1$. According to the Bohr model and neglecting fine structure splitting, the energy of an emitted photon is given by the energy difference of the two states

$$\Delta E_{2 \rightarrow 1} = E_2 - E_1 = E_R \left(\frac{1}{1^2} - \frac{1}{2^2} \right) = 10.2 \text{ eV}, \quad (2.4.1)$$

where $E_R = 13.6 \text{ eV}$ is the Rydberg energy. Since the energy of a photon is given by $E_\gamma = hc/\lambda$, the wavelength of the emitted Ly α photon is $\lambda_{\text{Ly}\alpha} = 1215.67 \text{ \AA}$. Vice versa, electrons can also be elevated from $1 \rightarrow 2$ through photon absorption if $E_\gamma = 10.2 \text{ eV}$. This has a noticeable effect on spectra of distant QSOs.

Figure 2.8 depicts a schematic setup of the observation of a high- z QSO: while propagating through the cosmos, light emitted by a QSO passes through numerous thin gas clouds consisting of H I, each of which absorbs a fraction of the light at the rest-frame wavelength of the Ly α line $\lambda_{\text{Ly}\alpha}$ due to high H I column densities. Since the absorbing clouds appear at intermediate redshifts $z < z_{\text{QSO}}$, their respective Ly α absorption line gets redshifted to higher wavelengths $\lambda = \lambda_{\text{Ly}\alpha}(1+z)$ as seen by the observer, hence appearing bluewards of the Ly α emission line of the QSO.

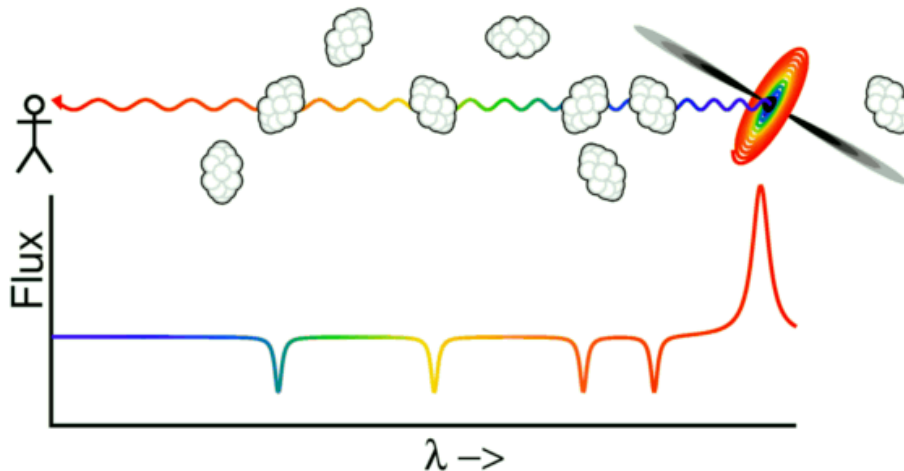


Figure 2.8. Schematic explanation of the Ly α forest: fractions of the light emitted by a QSO are absorbed by interloping gas clouds containing H I. Source: Division of Astronomy and Astrophysics, University of California, Los Angeles. Available from: <http://www.astro.ucla.edu/~wright/lyaf-75.gif> (date of last access: November 11, 2020 11:18 am).

In a realistic scenario, there are countless gas clouds between high- z QSOs and Earth. Therefore, the spectra show numerous absorption features each at a different redshift appearing as a forest of absorption lines, known as the *Ly α forest* (for a detailed review see e.g. Rauch 1998). Figure 2.9 shows three real QSO spectra at $z = (1.3, 2.9, 5.8)$ in the top, middle, and bottom panel, respectively. The Ly α , Lyman- β (Ly β), and metal emission lines of the gas surrounding the QSO are indicated in the top and middle panel.

The top panel reveals that at low redshifts most of the gas along the LOS is ionized with very low HI fractions $x_{\text{HI}} \equiv n_{\text{HI}}/n_{\text{H}} \ll 1$. Here, only a few, mostly weak absorption lines appear in the spectrum due to the low density of the IGM. At $z = 2.9$ the IGM density already increases such that they form the characteristic forest of Ly α (Ly β) absorption lines bluewards of the QSO's Ly α (Ly β) emission. At even higher redshifts close to the end of the EoR and earlier, the HI fraction and, consequently the Ly α optical depth, increases drastically. Since even tiny amounts of HI in the IGM cause absorption, the spectra of QSOs at $z \gtrsim z_{\text{r}}$ show very extended Ly α absorption lines. Close to the QSO, in the so-called proximity zone, the gas is exposed to a strong radiation field and, thus, remains ionized resulting in transmission. Away from the proximity zone there is no transmission to be observed anymore closely bluewards of the Ly α emission line – the so-called Gunn-Peterson trough (Gunn & Peterson 1965), which is a very prominent feature in the spectra of QSOs at $z > 6$ (see e.g. Fan et al. 2006). All along the LOS there are areas where basically no background emission is visible. Hence, Ly α spectra of high- z QSOs only show certain sections with spike-shaped transmission, the *Ly α transmission spikes*, which result from highly ionized, underdense regions of gas (Barnett et al. 2017; Chardin et al. 2018; Keating et al. 2020).

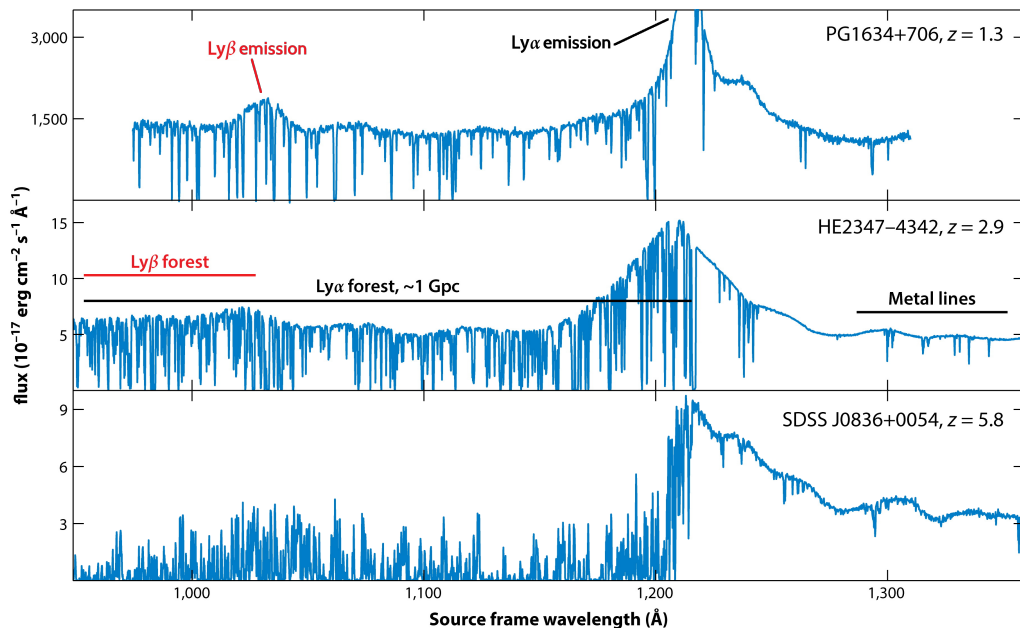


Figure 2.9. Three spectra of QSOs at $z = (1.3, 2.9, 5.8)$. The position of the Ly α and Lyman- β (Ly β) emission line is indicated in the upper panel. In the middle panel, the position of the Ly α and Ly β forest and metal absorption lines are highlighted. The intensification and growing number of the absorption lines indicate an increase of the HI fraction and the density of the IGM with redshift, respectively. Adopted from McQuinn (2016) and modified.

The main focus of studies dedicated to the Ly α forest are absorption lines at lower redshifts since they allow investigations of the absorbing systems. However, investigating structures of the cosmic web with low densities, i.e. voids, requires the measurement of certain physical processes such as, for example, the thermal Sunyaev-Zeldovich effect (Alonso et al. 2018) or gravitational lensing by voids (Melchior et al. 2014; Sánchez et al. 2017; Vielzeuf et al. 2021). The first can mainly be observed in galaxy halos in the

enveloping walls and filaments of cosmic voids. The density in voids, however, is in fact so low that a measurement of the effect is difficult resulting in weak signals. Furthermore, (Alonso et al. 2018) only measure relative signals, which does not allow any constraints about voids. Void lenses are also not eligible to study individual voids in detail since their analysis requires stacking of a large number of signals. Thus, Ly α transmission spikes are possibly the only observable to directly measure the gas contents and properties of cosmic voids.

2.4.2 Broadening of spectral lines

Naturally, one would expect that a spectral line appears at a unique wavelength as a very narrow peak. However, there exist certain physical effects which broaden spectral lines to (ideally) show symmetric line profiles (e.g. Gaussian, Lorentzian, or Voigt). The three most common local effects, which are linked to basic physical principles, are the natural, pressure, and thermal broadening. In addition to this, there also exist non-local effects that cause line broadening such as turbulence.

Natural broadening

Natural broadening is a result of a basic principle of quantum mechanics: Heisenberg's uncertainty principle (Heisenberg 1927). It states that two conjugate pairs of a quantum mechanical object, such as position and momentum, can never be measured simultaneously with precision. There is always a minimum uncertainty defined by Planck's constant h . This also influences absorption and emission processes. The radiative excitation cross section for the Ly α transition of a cold gas cloud at rest is given by (Gunn & Peterson 1965)

$$\sigma_{\text{Ly}\alpha}(\nu) = \frac{\pi e^2}{m_e c} f_{\text{Ly}\alpha} L(\nu), \quad (2.4.2)$$

where e and m_e are the electron charge and mass, respectively, c is the speed of light, $f_{\text{Ly}\alpha}$ the Ly α oscillator strength, and $L(\nu)$ the line profile function that satisfies $\int_0^\infty L(\nu) d\nu = 1$. Here, $L(\nu)$ is (see Eq. 3.56 in Rybicki & Lightman 1986)

$$L(\nu) = \frac{\frac{\gamma}{4\pi^2}}{(\nu - \nu_0)^2 + \left(\frac{\gamma}{4\pi}\right)^2}, \quad (2.4.3)$$

where γ is the natural line width (see Eq. 3.50 in Rybicki & Lightman 1986), ν the photon frequency, and ν_0 the respective line resonance frequency, e.g. that of the Ly α transition of H I (Peebles 1993). $L(\nu)$ shapes a so-called Lorentz profile. This profile defines the optical depth of a low-temperature gas cloud at rest. In reality, though, gas clouds in the IGM are moving towards a preferred direction. Hence, Doppler shifting due to the movement of the gas cloud relative to the observer influences the position of the absorption line.

Consider a gas cloud moving with a non-relativistic bulk velocity v_{bulk} relative to an observer. Here, we only consider the velocity component along the LOS of the observer since, in the non-relativistic regime, perpendicular velocity components do not cause a

Doppler shift. The observed frequency of a photon with frequency ν in the rest frame of the gas cloud then shifts to frequency

$$\nu_{\text{obs}} = \frac{\nu}{1 + \frac{v_{\text{bulk}}}{c}} \quad (2.4.4)$$

in the rest frame of the observer. Hence, in this scenario Eq. 2.4.3 yields

$$L(\nu_{\text{obs}}) = \frac{\frac{\gamma}{4\pi^2}}{\left(\nu_{\text{obs}} \left(1 + \frac{v_{\text{bulk}}}{c}\right) - \nu_0\right)^2 + \left(\frac{\gamma}{4\pi}\right)^2} \quad (2.4.5)$$

for the observer. Taking into account that the velocity is assumed to be non-relativistic, i.e. $v_{\text{bulk}} \ll c$, and Taylor expanding while neglecting terms of higher order, the term in the denominator can be approximated as

$$\nu_{\text{obs}} \left(1 + \frac{v_{\text{bulk}}}{c}\right) \approx \nu_{\text{obs}} - \nu_0 \left(1 - \frac{v_{\text{bulk}}}{c}\right). \quad (2.4.6)$$

Plugging this into Eq. 2.4.5 yields the line profile of a moving gas cloud

$$L(\nu_{\text{obs}}) = \frac{\frac{\gamma}{4\pi^2}}{\left(\nu_{\text{obs}} - \nu_0 \left(1 - \frac{v_{\text{bulk}}}{c}\right)\right)^2 + \left(\frac{\gamma}{4\pi}\right)^2}, \quad (2.4.7)$$

which demonstrates that the line center of an absorption line shifts from ν_0 to (approximately) $\nu_0 (1 - v_{\text{bulk}}/c)$ in the rest frame of the observer.

Pressure broadening

Pressure broadening results from the diffuse movement of particles in a thermal gas. Collisions during an excited state lead to a distortion of the energy levels of the orbits since the collisions interrupt the emission and absorption processes. This also results in a Lorentzian line profile shape. The effect, however, is proportional to the particle number density and gas temperature and therefore negligible in low-density regions such as the IGM.

Thermal broadening

Consider an ensemble of gas particles, i.e. a gas cloud, along the LOS towards a celestial object. Assuming the gas behaves as an ideal gas, the one-dimensional thermal velocity distribution of that cloud along the LOS is described by the Maxwell-Boltzmann distribution

$$p(v_{\text{th}}) = \frac{1}{\sqrt{\pi}b} \exp\left(-\frac{v_{\text{th}}^2}{b^2}\right), \quad (2.4.8)$$

where

$$b = \sqrt{\frac{2k_{\text{B}}T}{m}} \quad (2.4.9)$$

is the Doppler parameter with Boltzmann's constant k_B , the gas temperature T , and the gas particle mass m . Due to the diffuse movement of the gas, the atoms do not only absorb at the line resonance frequency ν_0 , but also at the Doppler shifted frequency $\nu = \nu_0(1 + v_{\text{th}}/c)$. As a consequence, their motion broadens the line. The profile of the line here corresponds to the number of photons absorbed at the Doppler shifted frequency, which is proportional to the fraction of particles with a certain velocity, i.e. $G(\nu) d\nu = p(v_{\text{th}}) dv_{\text{th}}$ (Theuns 2007). Therefore

$$G(\nu) = p(v_{\text{th}}) \frac{dv_{\text{th}}}{d\nu} = \frac{1}{\sqrt{\pi}\Delta\nu_D} \exp\left(-\frac{(\nu - \nu_0)^2}{\Delta\nu_D^2}\right), \quad (2.4.10)$$

where $\Delta\nu_D = \nu_0 b/c$ is the broadening parameter. As can be seen, the above equation is similar to a Gaussian distribution $f(x) = 1/\sqrt{2\pi\sigma^2} \exp(-(x - \mu)^2/(2\sigma^2))$ with mean μ and standard deviation σ . Hence, Eq. 2.4.10 produces a Gaussian line shape.

Voigt profile

In reality, an intergalactic gas cloud exhibits both of the described effects since each gas particle will also produce a Lorentzian-shaped absorption line. Hence, the resulting line profile is given by the convolution of the Lorentzian and Gaussian line shapes, i.e. Eqs. 2.4.3 and 2.4.8. Thus, following Theuns (2007) and replacing v_{bulk} with $v_{\text{bulk}} + v_{\text{th}}$, the final line profile is given by

$$\begin{aligned} V(\nu_{\text{obs}}) &= \int_{-\infty}^{\infty} dv_{\text{th}} p(v_{\text{th}}) L(\nu_{\text{obs}}) \\ &= \frac{1}{\sqrt{\pi}b} \int_{-\infty}^{\infty} dv_{\text{th}} \exp\left(-\frac{v_{\text{th}}^2}{b^2}\right) \frac{\frac{\gamma}{4\pi^2}}{\left(\nu_{\text{obs}} - \nu_0 \left(1 - \frac{v_{\text{bulk}} + v_{\text{th}}}{c}\right)\right)^2 + \left(\frac{\gamma}{4\pi}\right)^2}. \end{aligned} \quad (2.4.11)$$

This is the so-called Voigt profile. Setting $y = -v_{\text{th}}/b$ and defining $a = \gamma/(4\pi\Delta\nu_D)$, the last term of the above equation can be rewritten as

$$\frac{1}{\Delta\nu_D} \frac{\frac{a}{\pi} \exp(-y^2)}{\left(\frac{\nu_{\text{obs}} - \nu_0}{\Delta\nu_D} + \frac{v_{\text{bulk}}}{b} - y\right)^2 + a^2} \quad (2.4.12)$$

which then simplifies Eq. 2.4.11 to

$$V(\nu_{\text{obs}}) = \frac{H(a, u)}{\sqrt{\pi}\Delta\nu_D}, \quad (2.4.13)$$

where

$$u = \frac{\nu_{\text{obs}} - \nu_0}{\Delta\nu_D} + \frac{v_{\text{bulk}}}{b} \quad (2.4.14)$$

and

$$H(a, u) = \frac{a}{\pi} \int_{-\infty}^{\infty} \frac{\exp(-y^2)}{a^2 + (u - y)^2} dy \quad (2.4.15)$$

is the Voigt-Hjerting function (Hjerting 1938). $H(a, u)$ cannot be solved analytically and, hence, has to be approximated numerically (see e.g. Hjerting 1938; Hummer 1965;

Tepper-García 2006). Furthermore, absorption and emission lines can also be described by their Doppler velocity v_{line} relative to an observer, i.e. $v_{\text{obs}} = v_0/(1 + v_{\text{line}}/c)$. Rewriting this similarly as in the case of Eq. 2.4.6, the parameter u can be given in terms of v_{line} as

$$u = \frac{v_{\text{bulk}} - v_{\text{line}}}{b}. \quad (2.4.16)$$

The Voigt profile is a convolution of a Gaussian and Lorentzian line profile and, thus, consists of both of these components. The natural line width, however, is much narrower than the Doppler width. Therefore, the Voigt profile is indistinguishable from a Gaussian in its center, although it is dominated by a Lorentzian in the wings, hence

$$H(a, u) \sim \begin{cases} \exp(-u^2) & \text{center: Gaussian curve} \\ a/(\sqrt{\pi}u^2) & \text{wings: Lorentzian damping wings} \end{cases} \quad (2.4.17)$$

2.4.3 Optical depth of a gas cloud in the IGM

Consider a gas cloud consisting of neutral hydrogen with column density N_{HI} moving with a bulk velocity v_{bulk} with respect to an observer. The neutral hydrogen will cause an absorption line at $\lambda = \lambda_{\text{Ly}\alpha}(1 + v_{\text{bulk}}/c)$ in the rest frame of the observer. Generally, the optical depth of a medium of length l is given as

$$d\tau = \sigma n dl, \quad (2.4.18)$$

where n is the particle number density. Since the column density is the integrated density along the LOS, the Ly α optical depth of such a cloud can be written as

$$\tau_{\text{Ly}\alpha}(v) = \sigma_{\text{Ly}\alpha}(v) N_{\text{HI}}. \quad (2.4.19)$$

While usually Ly α absorption exhibits a Voigt profile, Ly α forest systems such as the hot, low-density IGM are well described by Doppler line profiles (Meiksin 2009). Thus, the exponential approximation for Eq. 2.4.15 can be used. Inserting Eq. 2.4.2 with a Voigt line profile function (Eq. 2.4.13) and the definition for Thomson scattering, i.e.

$$\sigma_{\text{T}} = \frac{8\pi}{3} \left(\frac{e^2}{m_e c^2} \right)^2, \quad (2.4.20)$$

it follows that

$$\tau_{\text{Ly}\alpha}(v_{\text{line}}) = c \sqrt{\frac{3\pi\sigma_{\text{T}}}{8}} f_{\text{Ly}\alpha} \frac{N_{\text{HI}} \lambda_{\text{Ly}\alpha}}{\sqrt{\pi}b} \exp\left(-\frac{(v_{\text{bulk}} - v_{\text{line}})^2}{b^2}\right), \quad (2.4.21)$$

where $\lambda_{\text{Ly}\alpha} = 1215.67 \text{ \AA}$ is the Ly α line wavelength of hydrogen and $f_{\text{Ly}\alpha} \approx 0.4162$ the oscillator strength of the Ly α transition of a one-electron atom (see e.g. Goldwire 1968).

Equation 2.4.21 gives the Ly α optical depth of a warm gas cloud that exhibits a certain relative velocity v_{bulk} towards or away from an observer. It scales with the column density of HI and broadens or flattens with the temperature of the gas through the Doppler parameter b . Its position in a spectrum as seen by an observer depends on v_{bulk} .

Chapter 3

The SHERWOOD RELICS simulations

The SHERWOOD RELICS simulations (Puchwein et al. 2021 in prep., also see Gaikwad et al. 2020), the follow-up project of the SHERWOOD simulations by Bolton et al. (2017), are large-scale hydrodynamical simulations of the cosmic web, which aim to model the low-density IGM and, thereby, the Ly α forest. They include more than 20 different simulation runs with varying properties such as warm and cold dark matter or varying photoionization and photoheating rates. The box sizes and particle number densities range between $(10 - 80 h^{-1} \text{ cMpc})^3$ and $2 \times 256^3 - 2 \times 2048^3$, respectively. Most of the runs were performed assuming a time-varying, spatially-homogeneous UVB model (Puchwein et al. 2019), whereas a single run deployed an inhomogeneous (i.e. patchy) UV radiation field from radiative transfer simulations (following Kulkarni et al. 2019a) based on the ATON code (Aubert & Teyssier 2008). The underlying code is a modified version of the P-GADGET-3 code, which is the subsequent version of the GADGET-2 smoothed-particle hydrodynamics code developed by Springel (2005). For the gravitational interactions and hydrodynamics, it uses a Tree-Particle-Mesh gravity solver and a smoothed-particle hydrodynamics scheme (Springel & Hernquist 2002), respectively.

3.1 Properties of the simulations

The simulations deploy the cosmological parameters $\Omega_m = 0.308$, $\Omega_\Lambda = 0.692$, $\Omega_b = 0.0482$ and $h = 0.678$ as constrained by Planck Collaboration et al. (2014), representing the cosmic matter, dark energy, and baryon density, and the Hubble parameter. For the mass fractions of hydrogen and helium $X = 0.76$ and $Y = 0.24$ is assumed, respectively. The seven models analyzed in this work are listed in Table 3.1. All of the runs were performed in a $(40 h^{-1} \text{ cMpc})^3$ volume with 2×2048^3 particles. This corresponds to a gas and dark matter mass resolution of $m_{\text{gas}} = 9.97 \times 10^4 h^{-1} M_\odot$ and $m_{\text{DM}} = 5.37 \times 10^5 h^{-1} M_\odot$, respectively. The gravitational softening length is set to $l_{\text{soft}} = 0.78 h^{-1} \text{ ckpc}$.

For photoionization, -heating and -cooling, external UVB models are deployed. Most hydrodynamical simulations of the IGM assume that the gas is in ionization equilibrium maintained by an external UVB. Although this is a good approximation at $z < z_r$, non-equilibrium effects during reionization are non-negligible. Hence, a non-equilibrium solver (Puchwein et al. 2015) is used. Since the simulations aim to model the low-density IGM, gas particles with a density $\rho > 1000 \bar{\rho}_b$, where $\bar{\rho}_b$ is the mean cosmic baryon density, and a temperature $T < 10^5 \text{ K}$ are considered as collisionless star particles to

Table 3.1. Investigated simulation runs

Name	Label	z_r	ϵ_{HI} factor	Properties
40-2048	default	6.2	1	Reference model
40-2048hot	hot	6.2	2	Hotter IGM
40-2048cold	cold	6.2	0.5	Colder IGM
40-2048zr75	early	7.5	1	Early reionization end (modified $\Gamma(z)$)
40-2048zr675	intermediate	6.75	1	Intermediate reionization end (modified $\Gamma(z)$)
40-2048patchy	patchy	5.2	-	Patchy UVB from radiative transfer simulations
40-2048homog	homogeneous	5.2	-	Reionization history identical to patchy model

Notes – Different simulation runs used from the SHERWOOD RELICS suite (Gaikwad et al. 2020; Puchwein et al. 2021, in prep.). The label here is used to make distinguishing them more intuitive. The columns contain (i) the name of the simulation run, (ii) our assigned label, (iii) redshift at which the reionization process completes, (iv) the deployed H I photoheating factor, and (v) a short explanation of the properties of each model.

accelerate the computations. This procedure, however, does not realistically reproduce galaxies, but still allows a sufficiently accurate modeling of the IGM (Viel et al. 2004).

As mentioned above, except for the patchy run, all of the SHERWOOD RELICS simulations use a spatially homogeneous, time-varying UVB model from Puchwein et al. (2019), which causes H I and He II reionization process to complete at $z \approx 6.2$ and $z \approx 2.8$, respectively. Deploying other UVB models e.g. from Haardt & Madau (2012) resulted in an artificial acceleration of the reionization process where H I reionization finishes at $z \approx 11$. For the *hot* and *cold* IGM model, the H I and He I photoheating rates were changed by a factor of 0.5 and 2, and the He II photoheating rate by 0.66 and 1.5, respectively, to achieve a varied heating of the gas and, thereby, a difference in IGM temperatures. The *hot* model, though, has a flatter $T - \Delta_b$ relation (Kulkarni et al. 2019a), and the ionization state of the gas also differs due to the temperature-dependent recombination rate (see Eq. 2.3.3). The *early* and *intermediate* models were adjusted to finish reionization at $z = 7.5$ and $z = 6.75$, respectively. This is achieved by linearly rescaling the redshift axis of the external UVB at $z > 5$ by a factor of 1.12 and 1.24, respectively.

For the *homogeneous* run, the reionization history and gas temperature were adopted such that they correspond to the mean of the patchy run. For both simulations, H I reionization completes at $z \approx 5.2$. The patchy run is a hybrid of radiative transfer and hydrodynamical simulations to model a patchy reionization process. The source model was developed by Kulkarni et al. (2019a): it implements the H I- and He I-photoionization rates and reionization redshift produced by post-processing the output of hydrodynamical simulations with an external, homogeneous UVB with radiative transfer simulations based on the ATON code (Aubert & Teyssier 2008). Thereby, it is possible to study the impact of the patchiness of reionization. Here, reionization redshift is defined as the redshift where a grid cell exceeds an H II fraction of 3%, which represents the onset of its reionization. The radiative transfer simulation populates halos with ionizing sources according to their mass and creates maps of z_r and Γ every 40 Myrs. In a second run of hydrodynamical simulations, the photoionization and reionization redshift maps produced by the radiative transfer code are used as the external UVB. However, since He II reionization only plays

a role in the late ionization and thermal evolution of the IGM, i.e. at $z < z_r$, the He II photoionization and -heating maps are adopted from the spatially homogeneous UVB model from Puchwein et al. (2019).

3.2 Homogeneous and patchy UVB models

As mentioned previously, we will investigate simulations with both homogeneous and patchy UV radiation fields. These fundamentally different approaches have a significant impact on the evolution of the HI fraction: although results from homogeneous UVB models match IGM properties as observed in real Ly α forest spectra at $z < 5$, they do not realistically reproduce them at $z > 5$ (see Sect. 2.3.4).

Figure 3.1 shows a chronological evolution of the gas density, HI fraction, and gas temperature the SHERWOOD simulations (Bolton et al. 2017) assuming a homogeneous UVB in the left, middle, and right column, respectively. The top, middle, and bottom row depict slices through the simulation box at $z = (10, 8, 6)$, respectively, indicated in the top right corner of the right panel in each row. Although these are not the simulations investigated in this work, they still suffice to describe the evolution of these properties since they are based on the same code, but have slightly different conditions. Here, the photoionization and -heating rates are zero until $z = 9$, where the UVB kicks in. The top row, reflecting the state of the simulation box at $z = 10$, shows that the gas temperature is relatively low, although the temperature map already mimics the low- and high-density regions as seen in the gas density distribution (right panel). The middle panel, i.e. the HI fraction, shows that the gas is entirely neutral at this stage since there is no radiation to ionize or significantly heat the gas. In the middle row, at $z = 8$, the structure formation governed by the gravitational interaction of the gas particles already progressed (left panel). Here, the UV radiation field is already turned on, which is clearly visible: the right panel shows how the gas is heated homogeneously in the entire box, where the temperature in high-density regions is still slightly higher compared to low-density areas, though. Accordingly, the middle panel shows how the UV radiation starts to ionize the neutral gas and, thus, the HI fraction decreases – similarly to the temperature – in a homogeneous manner. In these simulations, the reionization process completes before $z \approx 6$. The bottom row therefore reflects the state of the simulation after reionization has finished. The gas still gets uniformly heated (right panel). However, high-density structures (i.e. galaxies) that now clearly reside in filaments (as can be seen in the right panel) show higher temperatures than other low-density regions, i.e. voids. At this point, the HI fraction has already increased drastically. However, it is visibly lower in regions with higher densities. On the contrary, low-density areas show lower HI fractions, which results from reionization in dense regions progressing slower due to higher gas number densities. This is the major difference to simulations with a spatially patchy UVB.

A chronological evolution from $z = 8$ to 5 of the gas properties and the UVB in radiative transfer simulations by Kulkarni et al. (2019a) as used in the SHERWOOD RELICS project is depicted in Fig. 3.2. The upper, middle, and bottom row show the time evolution of the HI fraction, gas temperature, and the HI photoionization rate, respectively. In contrast to the simulations in this work, though, the depicted radiative transfer simulations use box sizes of $160 h^{-1} \text{ cMpc}$. At $z = 8$, while HI reionization progresses, the top row shows ionized bubbles populated with ionizing sources. The distribution of ionizing

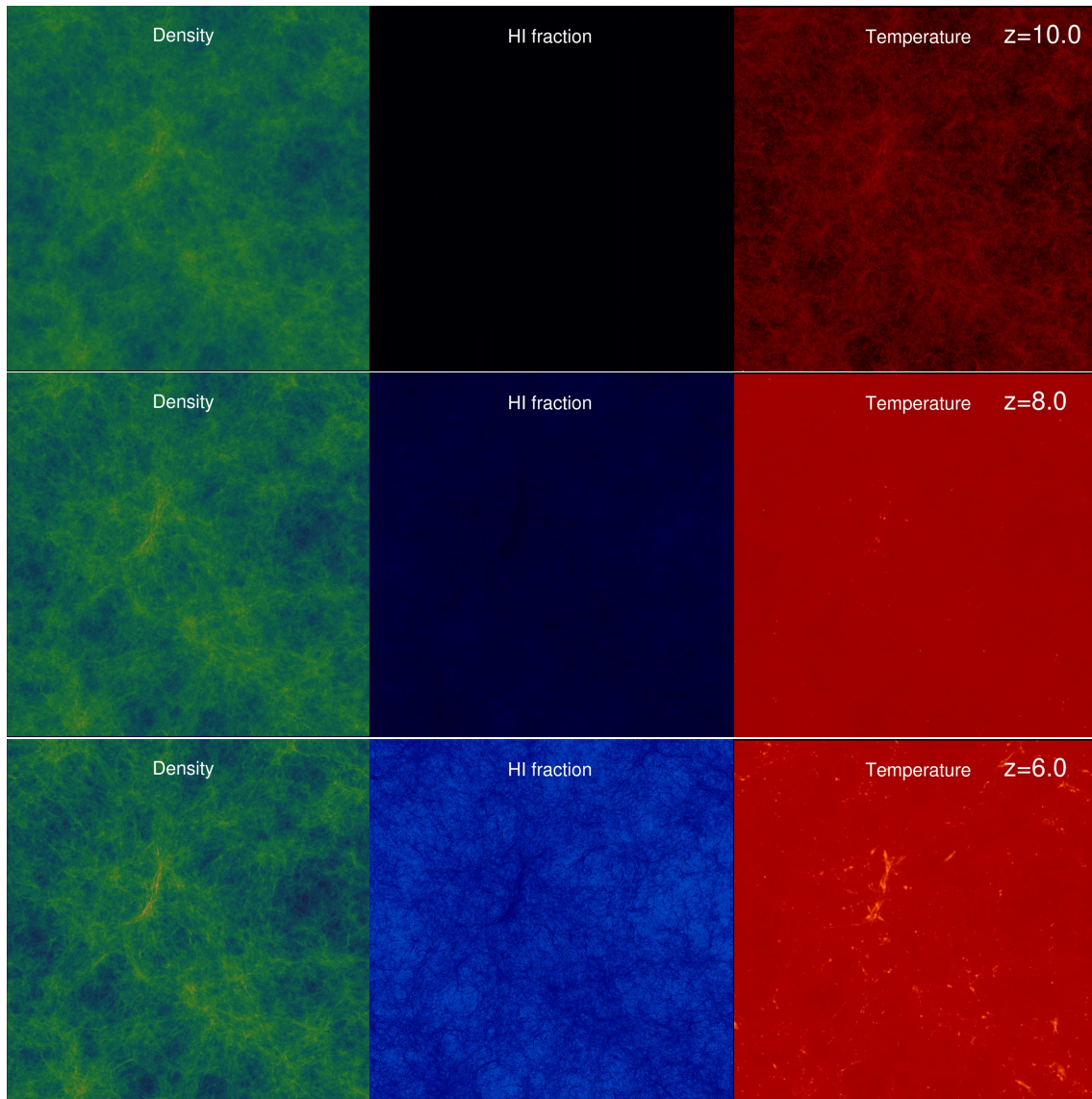


Figure 3.1. Snapshots of the evolution of the gas density (left column), HI fraction (middle column), and gas temperature (right column) from $z = 10$ to 6 (from top to bottom) in the SHERWOOD simulations by Bolton et al. (2017). The UVB is time varying but spatially homogeneous and sets in at $z = 9$. Each panel represents a slice through the simulation box with side lengths of $40 h^{-1} \text{ cMpc}$ at each redshift indicated in the upper right corner of the right panel in the respective row. While the formation of structures progresses with time, the HI fraction and gas temperature increases spatially homogeneous until the gas becomes highly ionized. Credit: James Bolton. Images are available from: <https://www.nottingham.ac.uk/astronomy/sherwood/media.php> (date of last access: December 29, 2020 03:31 pm).

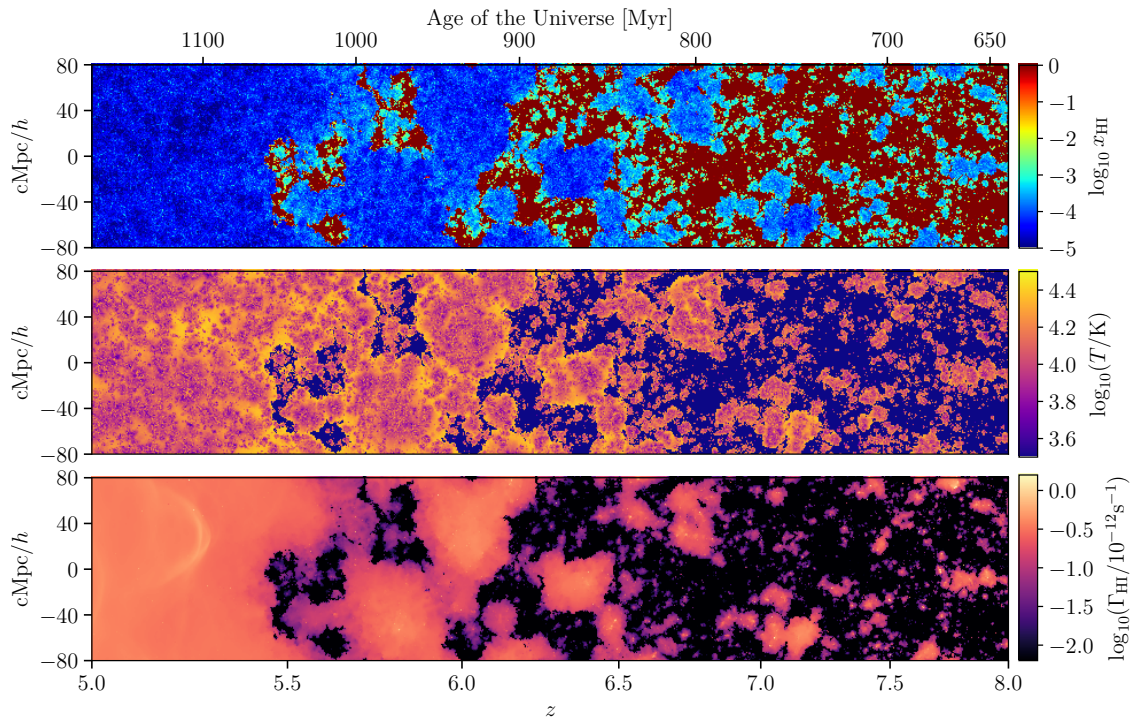


Figure 3.2. Evolution of the H I fraction (upper panel), gas temperature (middle panel), and the hydrogen photoionization rate (bottom panel) from $z = 8$ to 5 in the radiative transfer simulations by Kulkarni et al. (2019a). The UVB is time-varying and spatially-inhomogeneous (patchy) due to an irregular distribution of ionizing sources. These sources produce bubbles of hot, reionized gas that grow with time until they eventually overlap and fill the whole space. Adopted from Kulkarni et al. (2019a).

sources can be inferred from Γ_{HI} as to be seen in the bottom row: there are certain areas where the radiation field is particularly strong, which correlates with the ionized bubbles in the top row. There are also large gaps between these sources, where the ionizing radiation has not reached to yet. The photoheating radiation created by these sources heats the gas within the bubbles. In the space between bubbles the gas does not get significantly heated. With time, the bubbles of highly ionized, hot gas expand until they eventually begin to overlap. At $z \lesssim 5.5$, the entire gas in the box is heated up and highly ionized, which marks the end of the H I reionization era. From this point on, the radiation field is almost perfectly spatially homogeneous.

3.3 Available simulation data

Data reflecting the properties of the gas in the simulation boxes along artificial LOSs are provided at specific redshifts. For the *default*, *hot* and *cold* IGM, and the *early* and *intermediate* reionization end runs these snapshots are available at $z = 4 - 12$ at $\Delta z = 0.1$ intervals. The *patchy* and *homogeneous* model provide them at $z = (4.2, 4.6, 4.8, 5.0, 5.4, 5.8, 6.0, 6.4)$. At each redshift, the data contain all important properties. As well as the main details such as z , Ω_m , Ω_Λ , Ω_b , h , X etc., the data also provide the gas properties such as position, density, relative density, temperature, H I fraction, and peculiar velocity. The

optical depths of each pixel were calculated from the properties it depends on during the runtime of each simulation as described in [Bolton et al. \(2017\)](#).

Chapter 4

Methods

In the following Chapter we will describe the steps of our data analysis. In Sect. 4.1, we explain how the mock Ly α spectra are constructed from the simulations. We scale the spectra from models assuming a homogeneous UVB to observed effective optical, which is illustrated in Sect. 4.2. Our detection algorithm and criteria for spikes and underdensities are explained in Sect. 4.3. In Sect. 4.4, we discuss our method developed to measure spike and underdensity widths. The adding of noise to the mock spectra and the application of noise filtering to the noisy spectra is described in Sect. 4.5.

4.1 Synthetic quasar spectra

The resulting data of the simulations provide all the necessary information about the underlying gas properties in the simulation box. To construct sample spectra for each simulation run and redshift, 5 000 random LOS are cut through the simulation box. Along the x -, y -, and z -axis, the LOS are arranged in a 50×50 , 40×40 , and 30×30 grid, respectively. This corresponds to 2 500 LOSs in the x -, 1 600 in the y -, and 900 in the z -direction. Along each LOS, all underlying properties of the gas such as H I fraction x_{HI} , gas temperature T , peculiar velocity v_g and density ρ_g are extracted.

The synthetic Ly α quasar spectra were provided by [Puchwein et al. \(2021\)](#) (in prep.) and, similarly to [Bolton et al. \(2017\)](#), and constructed using the gas properties along each LOS to calculate the contribution to the overall optical depth of each real-space pixel τ_{px} using Eq. 2.4.21. Here, N_{HI} is the H I column density of the respective pixel and $v_{\text{bulk}} - v_{\text{line}}$ the velocity difference between real- and velocity-space pixel. Hence,

$$v_{\text{bulk}} - v_{\text{line}} = (v_{\text{H}} + v_{\text{g}}) - v_{\text{px}}, \quad (4.1.1)$$

where v_{H} and v_{g} are the Hubble and peculiar gas velocity of the corresponding real-space pixel, respectively, and v_{px} the velocity of the velocity-space pixel. The overall optical depth in velocity space along the LOS is then given by the sum of the contributions to the optical depth of each individual real-space pixel, i.e.

$$\tau = \sum_{\text{px}} \tau_{\text{px}}. \quad (4.1.2)$$

Assuming a continuous relative background emission of $F = 1$, the normalized transmitted flux of a synthetic background can then be calculated as

$$F = \exp(-\tau). \quad (4.1.3)$$

Figure 4.1 shows an example of a Ly α spectrum extracted from the *patchy* simulation run at $z = 5.0$. The spectrum reveals the transmitted flux from an artificial background QSO along the LOS through the complete simulation box with a continuous emission at $F = 1$. It clearly shows the spike-shaped transmitted background emission resulting from low-density and highly ionized areas in the IGM along the LOS towards the background source.

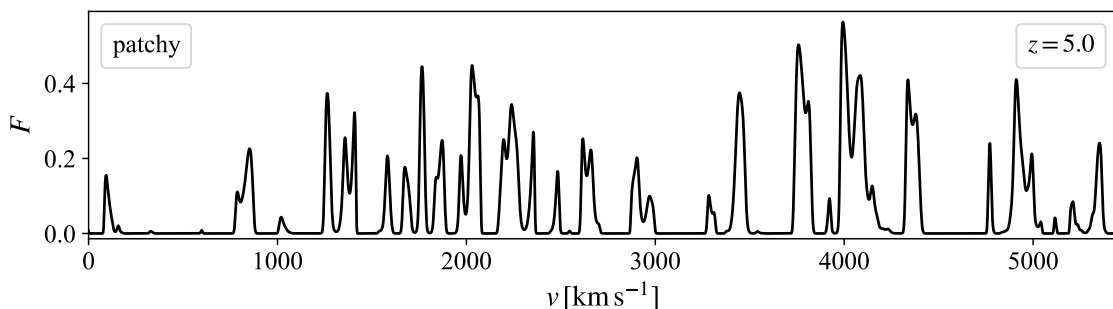


Figure 4.1. Ly α spectrum of an artificial background QSO with a continuous flux at $F = 1$ along a random LOS as extracted from the *patchy* UVB model at $z = 5.0$. A large fraction of the light gets absorbed due to the high H I fraction of the IGM, although there are regions where some light is transmitted and forms Ly α transmission spikes.

4.2 Scaling the spectra to observed effective optical depths

Comparisons of Ly α forest measurements of numerous QSOs with cosmological, hydrodynamical simulations deploying a homogeneous UVB model have shown that the modeling of Ly α spectra during reionization and towards its tail end shows an unrealistic evolution of the Ly α opacity (Becker et al. 2015). Instead, inhomogeneous (i.e. patchy) UVB models yield results that are much more consistent with observations (Kulkarni et al. 2019a). To make comparing the different simulation runs more consistent, the spectra from the *homogeneous* reionization model are scaled to the mean transmission of the *patchy* model since they have equal reionization histories. Similarly, the *default*, *hot*, and *cold* IGM as well as the *intermediate* and *early* reionization models are scaled to the effective optical depth τ_{eff} of the IGM as observed by Bosman et al. (2018), which relates to the mean flux as

$$\bar{F} = \exp(-\tau_{\text{eff}}). \quad (4.2.1)$$

Bosman et al. (2018) constrained the IGM Ly α opacity \bar{F} at $4.9 < z < 6.1$ from a sample of 62 QSOs at $z > 5.7$. Since $\tau \sim x_{\text{HI}}$, this quantity is also scaled by the same amount. A comparison between the Bosman et al. (2018) and our data from the *patchy* reionization model at $z = 5.0 - 6.5$ is shown in Fig. 4.2. The observed τ_{eff} from Bosman et al. (2018) is depicted by the blue line and data points. The black line represents τ_{eff} extracted from the

patchy reionization model. The simulation shows a similar trend as the observational data from [Bosman et al. \(2018\)](#). Since their data only apply at $z < 6$, we linearly extrapolate these at $z = 5.8 - 6.0$ in order to apply them for scaling spectra at higher redshifts.

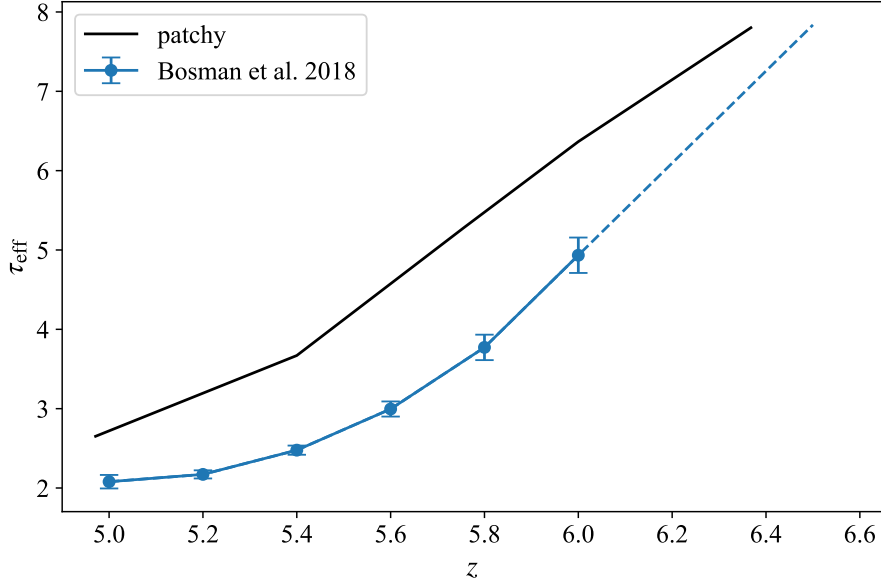


Figure 4.2. Observational IGM Ly α opacity (effective optical depth τ_{eff}) by [Bosman et al. \(2018\)](#) at $5.0 < z < 6.0$ (blue data points and solid, blue line) extrapolated to higher redshifts (dashed, blue line), and τ_{eff} as observed in the *patchy* reionization model (black line). The evolution τ_{eff} as constrained by the observational data is very similar to that from the *patchy* model.

The amplitude of the UVB and, thereby, the photoionization rate Γ_{HI} is unknown. According to Eq. 2.3.3, the HI number density n_{HI} depends on Γ_{HI} . If $n_{\text{HI}} \ll n_{\text{HII}}$ (and $n_{\text{HI}} \ll n_e$), which applies to the reionized IGM, where $n_{\text{HI}} \sim 10^{-4}$, the right side of Eq. 2.3.3 is practically independent of n_{HI} . Hence, it follows that

$$n_{\text{HI}} \sim \Gamma_{\text{HI}}^{-1} \quad (4.2.2)$$

and, thereby, Eq. 2.4.18 yields

$$\tau \sim \Gamma_{\text{HI}}^{-1}. \quad (4.2.3)$$

The above relation can be used to rescale τ to a different value of Γ_{HI} . Since the real value of Γ_{HI} is unknown, τ is rescaled such that the observed mean flux is reproduced. The scaling is carried out by adapting the mean transmission of all LOSs for every run at each redshift given by

$$\overline{F}(\alpha, z) = \overline{\exp\left(-\frac{\tau(z)}{\alpha(z)}\right)}, \quad (4.2.4)$$

where $\alpha(z)$ is the factor by which Γ_{HI} is being rescaled, to match the target transmission

$$\overline{F}_t(z) = \exp(-\tau_{\text{eff}}(z)), \quad (4.2.5)$$

where $\tau_{\text{eff}}(z)$ is the effective optical depth of the *patchy* run or as observed by [Bosman et al. \(2018\)](#), depending on the model whose spectra are being scaled. To achieve this, we use Newton's method to approximate the value of $\alpha(z)$ such that

$$f(\alpha, z) = \overline{F}_t(z) - \overline{F}(\alpha, z) = 0. \quad (4.2.6)$$

Here, we choose a precision of 10^{-6} , hence where $f(\alpha, z) < 10^{-6}$.

An example of the effect of the scaling of a spectrum from the *default* run, deploying a homogeneous UVB model, at $z = 5.4$ can be seen in Fig. 4.3. At this redshift, the simulated spectrum overpredicts the observed mean transmission from Bosman et al. (2018).

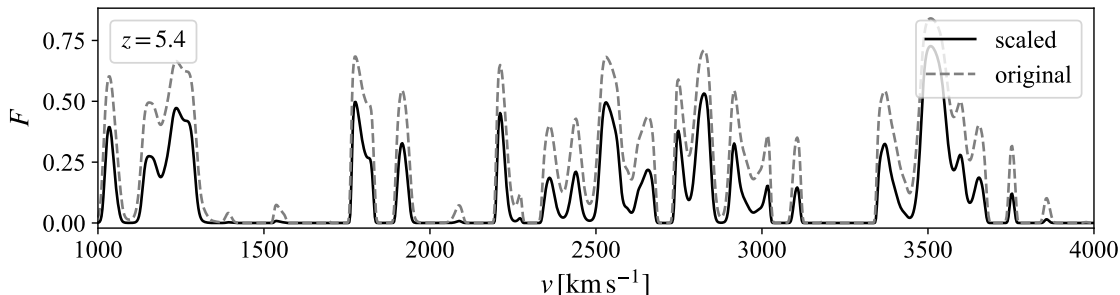


Figure 4.3. Transmitted Ly α flux F as extracted from the reference model (dashed, gray line) and scaled to the observed effective optical depth τ_{eff} of Bosman et al. (2018) (solid, black line) for a random LOS at $z = 5.4$. The simulated spectrum overpredicts the observed mean transmission.

4.3 Measuring transmission spike and underdensity properties

In the following, we describe our method for detecting spikes and underdensities in order to measure their properties. In essence, the concept follows Garaldi et al. (2019), although we will apply changes to it later on in the course of this work.

4.3.1 Detection criteria

As in Garaldi et al. (2019), the height of the transmissions spikes h_s is defined as the fraction of normalized transmitted flux at the local maximum F_{max} of each spike. The minimum flux for a spike to get detected is set to be $F_{\text{max}} \geq 0.05$. The width of each spike corresponds to the number of pixels left- and rightwards of the local maximum with $F \geq \alpha h_s$, where $\alpha = 0.5$. This corresponds to the full width at half maximum (FWHM). Due to the limited resolution of the simulation data, the position of the FWHM can lie between two spectral pixels. To compensate for this, the exact pixel position of the FWHM (and thereby the width of the spike) is calculated by linear interpolation of the pixels before and after crossing the threshold value.

Likewise, the properties of the underdense regions are detected. The intensity of an underdensity is defined by the density contrast at the local minimum δ_{min} . Here, δ is related to the mean gas density via Eq. 2.1.1. The maximum density contrast for a region to be categorized as underdense is $\delta_{\text{min}} \leq -0.5$. The extent of the underdense region is defined as the set of pixels left- and rightwards of the local minimum with $\delta \leq \beta \delta_{\text{min}}$, where $\beta = 0.5$ (i.e. FWHM). The exact position of the edges is again determined by linear interpolation of the two pixels before and after the excess of the FWHM.

4.3.2 Detection algorithm

Our detection algorithms for spikes and underdensities are identical: first, all local extrema of the respective quantity along the LOS are sorted by amplitude. Then, starting from the greatest extreme value, the algorithm collects all data points left- and rightwards of it that meet the defined criterion for the quantity and assigns these to the respective extremum. Trying to find the next extreme value, the algorithm skips all data points that have already been assigned to previously detected extrema. When assigning pixels to an extreme value, as soon as a data point was already assigned to a previously detected extremum, the algorithm aborts right before that pixel and marks it as the border of the currently investigated extremal value. In doing so, overlapping spikes and underdense regions are avoided. This lets the algorithm prioritize the measurement of greater extrema (i.e. spikes and underdensities). The code also respects the periodic boundary conditions of the simulations and, thus, also detects spikes at the simulation box edges.

4.3.3 Connecting spikes to the transmitting, underdense regions

In order to connect a transmission spike to the underdense region that produced the flux transmission, the position of the spatial pixel in the void (and, therefore, the position of the gas) is transformed from real into velocity space by adding the respective peculiar gas velocity v_g to the Hubble velocity v_H (based on their real-space position), i.e.

$$v = v_H + v_g. \quad (4.3.1)$$

All spikes whose pixel with the maximum flux (i.e. h_s) falls into the resulting extent of the underdensity are then connected to the void.

The result of this procedure is depicted in Fig. 4.4. The upper panel shows the transmitted flux of the synthetic background QSO. The detected transmission spikes are highlighted with red-shaded rectangles. The width and upper edge of the rectangle represent the measured width and height of the spike, respectively. In the second panel, the density contrast plotted as $\log_{10}(1 + \delta)$ reveals the detected underdense regions along the LOS. Here, the width (extent) and height (relative underdensity) of the regions are represented by the blue-shaded rectangles. The gray, dashed lines indicate the pixel in the density field (i.e. in real space) and, consequently, the underdense area to which a spike has been connected. The third and bottom panel show the H I fraction x_{HI} and temperature T of the gas, respectively.

In order to investigate the relation of spike properties to the characteristics of the IGM, the gas properties (i.e. temperature T , gas density contrast δ , H I fraction x_{HI}) along the LOS need to be related to each spike. For the spike height h_s , we assign the properties from the pixel in the connected underdensity of each spike that is closest to the pixel of the spike maximum in velocity space (see the gray, dashed lines in Fig. 4.4). The position of the pixels in velocity space can be calculated using Eq. 4.3.1. Furthermore, we relate the spike width w_s to the mean of each gas property over all pixels throughout the full extent of the spike-producing underdensity connected to the respective spike.

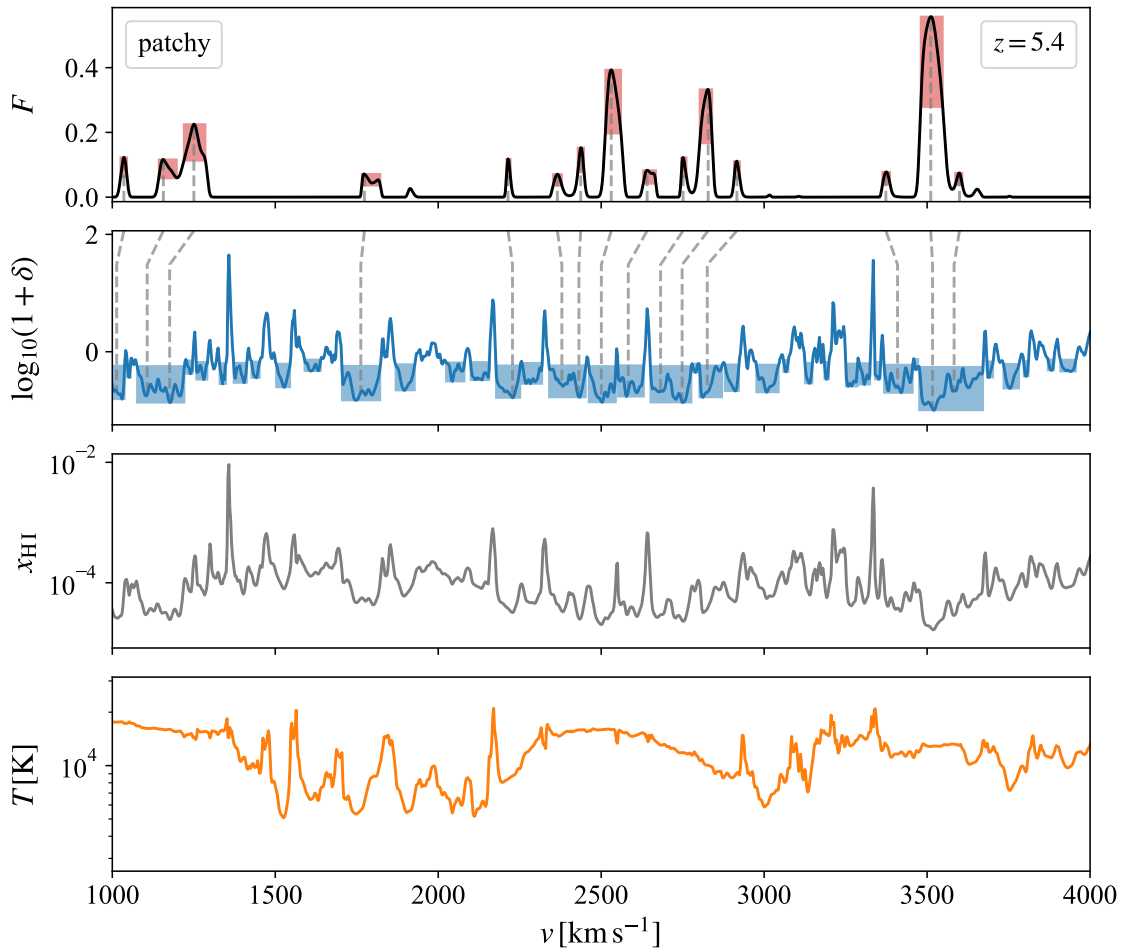


Figure 4.4. Transmitted Ly α flux F (upper panel), density contrast δ (second panel), H I fraction x_{HI} (third panel), and gas temperature T (bottom panel) along a random LOS at $z = 5.4$ extracted from the simulation with the *patchy* reionization model (inhomogeneous UVB). The red- and blue-shaded rectangles indicate the detected transmission spikes and underdense regions, respectively. The width of the rectangles represents their measured width at FWHM. The upper (bottom) edge of the red-shaded (blue-shaded) rectangles indicate the maximum height (depth) of the spikes (underdensities). The gray, dashed lines indicate the pixel in the underdense region a spike has been connected to (i.e. the corresponding real-space pixel). The two upper panels show that each transmission spike is produced by an underdensity, whereas not all underdensities cause the appearance of spikes.

4.4 Using a fixed threshold for spike and a dynamical for underdensity width measurement

In the previous section, spike and underdensity widths were measured at a relative height of their maximum and minimum value, respectively. This technique, though, has a great weakness: it measures the spike width at different optical depths τ and the threshold value for measuring the underdensity widths has to be chosen rather arbitrarily without a clear motivation. Since τ depends on the underlying gas properties, and the width of spikes and voids is being measured at arbitrary heights, these two quantities are not correlated with one another. In fact, [Garaldi et al. \(2019\)](#) only found a weak, redshift-dependent linear relation between the two. Thus, we assume that measuring the spike and underdensity widths at fixed, consistent values is physically more plausible and might result in a better correlation between the previously investigated properties.

Now, the width of transmission spikes is defined as the number of pixels with $F \geq 0.025$. The minimum value for detection is set to be double the threshold, i.e. $F \geq 0.05$, to ensure that the width is always measured below half maximum. This corresponds to the previously defined minimum height. Furthermore, since the transmitted flux depends on the density contrast, it is possible to choose the thresholds for underdensity width measurement consistently. To do so, every spectral pixel of a LOS in velocity space is correlated with all pixels in real space that fall into its extent. The former contains information about the transmitted flux F , while the latter provides the gas density contrast δ . The density contrast δ of all spatial pixels is then plotted against the flux of the respective spectral pixel.

Figure 4.5 shows the relation between gas density contrast δ and flux F for the *patchy* reionization model for all 5 000 LOSs through the simulation box at $z = 5.4$. The narrow distribution shows a correlation between the two quantities for all values with $F \gtrsim 0$. Thus, when measuring the spike width at a fixed value, it is possible to extract the distribution of δ at that very flux (i.e. the flux at the spike edges) and use a statistical measure of it to measure the extent of the underdense regions for a given model and redshift. This method is dynamical since the threshold value depends on both the model as well as the redshift.

By applying this method we expect an improved correlation between spike and underdensity widths if the threshold for underdensity width measurement is dynamically adapted to the distribution of δ at the chosen threshold flux. Here, we use the 95th percentile of δ at the previously defined threshold for spike widths estimated over all LOSs for each redshift separately and use it as the fixed value for measuring the widths of the underdense areas at the respective redshift. We found that using other statistical measures (e.g. mean or median) resulted in detected underdensities being split up into much smaller sections, and a large number of underdensities were not detected under these criteria. Thus, we chose a value for the density threshold close to the upper limit of the distribution seen in Fig. 4.5 at $F = 0.025$ at each respective redshift.

Figure 4.6 plots the thresholds at which the underdensity widths were measured at each redshift for all investigated reionization models. It shows that at $z \gtrsim 5.5$ these are now measured at lower density contrasts than before ($\log_{10}(1-0.5) \approx -0.3$) for the *default*, *hot*, and *cold* IGM, as well as the *intermediate* and *early* reionization model. In case of the *patchy* and *homogeneous* model, this applies for all redshifts. Hence, we now inspect

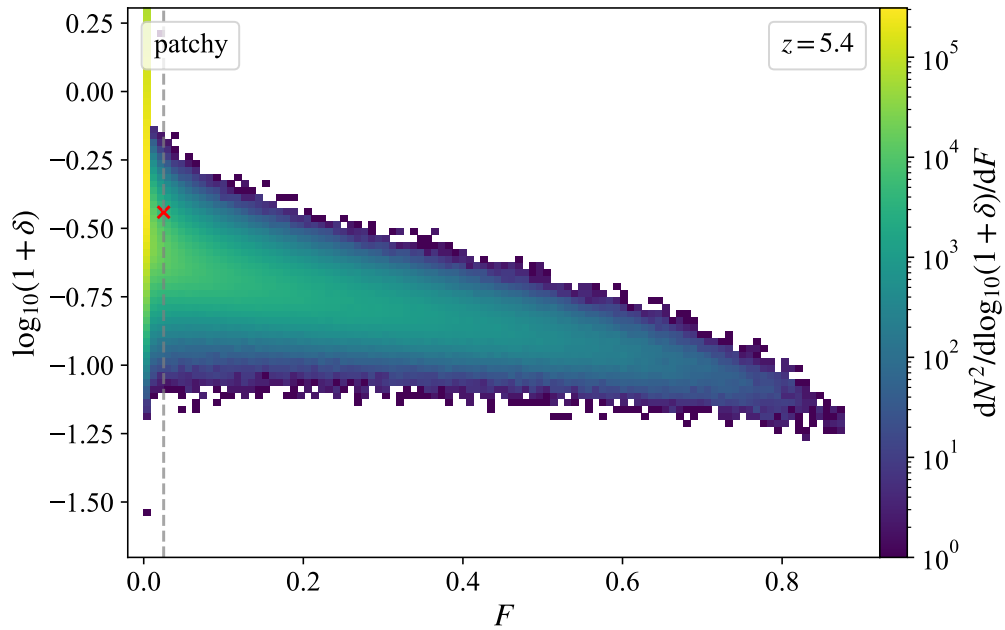


Figure 4.5. Relation between gas density contrast δ and flux F for the *patchy* ionization model at $z = 5.4$. The plot includes all spectral pixels of all 5 000 LOSs through the simulation box. The gray, dashed line indicates $F = 0.025$, and the red cross marks the 95th percentile of δ at the spike edges.

regions that are even less dense than those investigated previously. Similarly, Fig. 4.7 plots the density contrast measured at the spike edges ($F = 0.025$ here) against the mean flux \bar{F} averaged over all 5 000 LOSs in the simulation boxes of each run at each redshift $z = 5.0 - 6.4$.

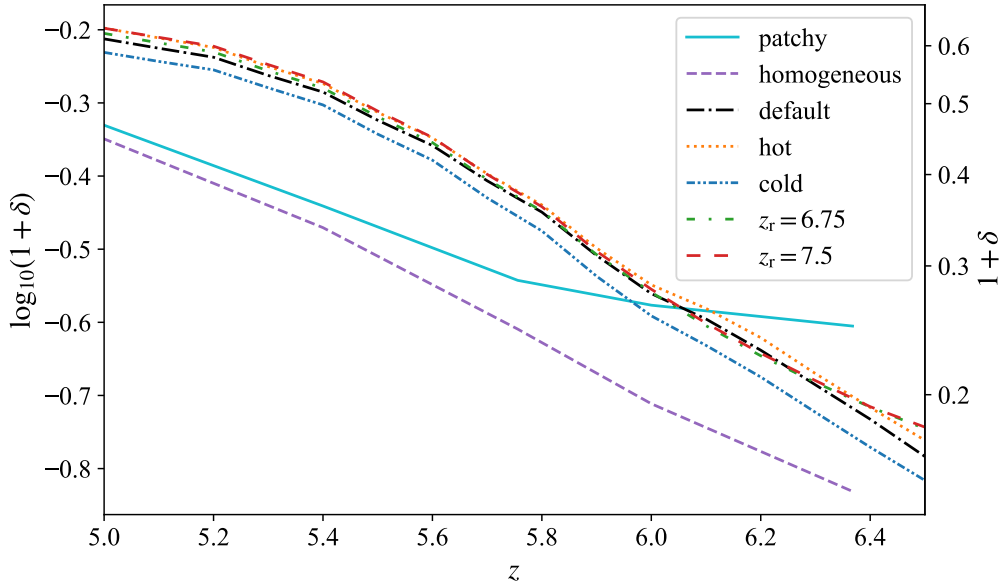


Figure 4.6. Threshold values δ for measuring of the underdensity widths at each redshift z for all investigated simulation runs. Here, δ is the 95th percentile of the density contrasts at the spike edges (i.e where $F = 0.025$) in all LOSs at each individual redshift.

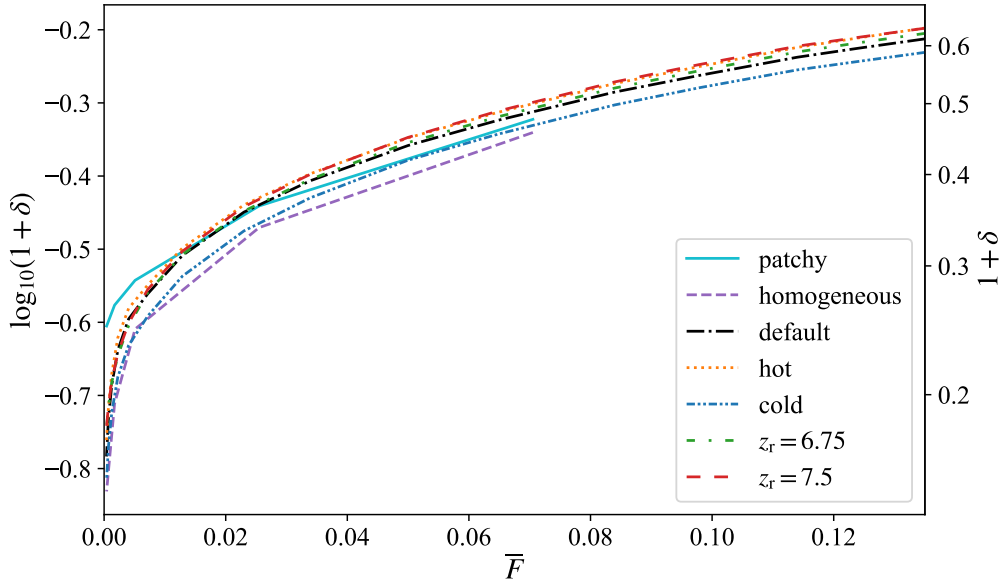


Figure 4.7. Threshold values δ for measuring of the underdensity widths vs. mean flux \bar{F} for all models. Here, δ is the 95th percentile of the density contrasts at the spike edges (i.e. where $F = 0.025$) in all LOSs. \bar{F} is the mean of all 5 000 LOSs in the simulation box at each redshift $z = (5 - 6.4)$.

4.5 Adding noise to create realistic spectra

In reality, observational data suffer from different physical and instrumental effects that produce noise in a spectrum taken by a telescope such as photon shot noise (i.e. Poisson noise), dark current, and read-out noise. Since the spectra extracted from the simulations have an infinite signal-to-noise ratio (S/N), we now degrade them to show realistic noise features to draw conclusions on the robustness of our results when comparing them to observations.

Both Poisson and Gaussian noise are added to the spectra. We assume a mean continuum level of 9×10^2 photons per pixel for the Poisson noise, which corresponds to $S/N \approx \sqrt{900} = 30$, and $\sigma_{\text{Gaussian}} = 2 \times 10^{-2}$ for the Gaussian noise, which corresponds to 2% noise being created by the statistical effects of electronic devices (e.g. CCD, read-out device etc.). Furthermore, we adopt a spectral resolution of $\sigma = 5 \text{ km s}^{-1}$ and a pixel width of $w_{\text{px}} = 2 \text{ km s}^{-1}$, which is equivalent to that of the MIKE spectrograph (Bernstein et al. 2003) used at the Magellan Telescopes at Las Campanas Observatory. An example of a noisy spectrum produced with the previously stated parameters is plotted as the black line in the upper panel of Fig. 4.8, which shows the same LOS as in Fig. 4.4.

The noise, though, prevents the clear measuring of spikes and introduces smaller spurious spikes resulting from statistical effects. These spikes are only a few pixels in width and, hence, contaminate the measurement. To clean the signal, we apply a Wiener filter and deconvolution. Consider a measured signal

$$f(v) = h(v) * s(v) + n(v), \quad (4.5.1)$$

where $h(v)$ is the impulse response of the signal-processing system (i.e. the line spread function of the spectrograph), $s(v)$ the (unknown) incoming signal, and $n(v)$ noise independent of $s(v)$ (e.g. Gaussian noise), and $*$ denotes a convolution. The unknown original signal can then be described by

$$\hat{s}(v) = g(v) * f(v), \quad (4.5.2)$$

where $\hat{s}(v)$ is an approximation of $s(v)$ with the least root mean square (RMS). The Wiener deconvolution is an approach to solve the above equation. In the frequency domain, it is expressed by

$$G(k) = \frac{H^*(k) S(k)}{|H(k)|^2 S(k) + N(k)}, \quad (4.5.3)$$

where $H(k)$ is the Fourier transform of $h(v)$ in the frequency domain, $S(k)$ the mean power spectrum density of the original, infinite S/N flux, and $N(k)$ the mean power spectrum density of the noise (i.e. difference between noisy and original flux $F_{\text{noise}} - F$). $S(k)$ is given by

$$S(k) = \overline{|\mathcal{F}F|^2}, \quad (4.5.4)$$

with the Fourier transform of the flux $\mathcal{F}F$, while $N(k)$ is given by

$$N(k) = \overline{|\mathcal{F}(F_{\text{noise}} - F)|^2}. \quad (4.5.5)$$

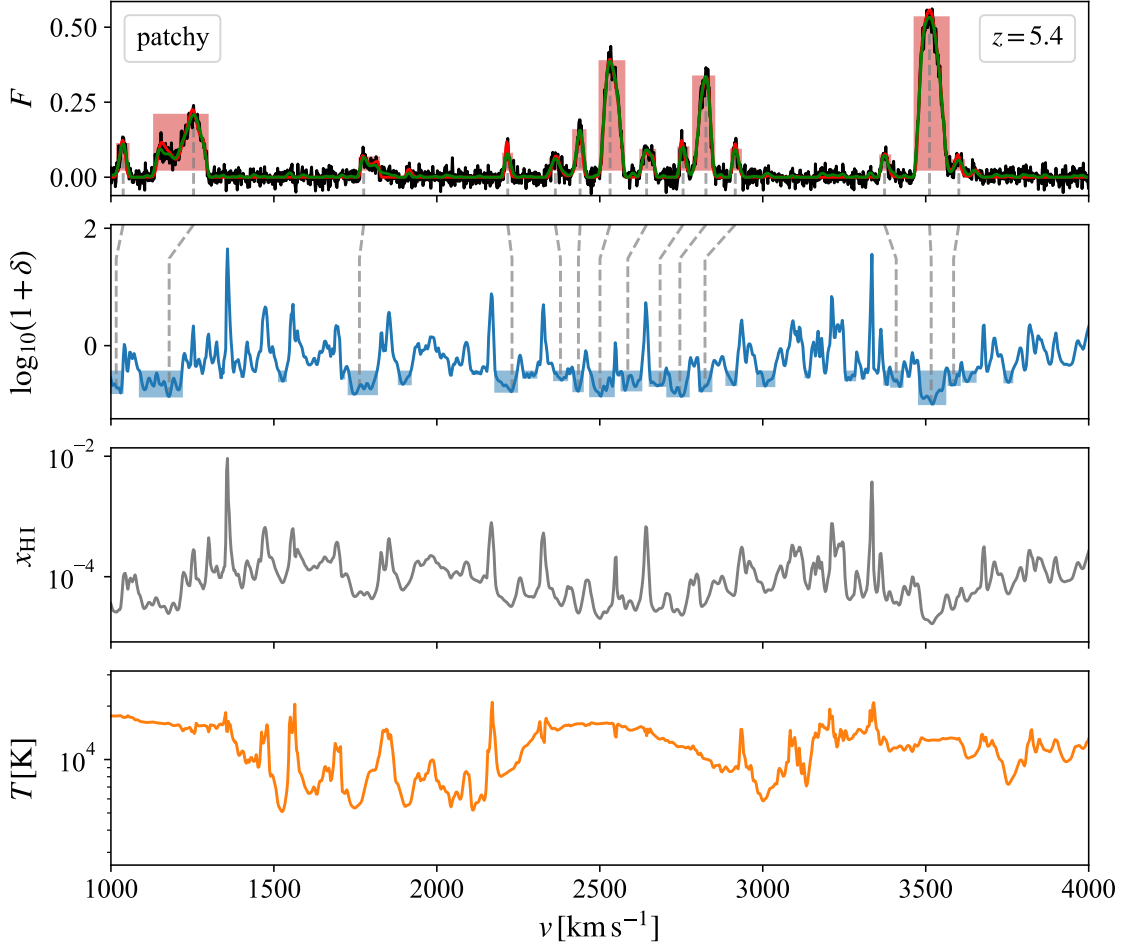


Figure 4.8. Same as Fig. 4.4. Here, the red, solid line in the upper panel shows the simulated spectrum without noise. The black and green solid lines show the noisy and filtered spectrum, respectively. Filtering the noise reliably reproduces the original spectrum.

For $h(k)$ we use a Gaussian kernel K , which – at a certain pixel px – is expressed by

$$h(k) = K(N_{\text{px}}, \text{px}) = \frac{w_{\text{px}}}{\sqrt{2\pi}\sigma} \exp\left(-\frac{(N_{\text{px}} - \text{px})^2}{2\left(\frac{\sigma}{w_{\text{px}}}\right)^2}\right), \quad (4.5.6)$$

where N_{px} is the number of pixels of the spectrograph (i.e. the noisy spectrum). Combining these two yields the Fourier transform of the noise-filtered flux as

$$\mathcal{F}F_{\text{decon}} = (\mathcal{F}F) G(k). \quad (4.5.7)$$

The noise-filtered flux is then given by the inverse Fourier transform of the above equation

$$F_{\text{decon}} = \mathcal{F}^{-1}(\mathcal{F}F_{\text{decon}}). \quad (4.5.8)$$

Wiener deconvolution is a great method for removing uncorrelated, additive Gaussian noise (e.g. read-out noise) and deconvolving the line spread function. However, it is not

Table 4.1. Wiener filtering and deconvolution RMS

N_{filter}	N_{analysis}	$\text{RMS}_{\text{unfil}}$	$\text{RMS}_{\text{fil+decon}}$	$\text{RMS}_{\text{fil+decon+pos}}$
10	4990	2.1802	0.8288	0.7504
50	4950	2.1804	0.8027	0.7229
100	4900	2.1798	0.8101	0.7346
250	4750	2.1795	0.8068	0.7282
500	4500	2.1798	0.7947	0.7084
1000	4000	2.1802	0.7934	0.7032
2500	2500	2.1804	0.7926	0.7044

Notes – RMS for different amounts of LOSs used for the Wiener filtering and deconvolution. The columns contain (i) the number of LOSs used to calculate the Wiener filter and deconvolution of the line spread function using a Gaussian kernel, (ii) the number of LOSs used for data analysis, (iii) the RMS of the unfiltered, noisy spectra, (iv) the RMS of the filtered and deconvolved spectra, and (v) the RMS of the filtered, deconvolved, and entirely positive spectra (i.e. negative flux values set to 0). All RMS are given in per cent. Here, the RMS is the average of all N_{analysis} LOSs at $z = 5.0 - 6.4$ for the *patchy* UVB model. In comparison, the method represented in the very right column (v) yields the best results in the range $N_{\text{filter}} \approx (50 - 250)$.

ideal for filtering Poisson noise since it depends on the incoming signal $s(\nu)$. Despite this, using this method as applied to numerically simulated spectra, where the original signal is known, yields good results.

The RMS serves as a measure of the effectiveness of the filtering, i.e. how much the filtered signal differs from the original spectrum with an infinite S/N. Here, we use $N_{\text{filter}} = 50$ LOSs to calculate the Wiener filter and deconvolution, and apply it to the remaining 4,950 LOSs for analysis. In doing so, we mimic a realistic scenario in which observational data would be filtered using simulated spectra. It is not required to use more LOSs to calculate the Wiener filter since we find that for $N_{\text{filter}} \rightarrow N_{\text{los}}$ the RMS does not change significantly. Besides, we want to keep a large amount of LOSs for analysis to maintain convincing statistics. Additionally, values with $F < 0$ are set to 0 since a negative flux is unphysical, which - as a side effect - significantly reduces the RMS. Table 4.1 shows an investigation of the dependence of the RMS with the different methods combined.

The result can be seen in the upper panel of Fig. 4.8. The black line reflects the noisy signal resulting from adding Gaussian and Poisson noise to the red line, which represents the original spectrum. The green line shows the result of applying the Wiener deconvolution to the noisy signal. To begin with, the noise level is similar to that of the observational data of UHS J043947.08+163415.7 with $\text{S/N} = 30.3$ (Fan et al. 2019). Furthermore, the filtered signal reproduces the original spectrum very well, although it underpredicts the peak heights in some cases. However, it is much smoother compared to the noisy signal and eliminates effects that cause individual spikes to be created purely by noise.

Finally, we run our detection algorithm on the filtered spectra. Again, the red-shaded rectangles represent the detected spikes. Comparing this result with Fig. 4.4 shows that roughly the same amount of spikes get detected, although some disappear under our detection criteria.

Chapter 5

Results

The evolution of the spike number density and H I fraction and their relationship are discussed in Sect. 5.1. Here, we also focus on the difference between the original and the scaled mock spectra, and how the simulation models differ from each other. We then investigate which parts of cosmic voids contribute to the absorption of background emission in Sect. 5.2. The relation between spike shapes and IGM density, temperature, and H I fraction, and spike width and underdensity extents are elaborated upon in Sect. 5.3 and 5.4, respectively. In Sect. 5.5, we compare the *homogeneous* and *patchy* UVB models and their impact on these relations. We discuss the influence of varying IGM temperature (Sect. 5.6) and reionization history as well as mean transmission (Sect. 5.7). Lastly, we check the robustness of our results against realistic observational noise in Sect. 5.8.

5.1 Evolution of transmission spike number density and neutral hydrogen fraction

The evolution of the spike number density dN_s/dL and the volume-weighted mean H I fraction \bar{x}_{HI} with redshift is shown in the upper and lower panels of Figure 5.1, respectively, for all investigated models. Here, \bar{x}_{HI} is averaged over the H I fraction x_{HI} of all 5 000 LOSs at each individual redshift. The left-hand side Fig. 5.1a shows the original, raw data, whereas the right-hand side Fig. 5.1b depicts the data where the optical depths have been scaled to the observed effective optical depths by Bosman et al. (2018) (see Sect. 4.2).

To begin with, the upper panel of Fig. 5.1a confirms that a homogeneous UVB (*default*, *hot* and, *cold* IGM model) causes physically implausible results that do not match with observational data (see e.g. Becker et al. 2015; Kulkarni et al. 2019a). At $z \approx 6$ the spike number density abruptly increases from almost none to $\sim 0.5 (h^{-1} \text{ cMpc})^{-1}$. For these models, reionization has ended already at $z = 6.2$ (see Table 3.1). The bottom panel shows that the mean H I fraction decreases logarithmically while reionization is progressing. This trend does not immediately plateau at $z = 6.2$, which is the redshift at which reionization is completed in these models, but at $z \approx 5.8$. It drops by a factor of $\sim 10^3$ over the whole period. However, except for the immediate appearance of spikes, this does not seem to have any visible effect on the further evolution of their number density. The *early* and *intermediate* reionization models, which also use a homogeneous UVB, do not show a drastic change in any of these quantities in the investigated redshift range due to

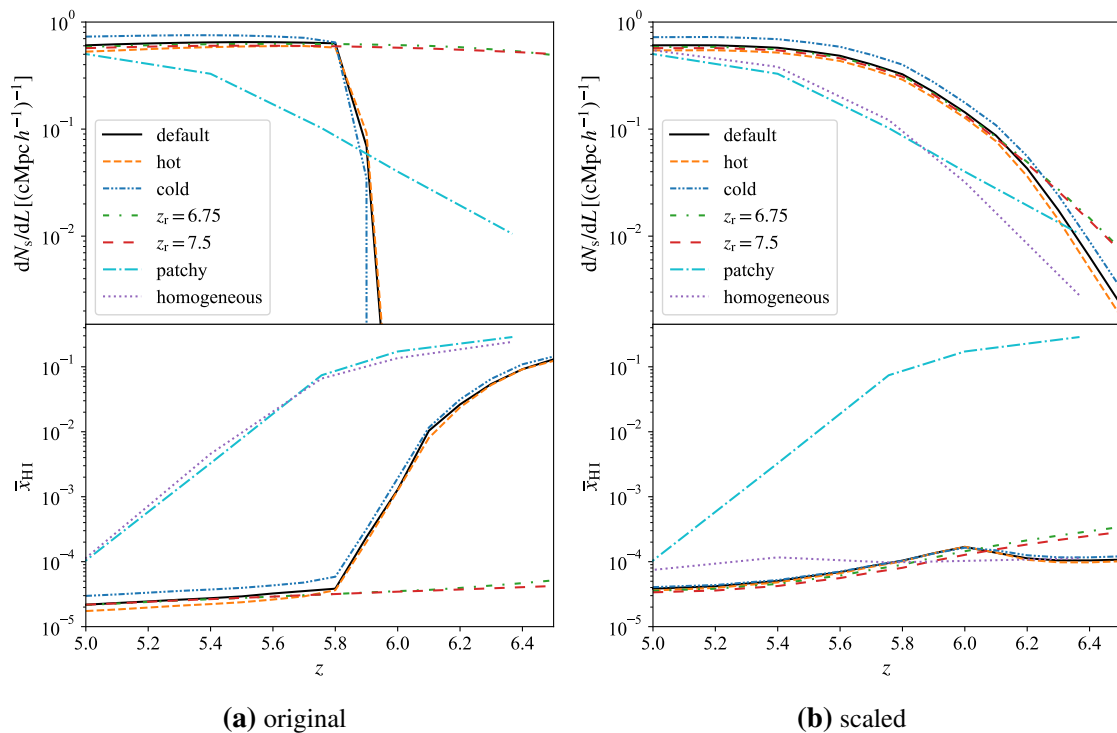


Figure 5.1. Number density of transmission spikes dN_s/dL and volume-weighted mean HI fraction \bar{x}_{HI} vs. redshift z (upper and bottom panels, respectively) for all investigated simulations. The left column 5.1a shows the original, unscaled runs, whereas the right column 5.1b shows the runs with scaled effective optical depths. Here, \bar{x}_{HI} is the average of all 5 000 LOSs at each redshift. The original spectra show that a homogeneous UVB only produces Ly α transmission spikes once the HI fraction exceeds a certain limit, while the patchy model reveals an increasing spike number density throughout the reionization process.

their HI reionization having ended at $z = 7.5$ and $z = 6.75$, respectively.

For the *patchy* model, which has completed the reionization process at $z = 5.2$, things progress differently. Although x_{HI} decreases similarly and shows the same order of magnitude, the spike number density increases continuously during this time frame: \bar{x}_{HI} decreases by a factor of $\sim 10^2$ while reionization is about to complete. Simultaneously, the number density of transmission spikes increases by a factor of ~ 10 to reach $0.4 (h^{-1} \text{ cMpc})^{-1}$ at $z = 5$. Hence, these quantities seem to have a negative correlation. The *homogeneous* run with equal parameters as the *patchy* run is not even to be seen in the upper panel since it does not allow any transmission that could produce spikes with a significant height in the investigated redshift range. This illustrates how the UVB affects the transmission of flux: if the UVB is spatially inhomogeneous, it leads to areas with high and low HI fractions. However, neutral regions do not prevent transmission by large, ionized bubbles. On the contrary, a homogeneous UVB leads to a spatially uniform increase in the ionization fraction, hence avoids transmission in all regions. Just as soon as a certain threshold for the HI fraction is exceeded, underdense regions allow transmission, which leads to an immediate increase of observed flux in voids.

When scaling the spectra of the models with a homogeneous UVB, the upper panel of Fig. 5.1b shows that the spike number density yields more realistic results even at $z > z_r$, i.e. during the EoR, which are very similar to the evolution of the *patchy* model and of

the same order of magnitude. At $z = 5$, all models show $\sim 5 \times 10^{-1} (h^{-1} \text{ cMpc})^{-1}$. On the contrary, the mean HI fraction now shows physically implausible results: \bar{x}_{HI} should increase while the spatially homogeneous UV radiation ionizes and heats the gas. The figure, though, shows that it decreases. This is possibly caused by the scaling parameter needed to scale the mean transmission of the spectra to that observed by [Bosman et al. \(2018\)](#) (or as in the *patchy* run) being too large to also create consistent results for x_{HI} . Scaling the photoionization rate by solving the complete ionization equilibrium equation (i.e. Eq. 2.3.3) might yield more consistent results at high HI fractions. However, during the end of the EoR, the IGM is not necessarily in ionization equilibrium, hence this approach may also be inappropriate for this purpose.

Comparing the spike number density in the models with different IGM temperatures also gives some insight into the spike physics. Both Fig. 5.1a and Fig. 5.1b reveal that the gas temperature has an impact on this quantity. The scaled spectra of the *cold* IGM model reveal a slightly higher density of spikes throughout the investigated redshift range, reaching more than $0.6 (h^{-1} \text{ cMpc})^{-1}$ at $z = 5$, compared to the *hot* model, which produces $\sim 0.45 (h^{-1} \text{ cMpc})^{-1}$ at this redshift. The *default* model is situated between the two. It seems that the relation stays proportional during the evolution of the simulations. The unscaled spectra show almost the same behavior, although it is different during the first appearance of spikes. At $z = 6$, the first spikes appear in the *hot* and *default* IGM model in the same amount with an almost identical evolution, whereas the *cold* IGM model shows the first spikes at $z = 5.9$. The spike density immediately reaches $\sim 0.5 (h^{-1} \text{ cMpc})^{-1}$ at $z = 5.8$. This suggests that the IGM temperature influences the spike shapes such that measuring the spikes at a fixed threshold results in a separation of spikes, which means that more spikes are being detected for lower IGM temperatures. The discrepancy also demonstrates that higher IGM temperatures produce larger ionization fractions – and, consequently, mean transmissions – amplifying thermal broadening, which will be discussed in the following section.

The data and the scaling technique show that a homogeneous UVB produces implausible results, especially during and closely after the end of reionization. The spatially homogeneous decrease of the HI fraction avoids any transmission until reaching a certain threshold. On the contrary, an inhomogeneous UVB allows transmission in certain areas throughout the investigated redshift range, which is in agreement with observations. In such models, areas populated with ionizing sources create a high degree of ionization of the IGM, whereas other areas stay neutral until eventually being reionized as the ionized bubbles grow. During this process, the neutral regions do not prevent transmission in highly ionized bubbles. The number density of spikes indicates a positive correlation between transmitted flux in the IGM and its degree of ionization: throughout the EoR, the size of the bubbles and their degree of ionization increase such that more and more spikes appear with decreasing redshift. Moreover, the models with different photoheating rates reveal that the IGM temperature affects the spike shapes since the spike number density drops with temperature when measuring spikes at a fixed threshold.

5.2 Contribution of individual pixels to absorption in underdensities

In order to establish how well transmission spikes can probe gas in underdense areas, we now examine the contribution of individual real-space pixels in underdense regions to the transmission of background emission, which causes the transmission spikes. We do this only with the original simulation data (i.e. unscaled spectra) to avoid adulteration of the results.

The fraction of flux being transmitted depends on the optical depth τ . Hence, in a first step we calculate τ for specific pixels (i.e. every 10th pixel) along a LOS as explained in Sect. 4.1. To approximate the contribution by surrounding pixels and, thereby, the full transmission along the LOS, the calculated optical depth of each pixel is scaled by a factor of 10 here. Figure 5.2 shows the result of this procedure for a specific spike at $v \approx 3400 \text{ km s}^{-1}$ of the LOS previously shown in Fig. 4.4. As before, the transmitted flux is represented by the black line in the upper panel. The colored curves show the flux absorbed by every 10th real-space pixel. The colored, dotted lines indicate from which real-space pixel each curve results. Likewise, the middle panel shows their optical depth as well as the overall optical depth (solid, black line) along the LOS. The blue line in the bottom panel depicts the gas density contrast. Red-shaded and blue-shaded areas highlight the detected spikes and underdensities, respectively. The gray, dashed lines show which underdensity and real-space pixel each spike was connected to.

In certain cases it is clearly visible that our technique to approximate the contribution of surrounding pixels by simply scaling by a specific factor leads to an overprediction of the actual optical depth and, therefore, flux. This does not affect our reasoning later on, but enables a clear distinction of thermal broadening and gas velocity.

As a second step, since we test the relation between spike and IGM properties, we want to understand which real-space pixels dominate the optical depth at the spike center. To do this, we calculate the optical depth of each real-space pixel in velocity space as previously. Then, the contribution by each real-space pixel to the optical depth of a spike peak is given by the optical depth at the velocity-space pixel of the spike maximum. The outcome of this method for the same LOS as in Fig. 4.4 is shown in Fig. 5.3. The latter figure, though, shows the complete LOS through the simulation box split over four rows. Each row shows three panels: original (unscaled) transmitted flux (solid, black lines) in the upper, density contrast (solid, blue lines) in the middle, and optical depth contribution per real-space pixel (solid, colored lines) in the bottom panel. As in the previous figure, the red- and blue-shaded areas represent the detected spikes and underdensities with the dashed, gray lines indicating which underdensity and real-space pixel a spike was assigned to.

The middle and upper panel of Figs. 5.2, 5.4, 5.5, and 5.6 show the optical depth and absorbed flux of individual real-space pixels in velocity space for the *patchy*, *default*, *cold*, and *hot* model, respectively. To begin with, it stands out that the gas is moving outwards from the underdense regions towards denser areas along the LOS, where the gas velocity is low in the center and increases towards the void edges (see e.g. [Hamaus et al. 2014](#)). The peculiar velocity increases with decreasing distance to the high-density region. This shows the effect of the peculiar gas velocity affecting the position in velocity space at which the pixels contribute to flux absorption. Furthermore, all plots show that

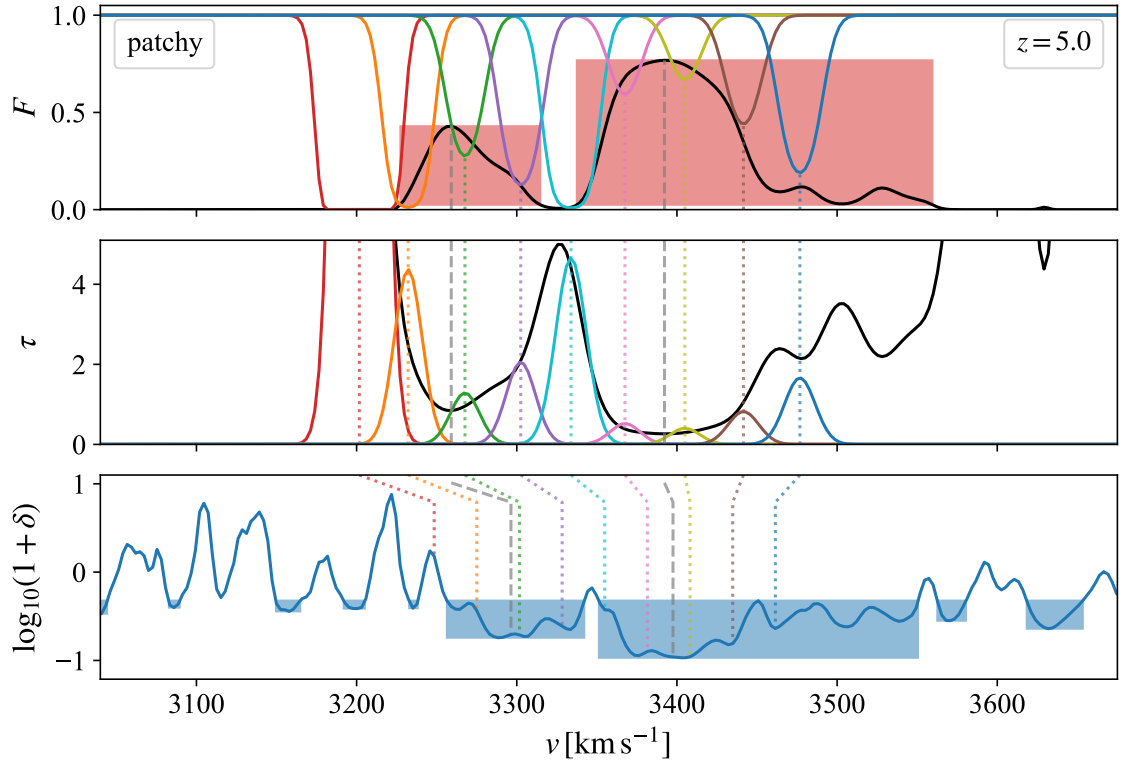


Figure 5.2. Contribution of individual pixels to the absorbed flux (i.e. optical depth) in underdense regions for the original data of the *patchy* reinization model at $z = 5$. The upper and bottom panel show the original (i.e. unscaled) transmitted flux (black line) and gas density (blue line), respectively, along the LOS depicted in Fig. 4.4. The flux and optical depth of individual pixels, represented by the colored curves in the first and second panel, respectively, was calculated for every 10th pixel and scaled by a factor of 10 to mimic the additional contribution by surrounding pixels. The individual colors here were randomly chosen to enable distinguishing the different curves. The solid, black line in the middle panel plots the overall optical depth. Red- and blue-shaded areas represent the detected spikes and underdensities, respectively. The gray, dashed lines depict to which underdense region and real-space pixel a spike has been connected. The colored, dotted lines show from which real-space pixel the calculated optical depth and flux result and hence represent the peculiar gas velocity along the LOS. The velocity-space position where the pixels cause absorption moves according to the peculiar velocity of the gas. The major contribution to the absorption at the spike peak results from the respective real-space pixel and its close neighbors.

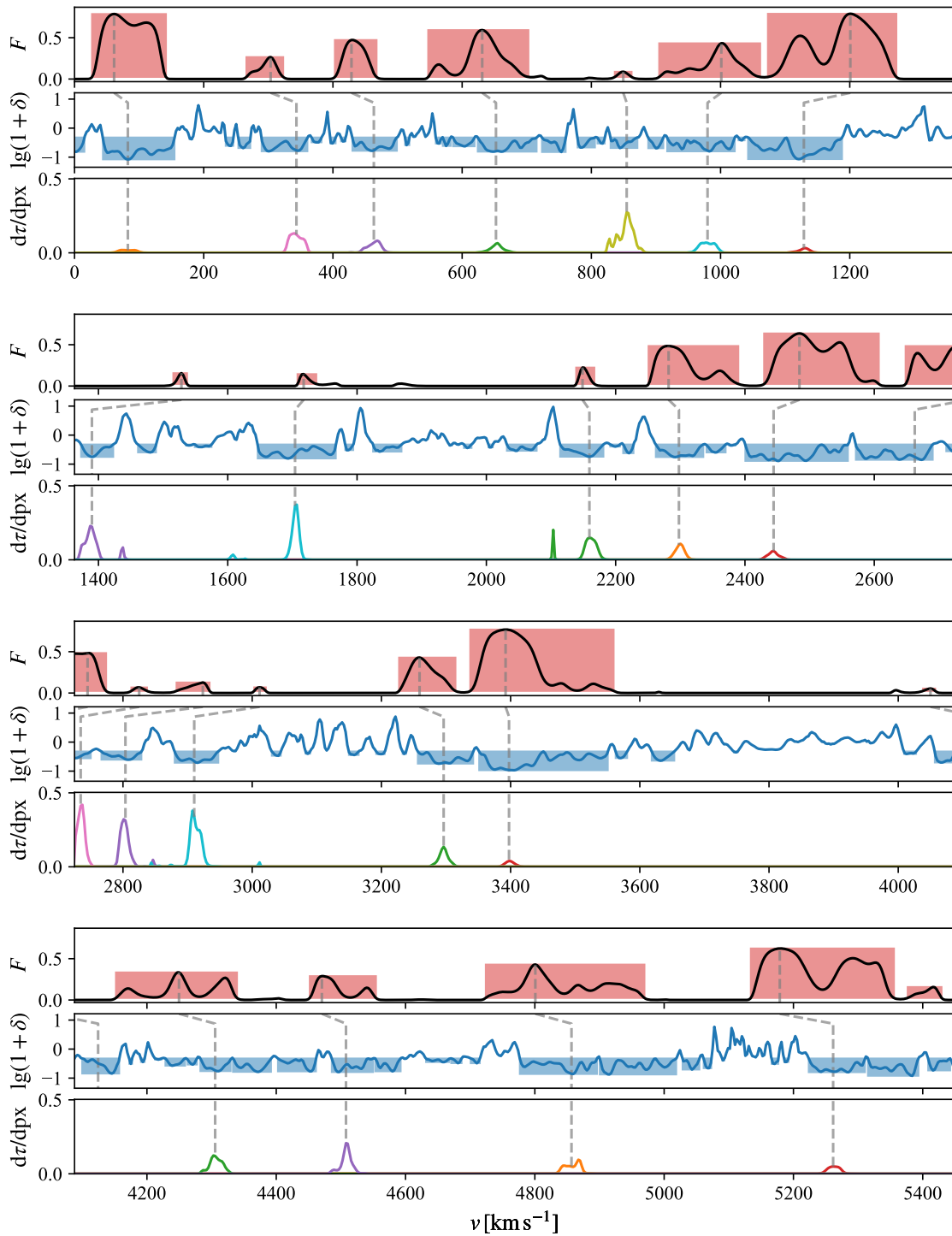


Figure 5.3. Contribution of each real-space pixel to the optical depth at the spike peaks for the *patchy* reionization model at $z = 5$. The plot shows the complete LOS of Fig. 4.4. Each row shows the original (i.e. unscaled) transmitted flux in the upper panel (solid, black lines) with the detected Ly α transmission spikes (red-shaded areas), the gas density contrast (solid, blue lines) in the middle panel, where \lg denotes \log_{10} , with the underdense regions (blue-shaded areas), and the contribution of each real-space pixel to the optical depth at the spike peaks in the bottom panel. Again, the individual colors were randomly chosen to allow distinguishing the different curves. The gray, dashed lines indicate the underdensity and real-space pixel a spike was connected to. The major contribution to the optical depth results from the central regions of the underdensities.

the contribution by individual real-space pixels to the cumulative optical depth (and thus absorption) spans over a larger number of velocity-space pixels due to thermal broadening. The width and height of the Gaussian distribution depends on the temperature (i.e. thermal velocity) in the pixel (see Eq. 2.4.21). However, the main contribution of the pixels is narrowly around their position in velocity space. This supports our choice of relating the spike height to a single real-space pixel only.

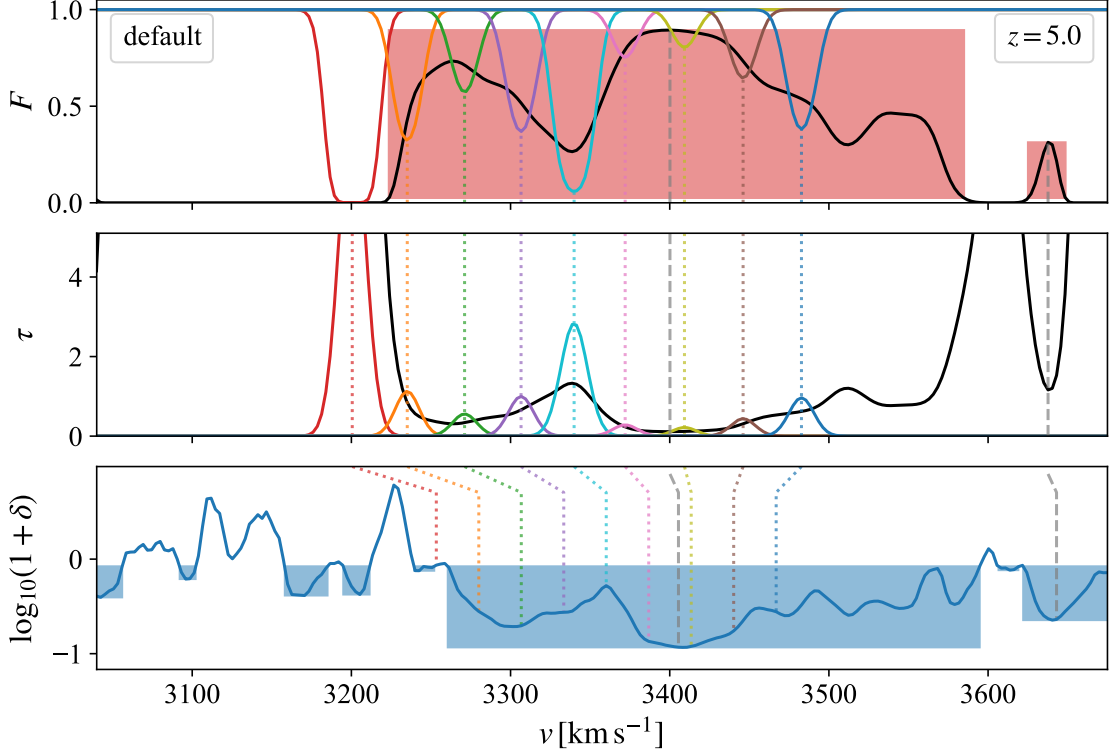


Figure 5.4. Same as Fig. 5.2 except that results are shown for the *default* model here.

This argument is further supported when looking at Figs. 5.3, 5.7, 5.8, and 5.9, which show the contribution of each real-space pixel to the optical depth at the spike peak for the *patchy*, *hot*, *cold*, and *default* model, respectively. The bottom panels of each row plot the contribution of all pixels along the LOS to the cumulative optical depth of the velocity-space pixel at each spike peak (indicated by the gray, dashed lines). It is given by

$$\tau_j = \sum_i^{N_{\text{px}}} \tau_{i,j}, \quad (5.2.1)$$

where $\tau_{i,j}$ denotes the contribution of the real-space pixel with index i to the optical depth in the velocity-space pixel with index j and N_{px} the number of pixels along the respective LOS. All plots support the argument that the strongest contribution results from the connected real-space pixel and its closely surrounding neighbors. It is clearly visible how surrounding pixels also contribute to smaller extents. The contribution by ambient pixels decreases away from the void center. Consequently, relating the spike height to the gas properties of a specific pixel predominantly measures the gas properties around the center of the underdensity. Pixels towards the underdensity edges also contribute in some cases,

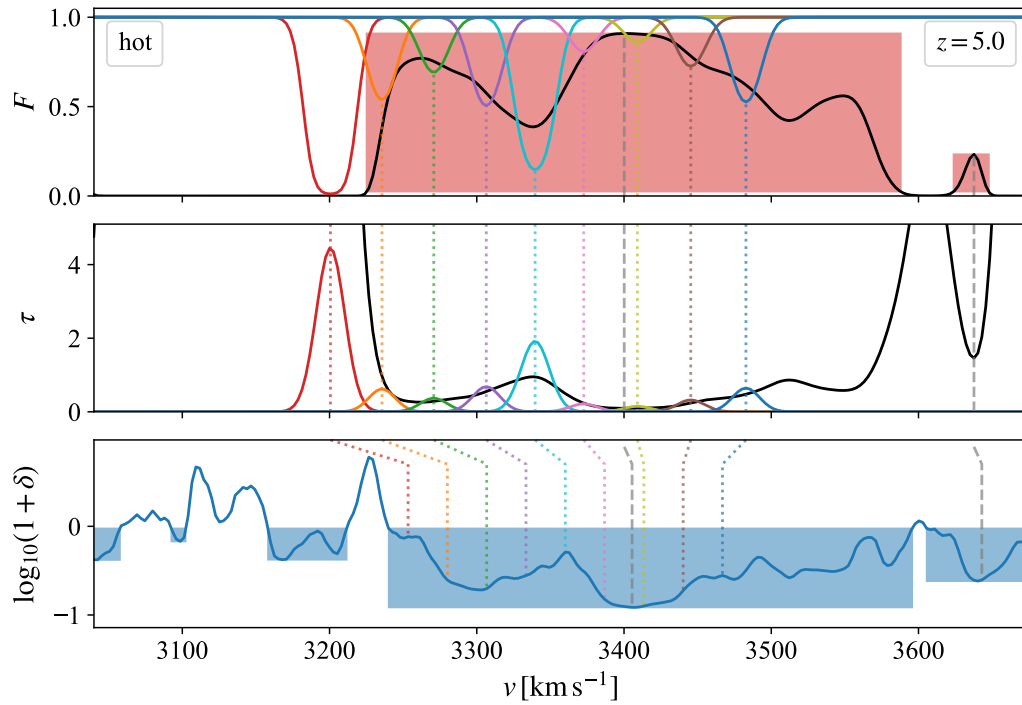


Figure 5.5. Same as Fig. 5.2 except that results are shown for the *hot* model here. As a result of the higher IGM temperature, the contribution to the optical depth of individual pixels is broader and flatter.

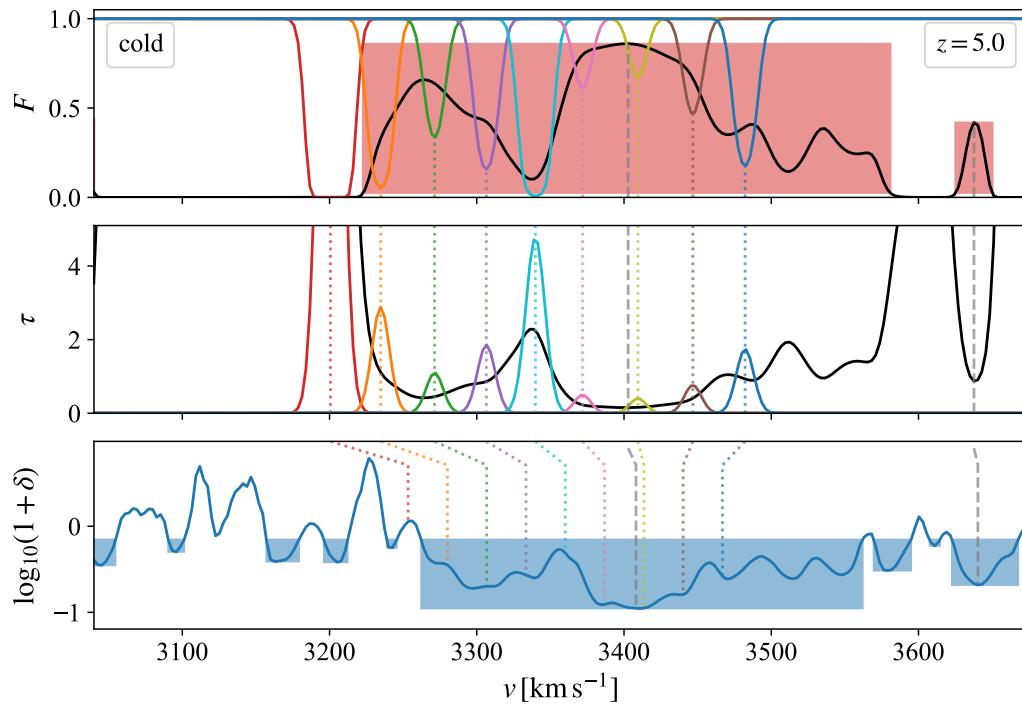


Figure 5.6. Same as Fig. 5.2 except that results are shown for the *cold* model here. The lower IGM temperatures result in a more intensive but narrower contribution of each pixel to the optical depth.

especially when the detected area is narrow. However, looking at the *default* and *hot* IGM model (Figs. 5.9 and 5.7, respectively) it stands out that in rare cases some contribution results from pixels in very dense areas far from the actual spike peak (i.e. walls, see e.g. at $v \approx (1400, 1700, 2180, 3650) \text{ km s}^{-1}$). In contrast, this effect can barely be observed in the *cold* model.

Comparing Figs. 5.5 and 5.6, i.e. the *hot* and *cold* IGM model, reveals the effect of gas temperature (i.e. thermal broadening) on the contribution to the optical depth and, thereby, to the shape of transmission spikes: the *cold* model shows very narrow distributions with higher intensities, whereas the *hot* model reveals weaker and broader contributions. Consequently, the spikes in the *cold* model show more details, which partly reflect the underlying density field – a result of weaker thermal broadening due to a lower HI fraction and IGM temperature. This reflects results from Gaikwad et al. (2020), who found that fitting spikes in models with a cold IGM requires more components. This results in a disconnection of spikes: while transmission in certain areas gets detected as a single spike in the *hot* model, it gets split into separate spikes in the *cold* model (e.g. at $v \approx (900, 2650, 2800, 4450, 4600) \text{ km s}^{-1}$). This supports the effect previously discussed in Sect. 5.1 that the spike number density decreases with IGM temperature. Another effect that can be directly observed is the pressure smoothing of the density field. This becomes especially visible at $v \approx (180 - 300, 3800 - 4000, 5100 - 5200) \text{ km s}^{-1}$: the density field in the *hot* model is much flatter and shows less variability than the *cold* model. This is observable throughout the complete LOS.

Investigating the contribution of individual pixels to absorption shows that transmission spikes probe the central regions of cosmic voids. Void walls also occasionally contribute, dependent on the IGM temperature. Hence, Ly α transmission spikes enable studying the central regions of cosmic voids and allow constraints about their gaseous content. Additionally, the IGM temperature affects the spike shapes. Since thermal broadening governs the contribution of the pixels and depends on the gas temperature, lower (higher) temperatures result in narrower (broader) contributions to the optical depth. As a result, spike details get smoothed with increasing IGM temperature. Consequently, this procedure illustrates that Ly α transmission spikes allow measuring gas properties of the central regions of cosmic voids. They could even be the only observable able to directly measure their gaseous contents.

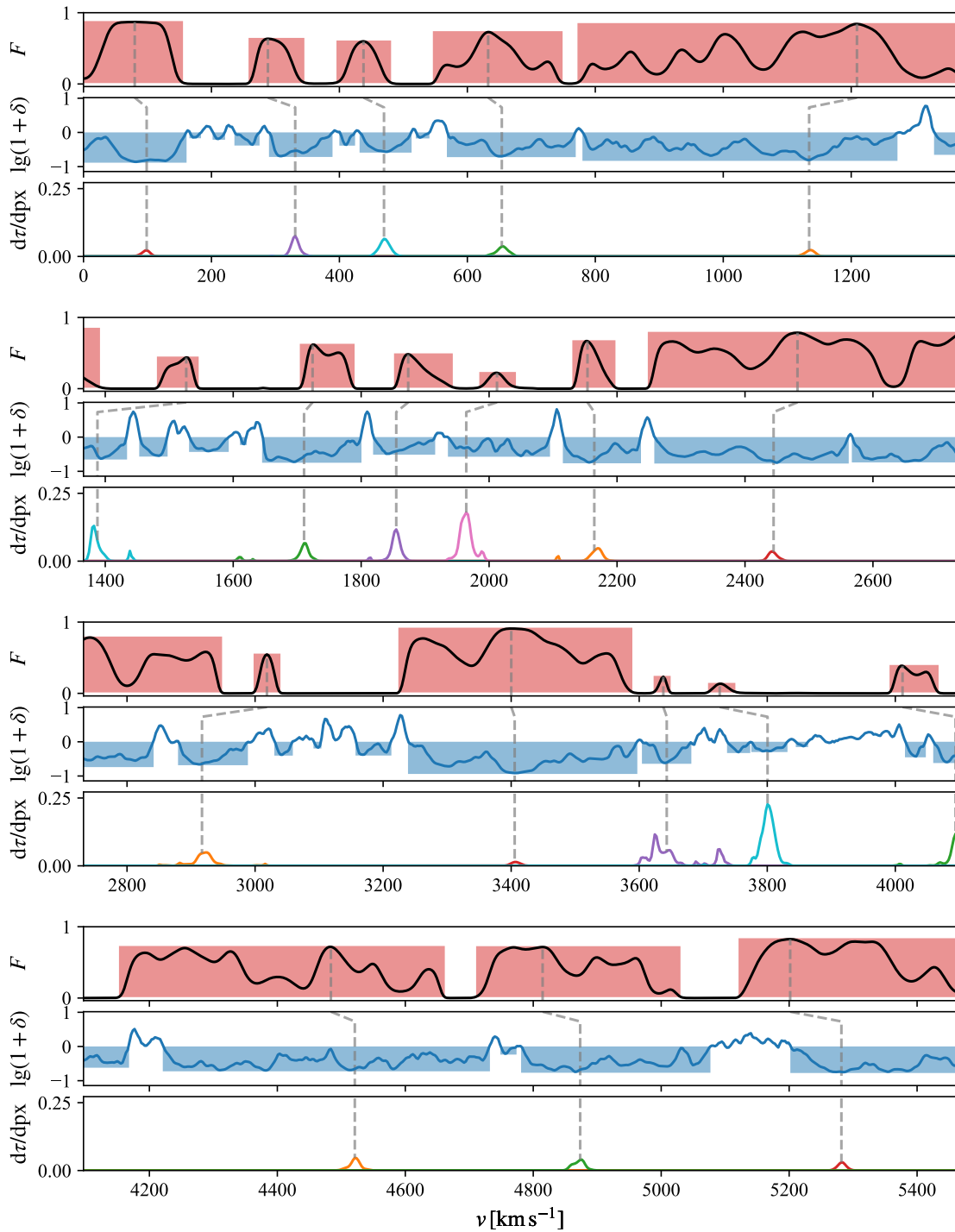


Figure 5.7. Same as Fig. 5.3 except that results are shown for the *hot* model here. The major contribution to the optical depth at the spike peaks results from the connected real-space pixels. Due to the higher IGM temperature, the number of pixels around the center of the underdensities contributing to the optical depth increases. In rare cases, high-density regions in the void edges also contribute.

5.2. Contribution of individual pixels to absorption in underdensities

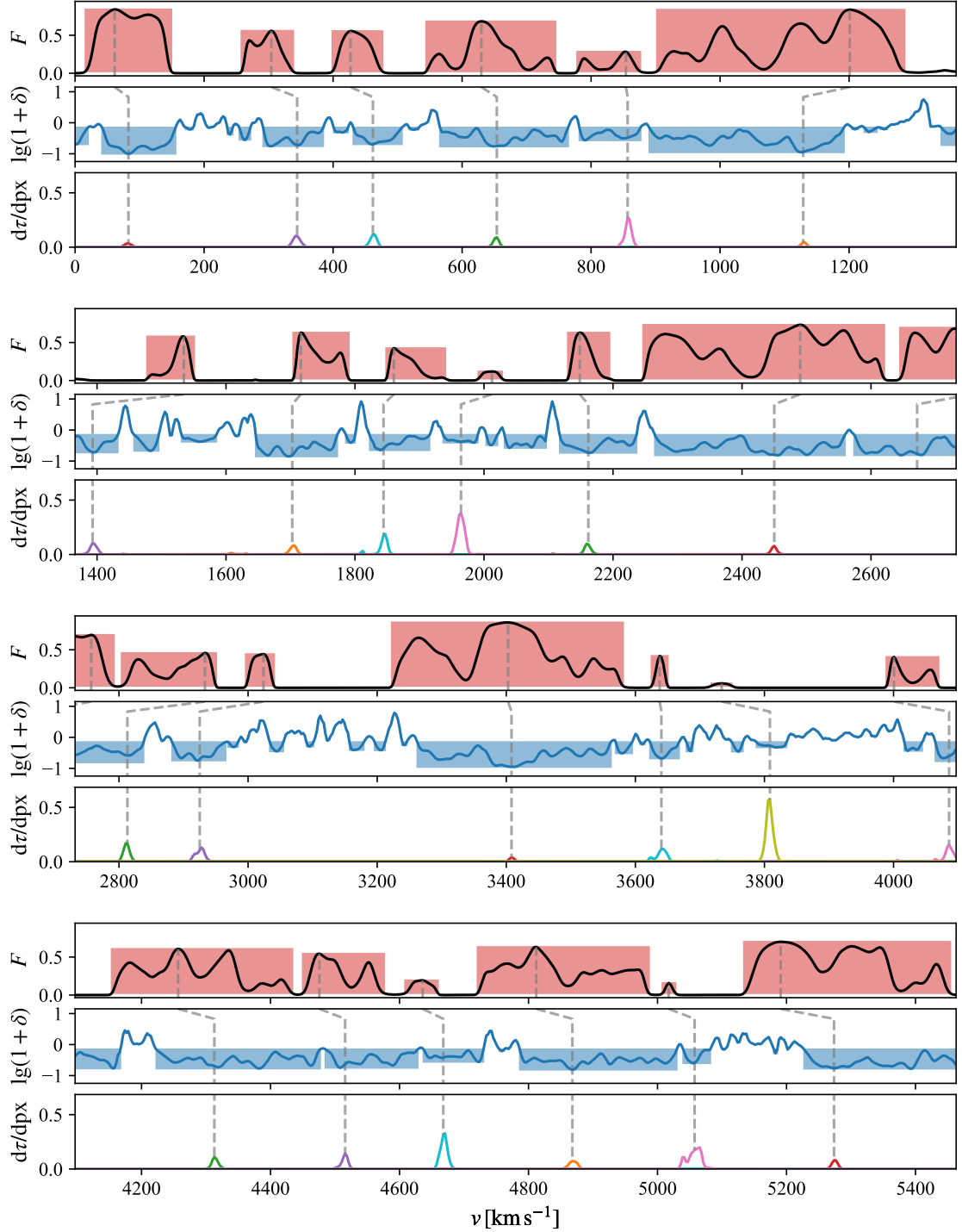


Figure 5.8. Same as Fig. 5.3 except that results are shown for the *cold* model here. The contribution to the optical depth only results from very close neighbors of the central pixel in the underdensities.

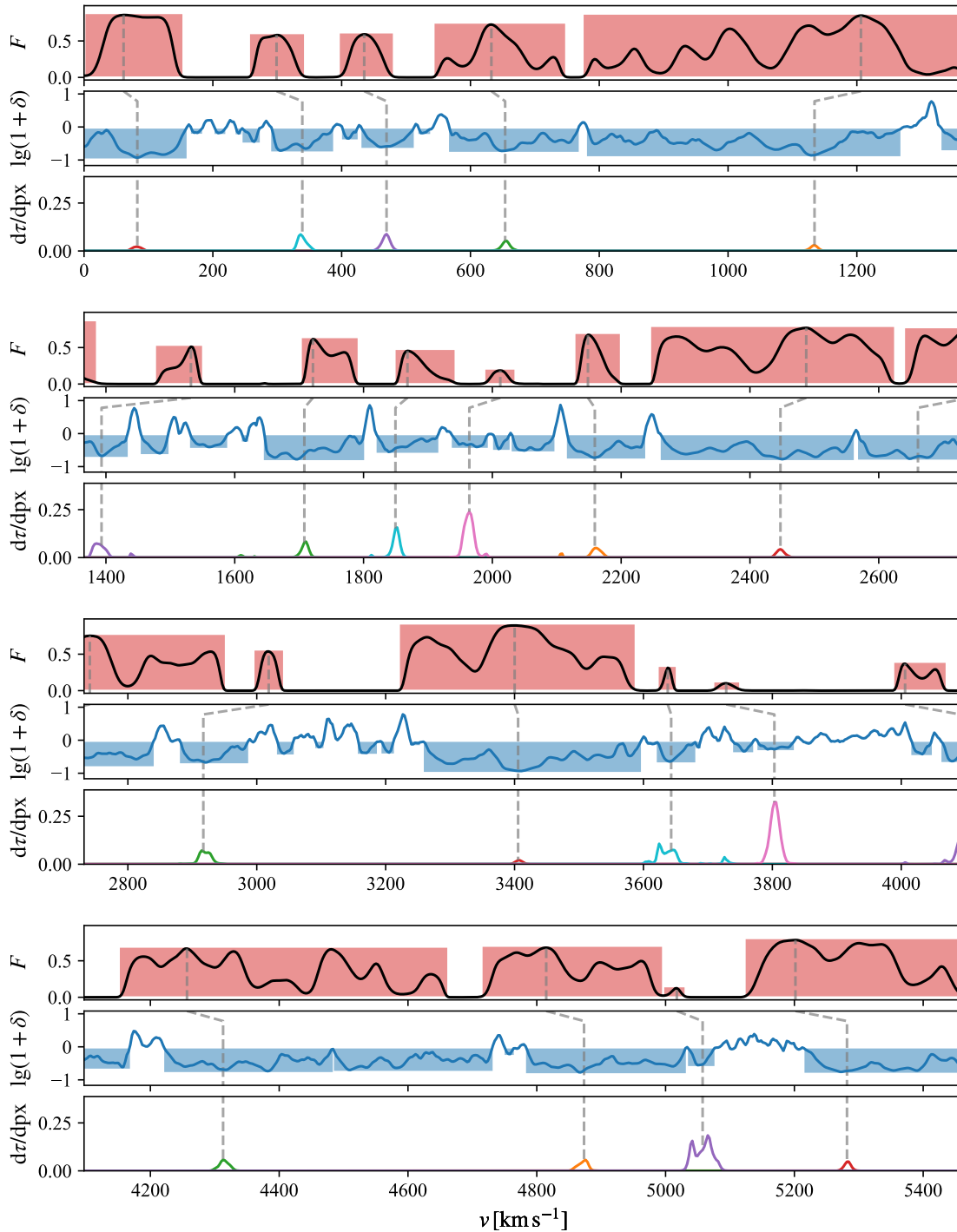


Figure 5.9. Same as Fig. 5.3 except that results are shown for the *default* model here. The major contribution to the optical depth at the spike peaks result from the respective real-space pixels and close neighbors. In very rare cases, high-density regions in walls also show a small contribution.

5.3 Properties of transmission spikes and underdense regions

Figure 4.4 shows only one random LOS through the simulation box of the *patchy* reionization run, but it nevertheless reveals some information about the underdense regions in the IGM that produce the spikes. To begin with, all spikes (red-shaded rectangles) appearing in the spectrum are produced by an underdensity. This is indicated by the gray, dashed lines in the upper and middle panel that show which spike resulted from which underdensity (blue-shaded areas) along the density field. Not all underdense regions, though, transmit the background emission and, hence, produce spikes. Furthermore, one underdense region can produce several separate transmission spikes, while a unique assignment of spikes is possible. The bottom panel reveals that the temperature in underdense regions varies significantly and seems not to correlate strongly with δ . In cold regions, e.g. at $v \approx (1500 - 2100) \text{ km s}^{-1}$, there is a visible correlation between temperature and density, whereas in hot, just recently reionized regions, here visible at $v \approx (2300 - 2800) \text{ km s}^{-1}$, there is almost none.

This argument is also supported by Figs. 5.10 and 5.11, which plot the density contrast, gas temperature, and HI fraction against the spike width w_s and height h_s for the three redshift bins $6.0 \leq z_1 < 6.5$, $5.5 \leq z_2 < 6.0$ and $5.0 \leq z_3 < 5.5$. The solid and dashed lines indicate the 95th and 68th percentile of the distributions, respectively. Here, Fig. 5.10 shows the results of the FWHM method described by [Garaldi et al. \(2019\)](#), whereas 5.11 deploys our adaptive threshold procedure. Generally, the different methods do not show bigger discrepancies in the results. To begin with, all panels suggest that both the spike width and height decrease with redshift. The bottom middle panels reveal that greater spikes tend to appear at higher IGM temperatures. Hence, the spike height correlates with the gas temperature in voids. Moreover, both the density contrast δ (top left panel) and the HI fraction x_{HI} (top right panel) reveal a weak, redshift-dependent negative correlation to w_s . On the contrary, h_s shows a clear, negative relation to δ and x_{HI} (bottom left and right panel, respectively). This is also reflected by Figs. B.1-B.6 in the appendices, which show the results for the remaining models. This indicates that denser regions as well as regions with higher HI fractions cause more absorption and, hence, smaller, narrower, and fewer transmission spikes.

The IGM temperature seems to have an effect on the appearance of spikes. At $v \approx (1400 - 2200) \text{ km s}^{-1}$ (see Fig. 4.4) the temperature fluctuates significantly. Throughout that region, only two small spikes appear that originate from areas with high temperatures above 10^4 K , one of which disappears under the selected detection criteria. At $v \approx (2300 - 2900) \text{ km s}^{-1}$, the temperature is continuously above 10^4 K , which produces a larger number of spikes to appear along the LOS in this range. In the *hot*, *cold*, and *default* model these spikes appear more uniformly distributed (see Figs. 5.7, 5.8, and 5.9 respectively). Thus, the *patchy* model shows a clustering of spikes in hot areas that have been ionized late in the reionization process.

Looking at individual LOSs combined with statistically investigating the relation of spike shapes (width and height) yields some information about the connection of spikes to cosmic voids. While all spikes result from voids, not all voids cause transmission spikes. Generally, the spike width and height both increase with decreasing redshift. Both quantities show different relations to the IGM properties. The spike height grows

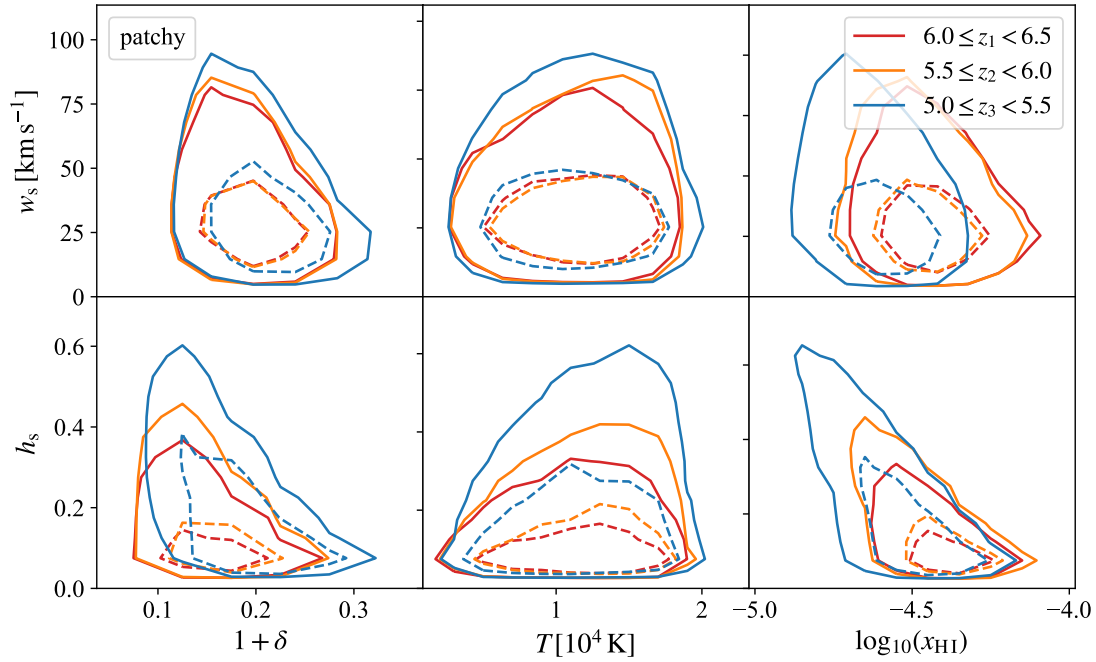


Figure 5.10. Distribution of spike widths and heights and their associated gas properties gas density contrast (left column), temperature (middle column) and HI fraction x_{HI} (right column) in the top and bottom row, respectively, for the three different redshift bins $6.0 \leq z_1 < 6.5$, $5.5 \leq z_2 < 6.0$, and $5.0 \leq z_3 < 5.5$ of the *patchy* reionization model. Here, w_s is measured at FWHM. The solid and dashed lines indicate the 95th and 68th percentile of the distributions, respectively. Here, w_s shows a weak, negative correlation to δ and x_{HI} , whereas h_s reveals a strong, negative correlation to both quantities. Moreover, h_s increases with IGM temperature.

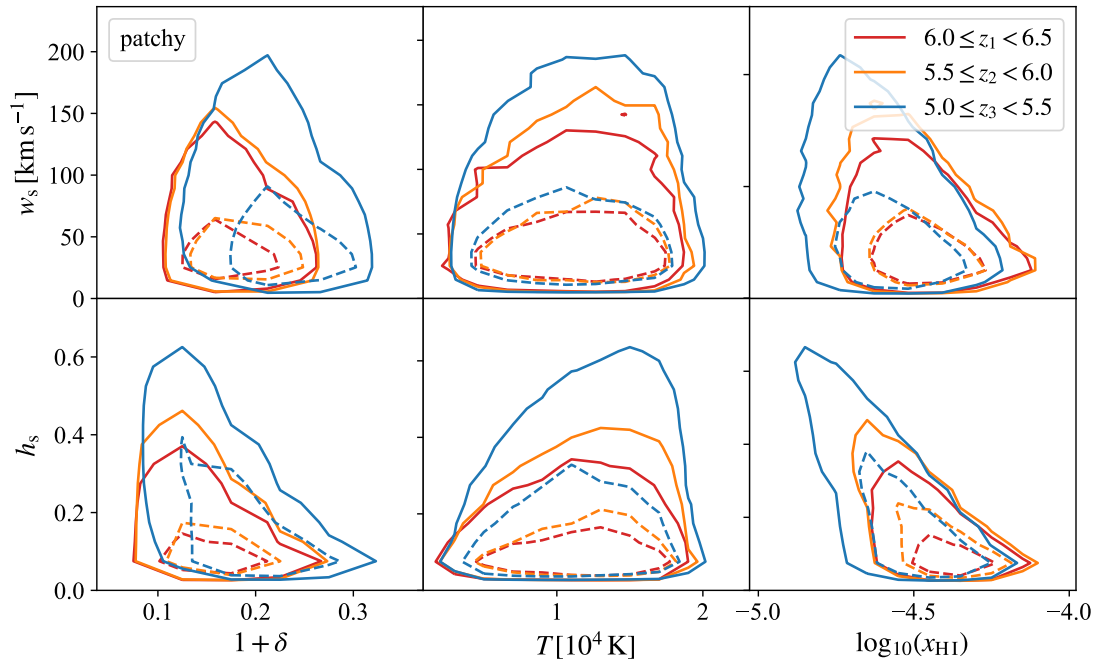


Figure 5.11. Same as Fig. 5.10 except that results are shown for w_s measured at a fixed threshold $F = 0.025$ here. The correlations remain as seen in Fig. 5.10.

with the IGM temperature in voids. Less dense areas and such with a higher degree of ionization produce wider spikes, where the correlation is weak. The spike height, on the other hand, strongly correlates with the gas density and HI fraction. Hence, less dense and highly ionized voids produce greater spikes.

5.4 Relation of spike and underdensity widths

Figure 5.12 shows the distribution of spike widths and their related underdensity extents of the *patchy* model for three different redshift bins $6.0 \leq z_1 < 6.5$, $5.5 \leq z_2 < 6.0$ and $5.0 \leq z_3 < 5.5$. The left and right column depict the results using the FWHM method from [Garaldi et al. \(2019\)](#) and our method, where the spike width is measured at a fixed flux and the value for measuring the underdensity width is the redshift-dependent 95th percentile of the density contrast δ at the spike edges, respectively. As pointed out in the previous section, underdense areas as found by the demonstrated procedure can cause multiple separated spikes to appear in the spectrum. We therefore define the spike width related to an underdensity here to be the sum of the widths of all detected spikes it produced.

The left column of Fig. 5.12 shows that measuring spike width and underdensity extent along the LOS at FWHM reveals a positive correlation with significant scatter between the two – similar to that found by [Garaldi et al. \(2019\)](#). This relation is redshift dependent and gets weaker with increasing redshift. It also stands out that spikes are generally narrower than the spike-producing underdensity.

This significantly improves when measuring with our new method using a fixed threshold for spike and an adaptive threshold for underdensity widths. Again, the spike width is the cumulative width of all spikes originating from the respective underdensity. Whereas the FWHM method shows a weak correlation that only improves with decreasing redshift, our adaptive method reveals an almost 1-to-1 correlation between spike and underdensity widths along the LOS throughout all investigated redshift ranges. Furthermore, the left bottom panel of Fig. 5.12 shows a widely spread void size distribution at all redshifts. Using the threshold method, though, always measures a majority with a width of $w_u \approx 50 \text{ km s}^{-1}$. Both methods, however, show a cutoff at small void scales (see e.g. [Sheth & van de Weygaert 2004](#)).

In contrast to [Garaldi et al. \(2019\)](#), our adaptive, redshift-dependent method reveals that spike widths correlate well with the size of underdense regions along the LOS in all investigated redshift bins. The slope of the relation is ~ 1 . Hence, Ly α transmission spikes are a very suitable tool to study individual cosmic voids and possibly infer the void size distribution.

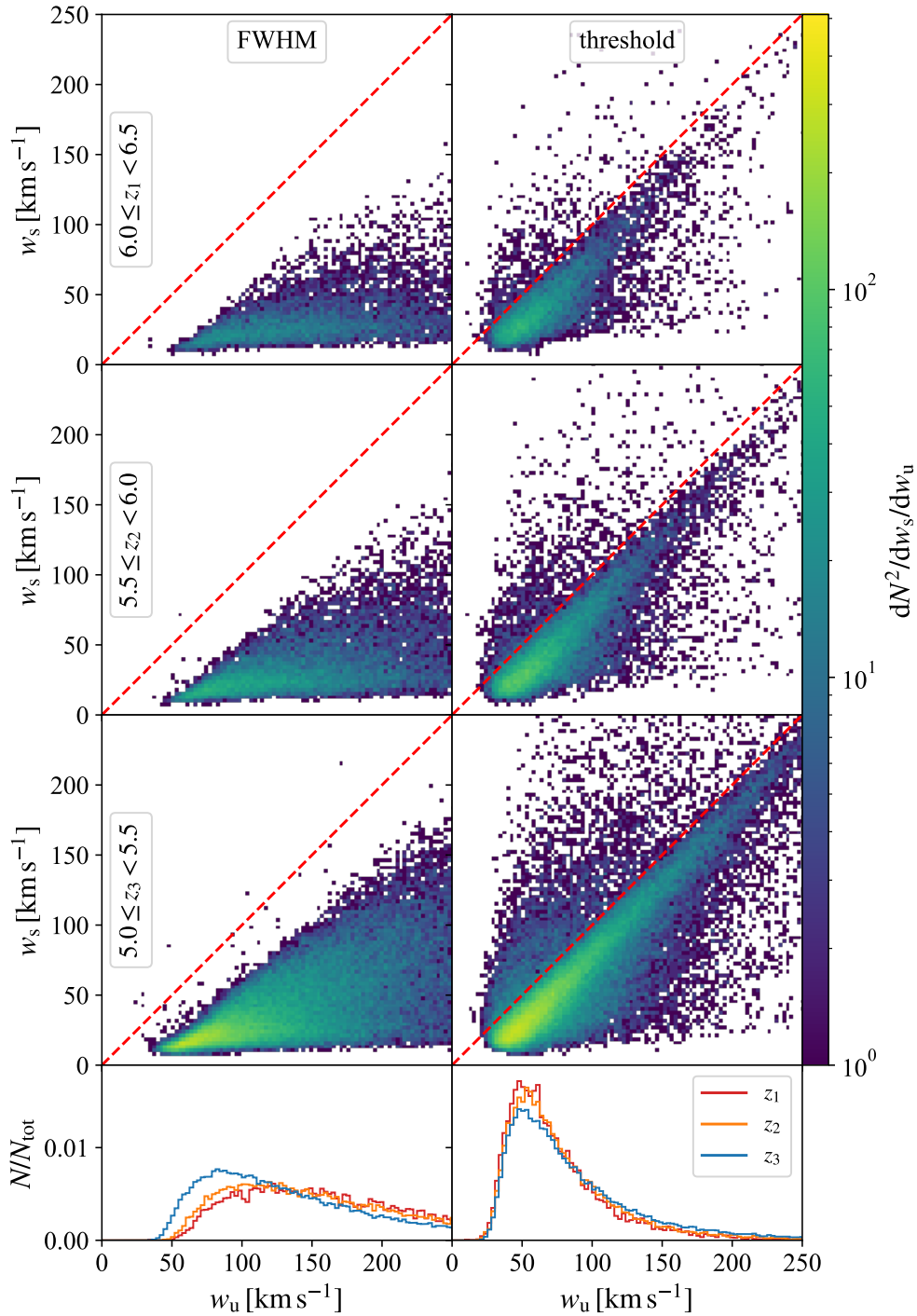


Figure 5.12. Distribution of underdensity widths w_u and transmission spike widths w_s (sum of the widths of all spikes originating from the respective underdensity) along all 5 000 LOSs for the three different redshift bins $6.0 \leq z_1 < 6.5$, $5.5 \leq z_2 < 6.0$, and $5.0 \leq z_3 < 5.5$ for the *patchy* reionization model (three upper rows). The dashed, red lines plot a linear function with slope 1. The left column shows the results for measuring spike and underdensity widths at FWHM. The right column depicts the results of our new method: a fixed and a redshift-dependent, adaptive threshold for measuring spike and underdensity widths, respectively. The bottom row shows the normalized distribution of underdensity widths for each of the three redshift bins. While the FWHM method reveals a weak relation between spike and void widths that decreases with redshift (Garaldi et al. 2019), our method shows a strong linear correlation with slope ~ 1 throughout.

5.5 Comparing patchy and homogeneous UVB models

In contrast to homogeneous UVB models, where the H I fraction increases spatially homogeneously, a patchy UVB causes some regions to ionize early when others are still entirely neutral. A result of this is that the IGM temperature also varies in these regions. By comparing these two approaches to modeling the cosmic UVB, we want to understand how the spatial distribution of ionized and neutral regions and different times of reionization affect Ly α transmission spikes.

To begin with, if the spectra are unscaled, the *homogeneous* model does not allow any transmission before $z \simeq 4.8$, which is outside the redshift range investigated here (see Fig. 5.1a). Even though reionization is supposed to be complete at $z = 5.2$ in both models, no spikes can be observed throughout the investigated redshifts. If the spectra of the *homogeneous* run are scaled to the mean transmission of the *patchy* model, though, the number density of spikes shows a similar trend (see Fig. 5.1b). However, at $z \approx 5.9$ the *homogeneous* model's spike density begins to drop faster.

A cutout of a random LOS at $z = 5$ for both models is plotted in Fig. 5.13. Here, the effective optical depths and, thus, mean transmission of the *homogeneous* model is scaled to that of the *patchy* run. The flux, depicted in the top panel, reveals that transmission appears in the same regions in both models. Spike shapes are very similar, although the homogeneous models shows smaller spikes in regions with high transmission and, vice versa, greater spikes in regions with low transmission. The density field, plotted in the second panel, also shows an almost identical profile throughout the LOS with only very small deviations, which do not show any systematic differences. This can also be observed for the H I fraction in the third panel. However, the gas temperature in the bottom panel reveals some disparities. To begin with, the mean temperature along the LOS is lower in the *homogeneous* model. The profile almost mimics that of the density field. This is different for the *patchy* model, where the gas temperature only shows similar trends in very high or low density regions. In general, it shows stronger fluctuations in these areas, where greater regions with a constantly high temperature appear. In high-temperature regions, H I is lower (i.e. the ionization fraction is greater). This reflects hot regions in the IGM that have been lately reionized and heated.

The relation between spike shapes and the IGM properties for the redshift range $5.5 \leq z_2 < 6.0$ is shown in Fig. 5.14. First of all, the bottom row shows that a patchy UVB model produces higher spikes than a homogeneous one. This is because the *patchy* model exhibits areas populated with ionizing sources that produce high photoionization rates, which make the H I fraction and temperature drop and increase enormously, respectively, (see also Fig. 5.13 at $v \approx (1000 - 1300) \text{ km s}^{-1}$ and $(2300 - 2700) \text{ km s}^{-1}$) and hence allow a lot more transmission than a homogeneous UVB in these areas. The IGM temperature and H I fraction, plotted in the middle and right columns, respectively, are of the same order of magnitude as previously observed in Fig. 5.13, but show less spread in the *homogeneous* run. Again, the spike width (height) show a weak (strong) negative correlation, respectively, to the density contrast and H I fraction. At this redshift range, though, this cannot be observed in the *homogeneous* model. However, looking at Fig. B.1 in the appendices, which shows the full redshift range $z = 5.0 - 6.4$, the correlation also appears at lower redshifts $5.0 \leq z_3 < 5.5$.

The correlation between spike and underdensity width is depicted in Fig. 5.15. Both

models create equal underdensity and spike widths and also show a constant linear correlation with slope ~ 1 , although there are differences between the two. While the *homogeneous* model produces a relatively sharp distribution, the patchy UVB creates more spread and, thereby, a weaker correlation. Comparing the normalized distribution of the two models reveals that the *patchy* run generates an equivalent dispersal for all three redshift bins, which changes with redshift in the *homogeneous* simulation: the fraction of underdensities with $w_s \approx 50$ decreases with redshift.

Comparing the *patchy* to the *homogeneous* UVB model, it again becomes visible that the latter produces implausible results since it does not allow any transmission of light before and closely after reionization has finished. Only a spatially inhomogeneous UVB can produce highly ionized areas early during cosmic reionization to allow Ly α transmission spikes to appear at redshifts $z > z_r$, i.e. during cosmic reionization. Furthermore, it produces larger spikes resulting from highly ionized areas, whereas a homogeneous UVB causes spikes to appear more smoothly distributed but less intense due to the spatially uniform increase of the HI fraction. Both models, however, equally show a constantly strong linear correlation between spike and void widths with slope ~ 1 throughout all three redshift bins if the spectra of the *homogeneous* model are rescaled. The size distribution of voids associated with spikes, though, varies slightly between the two since the patchy UVB produces wider spikes.

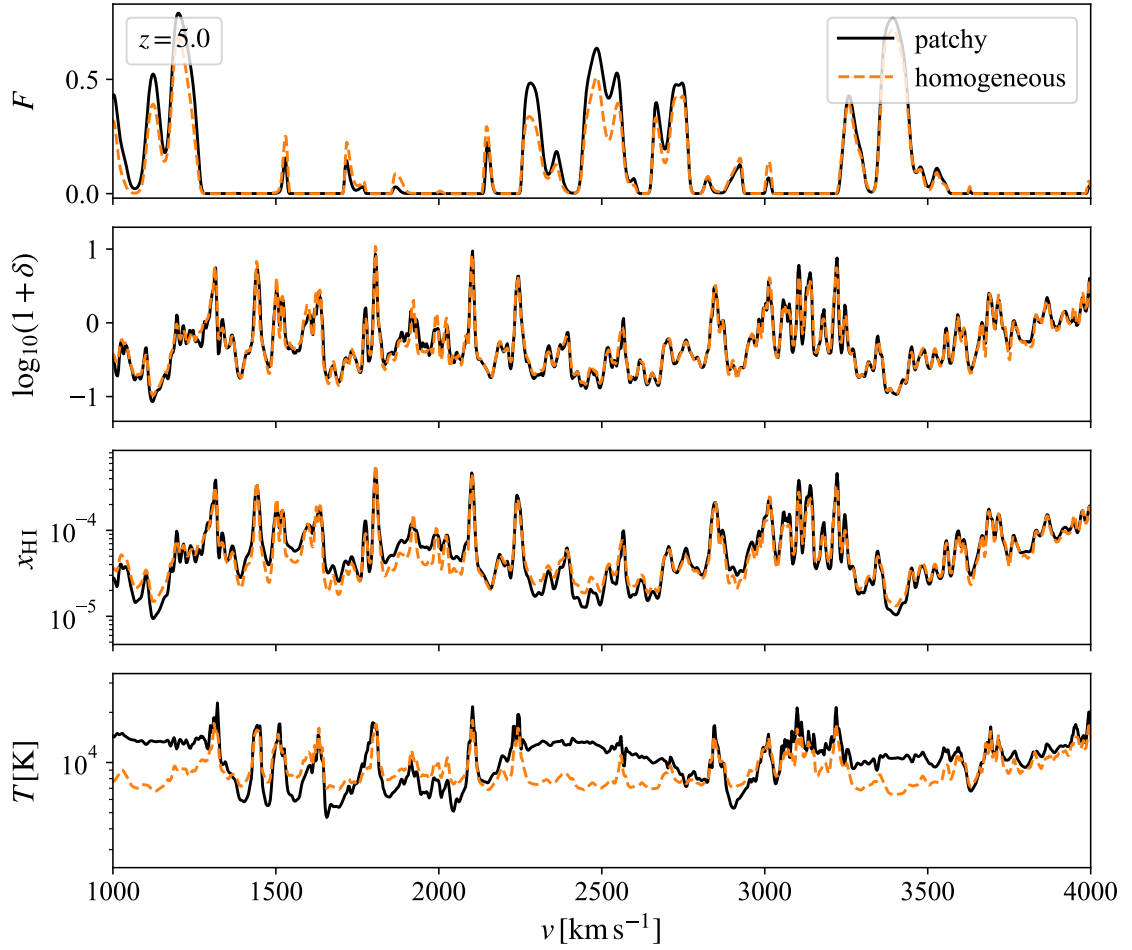


Figure 5.13. Same as Fig. 4.4 except that results are shown for the *patchy* (solid black lines) and *homogeneous* (dashed orange lines) UVB models at $z = 5$ here. The mean transmission (and, hence, HI fraction) of the *homogeneous* model is scaled to that of the *patchy* run. The major difference between the two models is visible in the IGM temperature. Here, the *homogeneous* model shows a temperature profile similar to the density field, whereas the *patchy* model shows large high-temperature regions that have been lately reionized and heated.

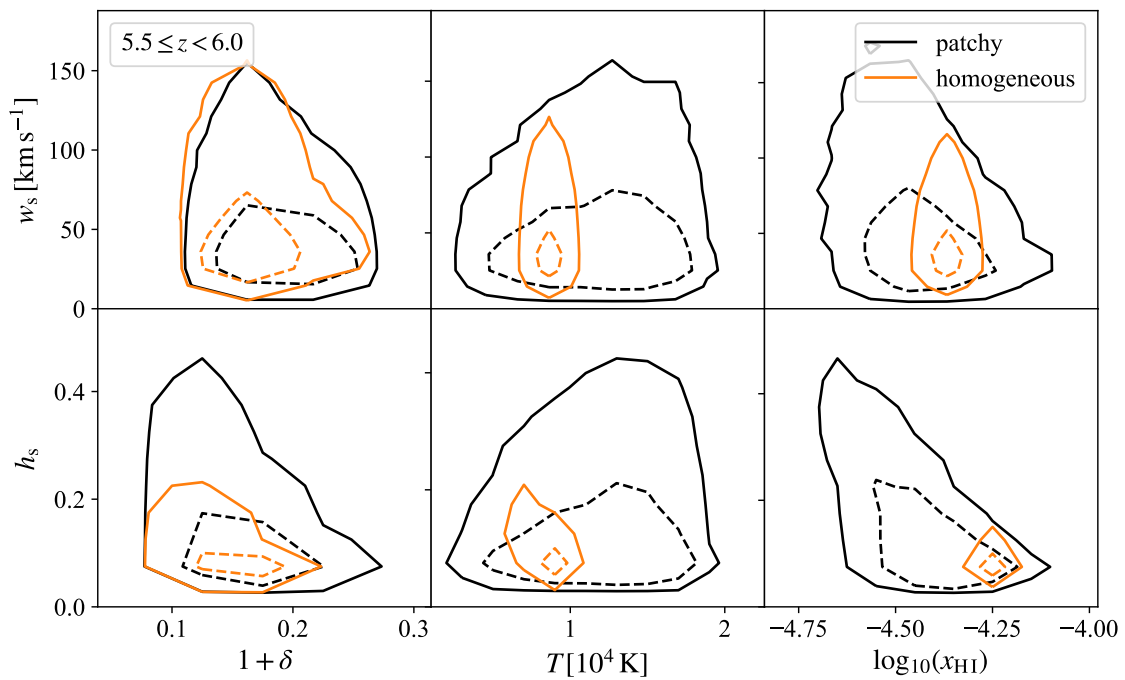


Figure 5.14. Same as Fig. 5.11 except that results are shown for the *patchy* (black lines) and *homogeneous* (orange lines) model at $5.5 \leq z_2 < 6.0$ here. The results for the *homogeneous* model at all three redshift bins are shown in Fig. B.1 in Appendix B, whereas that of the *patchy* model are shown in Fig. 5.11. We previously pointed out that w_s shows a weak, negative correlation to δ and x_{HI} and h_s a strong, negative correlation to both quantities. These are not present in the *homogeneous* model in this redshift range.

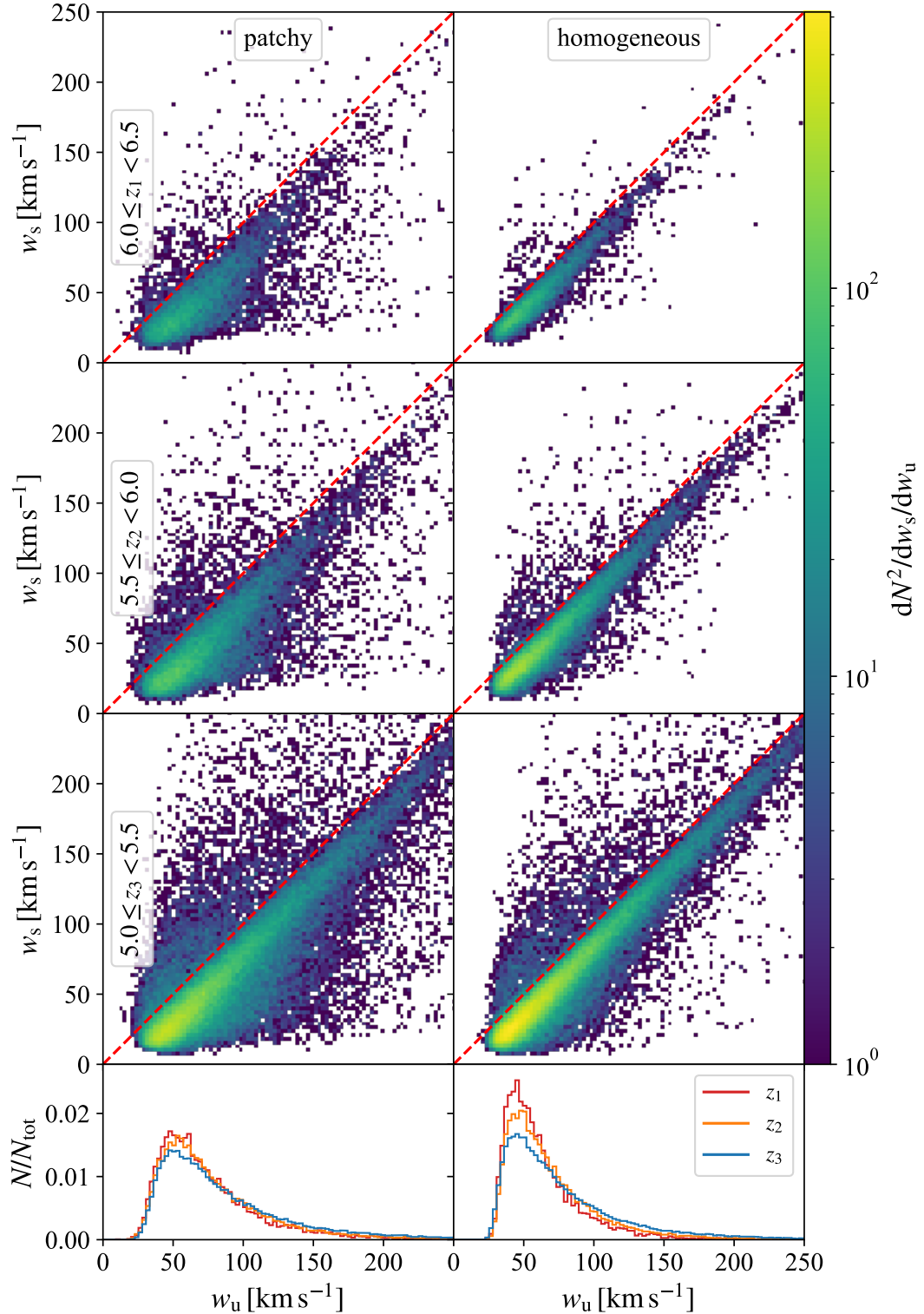


Figure 5.15. Same as the right column of Fig. 5.12 except that results here are shown for the *patchy* (left column) and *homogeneous* model (right column). Both models reveal a relation between spike and void widths with constant slope ~ 1 throughout the investigated redshift range. The patchy model, though, shows more spread.

5.6 Influence of IGM temperature

By investigating models with varying IGM temperatures, we aim to understand how the gas temperature in voids affects the transmission spike shapes. Figure 5.16 shows a comparison of the Ly α spectra along a random LOS at $z = 6$ for the *default*, *hot*, and *cold* IGM reionization models as well as the density contrast and gas temperature. Here, the optical depths and hence HI fraction were scaled to match observed mean transmissions. The Ly α spectra show roughly the same transmission profile, i.e. the spike density is similar, which can also be seen in the top panels of Fig. 5.1. However, there are some differences between the spike shapes. The *cold* IGM model shows more small-scale structure in the spike profiles, whereas for the *default* and *hot* models these details get smoother with increasing IGM temperature. The greater the temperature of the IGM, the more strongly thermal broadening is able to smear out these features (see Sect. 5.2). This matches with results from Gaikwad et al. (2020), who found that fitting transmission spikes in Ly α forest spectra requires fewer components the higher the IGM temperature of the underlying model.

While the second and third panel of Fig. 5.16 show that generally the profile of the density field and HI fraction along the LOS is very similar for the three models, the bottom panel shows larger discrepancies: the difference in IGM temperature is clearly visible as it varies by $\sim 5 \times 10^3$ K between the three models at the investigated redshift. This is confirmed by the middle and right panels of Fig. 5.17, which show the connection between transmission spike properties and gas temperature and HI fraction of the spike-producing, underdense regions at $5.5 \leq z_2 < 6.0$, respectively. Here, the temperature does not show any correlation with the spike width or height in the individual models. However, Fig. 5.10 shows that there is in fact a positive relation of temperature to spike height. Hence, here the results might be biased due to the scaling of the mean transmission. Comparing the three models with each other, though, reveals that the spike height and width is affected by the IGM temperature. The hotter the IGM, the higher and broader the transmission spikes. Again, the weak (strong) negative correlation between spike width (height) and gas density and HI fraction is visible, but does not significantly vary between the models. Furthermore, the gas density and HI fraction in the underdensities causing the transmission spikes is slightly higher and smaller, respectively, for a higher given gas temperature. Hence, the photoheating rate affects the degree of ionization and density distribution.

The spike-underdensity width relation for the three different models is plotted in Fig. 5.18. All of them show a seemingly identically strong linear correlation between the two measures as already seen in Fig. 5.12. However, the normalized distribution of underdensity widths in the bottom panels suggests that in the *cold* model we usually find narrower voids. This is a result of the IGM temperature influencing the spike shapes such that we measure the voids at different densities (see Fig. 4.6).

Comparing the three models with different photoheating rates shows that the IGM temperature influences both the spike width and height. This is because the degree of ionization of the IGM increases with temperature. Furthermore, thermal broadening increasingly smooths the spike details. The relation between spike and void widths is not visibly affected by the IGM temperature, although there are small discrepancies in the void size distribution. This shows that the photoheating rate and, thus, IGM temperature,

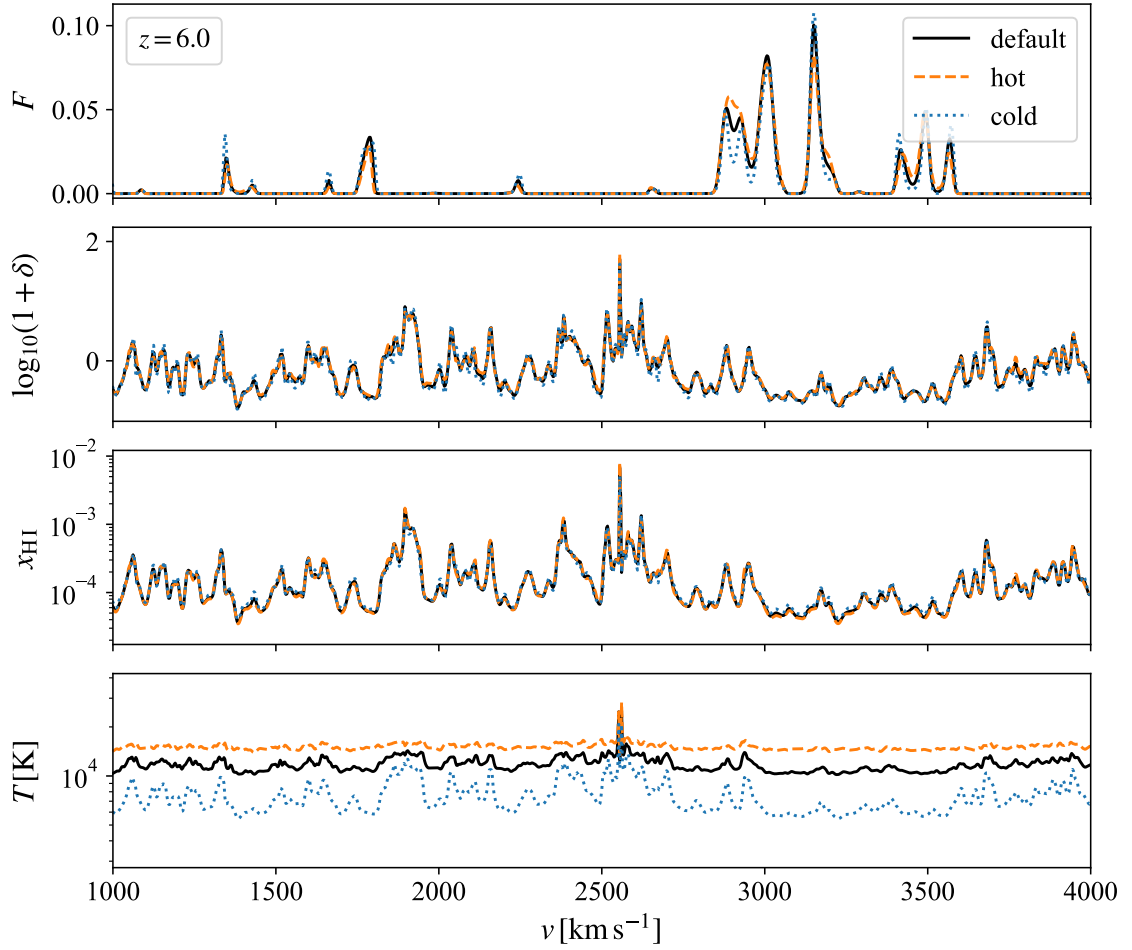


Figure 5.16. Same as Fig. 4.4 except that results are shown for the *default* (solid black lines), *hot* (dashed orange lines), and *cold* (dot-dashed blue lines) IGM models at $z = 5.6$ here. The mean transmission (and, hence, HI fraction) is scaled to that observed by [Bosman et al. \(2018\)](#). While there are only marginal differences for the flux, density and HI fraction between the three models, the temperature shows greater variations. Especially the hot model shows a very flat temperature profile due to pressure smoothing.

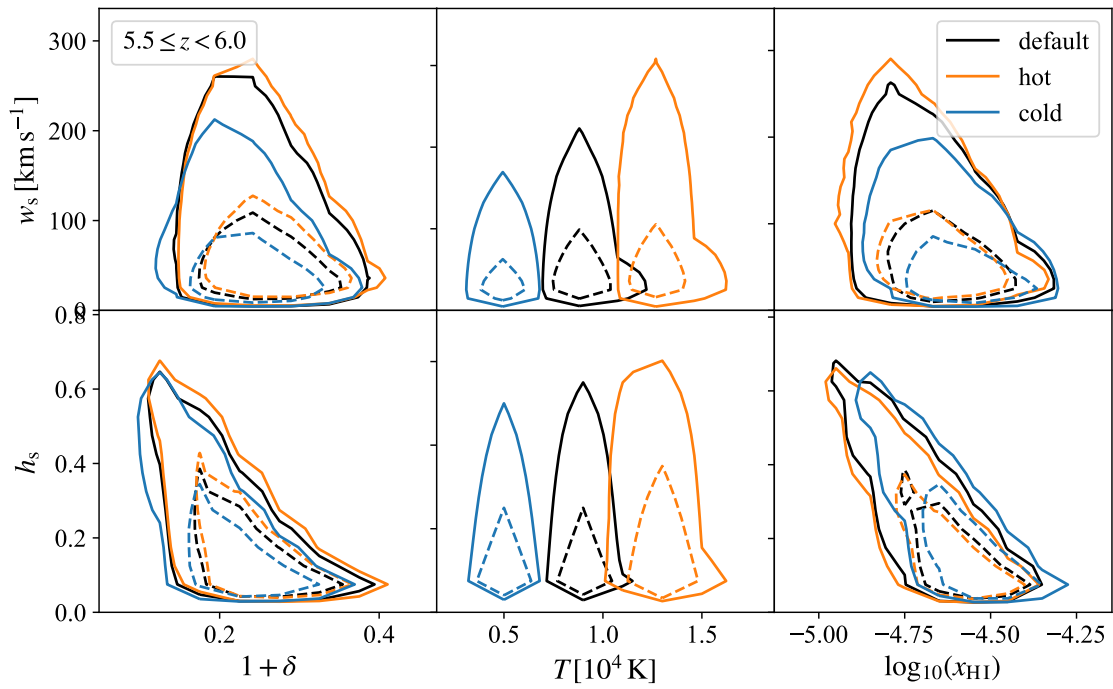


Figure 5.17. Same as Fig. 5.11 except that results are shown for the *default* (black lines), *hot* (orange lines), and *cold* model (blue lines) at $5.5 \leq z_2 < 6.0$ here. The results of each model for all three redshift bins are shown in Figs. B.2, B.3, and B.4, respectively, in Appendix B. All three models still show the same weak (strong) negative correlation between the spike width (height) and δ and x_{HI} . The top row reveals that the spike width increases with IGM temperature.

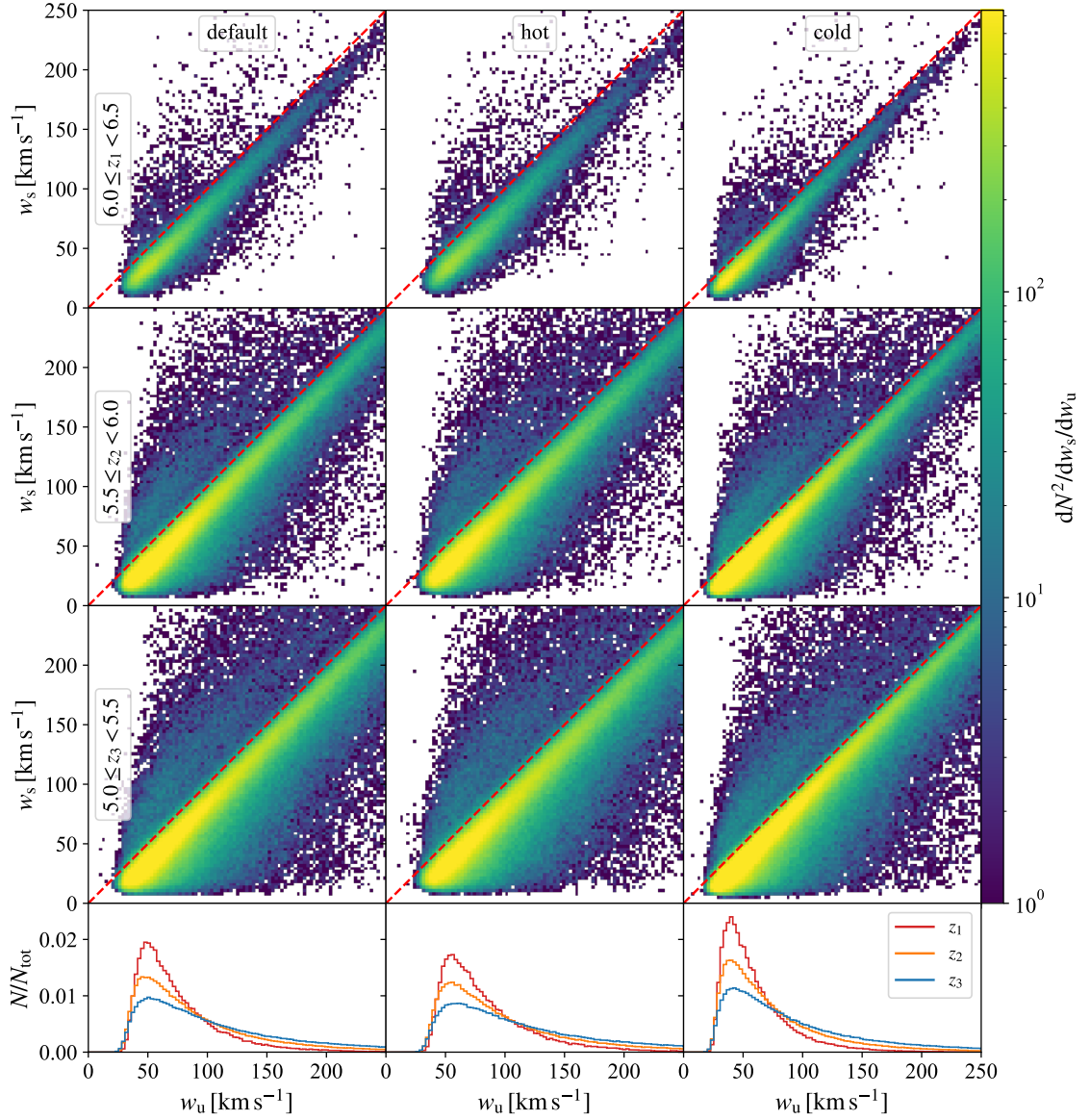


Figure 5.18. Same as Fig. 5.15 except that results are here shown for the *default* (left column), *hot* (middle column), and *cold* model (right column). There are no visible differences for the correlation of spike and void widths between the three models. The void size distribution in the bottom row shows that the void widths increase with IGM temperature.

due to the impact on the spike shapes, affects the densities at which we measure voids with our adaptive method.

5.7 Effect of ionization history and mean transmission on spike properties

The exact period over which reionization took place is still unclear. While the start of the EoR is still very uncertain in terms of redshift, the end of the EoR appeared at $z \approx 6$ as constrained by multiple independent observations (Fan et al. 2006; Schroeder et al. 2013; McGreer et al. 2015). Therefore, we test whether the reionization history has any effect on Ly α transmission spikes and the relation between spike and void widths.

The *early* and *intermediate* reionization models deploy different photoionization rates and hence represent distinct ionization histories in which the reionization process finishes at $z_r = 6.75$ and $z_r = 7.5$, respectively. Figure 5.19 shows three different Ly α spectra at $z = 5$ and their underlying gas properties (density contrast, H I fraction, and temperature in the second, third, and bottom panel, respectively) for the three simulation runs with different reionization redshift $z_r = (6.2, 6.75, 7.5)$. Well after the end of the reionization era, the IGM temperature, x_{HI} profile, and density field are almost identical in all three models. Pressure smoothing does not affect the spike shapes (i.e. spike widths and heights) at scales investigated here. The spike profiles, though, show small-scale discrepancies. Hence, the spike properties we measure do not depend on reionization history in models with a homogeneous UVB. However, since they correlate with x_{HI} , they may well depend on reionization history in a patchy reionization process because the H I fraction is not increasing in a spatially-uniform manner and is hence different to the density profile of the IGM (see Figs. 4.4 and 5.13). We also investigated the distribution of spike and void widths (see Fig. A.1 in Appendix A) as well as the relation of the IGM properties to spike shapes (see Figs. B.2, B.5, and B.6 in Appendix B) here. However, there are only marginal differences between the models. We therefore conclude that the reionization history does not affect our previous results inferred from the spike widths and heights at $z = (5.0 - 6.4)$.

In order to investigate how the mean transmission (i.e. effective optical depth τ_{eff}) affects the relation of observed spike shapes to the underlying IGM properties, we scale the Ly α spectra of the reference model (i.e. *default* run) to match $\tau_{\text{eff}} = (1, 3, 5)$. By doing so, we test if scaling the spectra affects the inferred statistics. Figure 5.20 shows the result of this procedure. As expected, the spectra with lower effective optical depths show more transmission spikes. The spike heights and widths also increase with τ_{eff} . This suggests that lower effective optical depths lead to a better sensitivity towards denser regions with a smaller H I fraction. Figure 5.21 supports the assumption that lower optical depths produce greater and wider spikes. However, the correlations of the spike shapes to the density and H I fraction are still visible. Hence, this procedure shows that the scaling affects the spike statistics. Thus it is important to scale the spectra to observed mean transmissions.

By investigating homogeneous UVB models with different reionization histories, we find that the redshift at which reionization finishes does neither significantly affect Ly α transmission spike shapes, nor the correlations of spike width and height to the IGM prop-

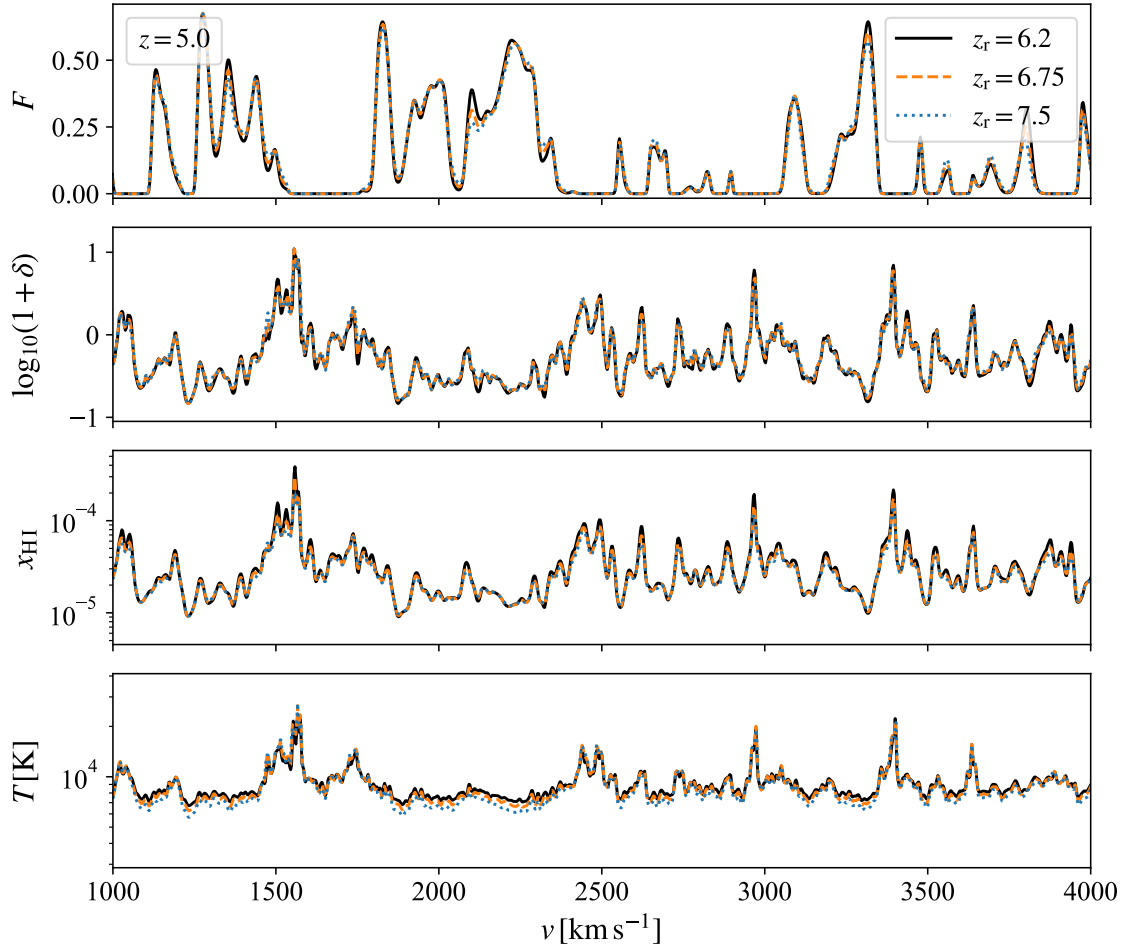


Figure 5.19. Same as Fig. 4.4 except that results are shown for the models with different reionization redshifts $z_r = 6.2$ (*default* model, solid black lines), $z_r = 6.75$ (*intermediate* model, dashed orange lines) and $z_r = 7.5$ (*early* model, dot-dashed blue lines) at $z = 6.2$ here. The mean transmission (and, hence, HI fraction) is scaled to that observed by [Bosman et al. \(2018\)](#). There are only marginal differences between the three models.

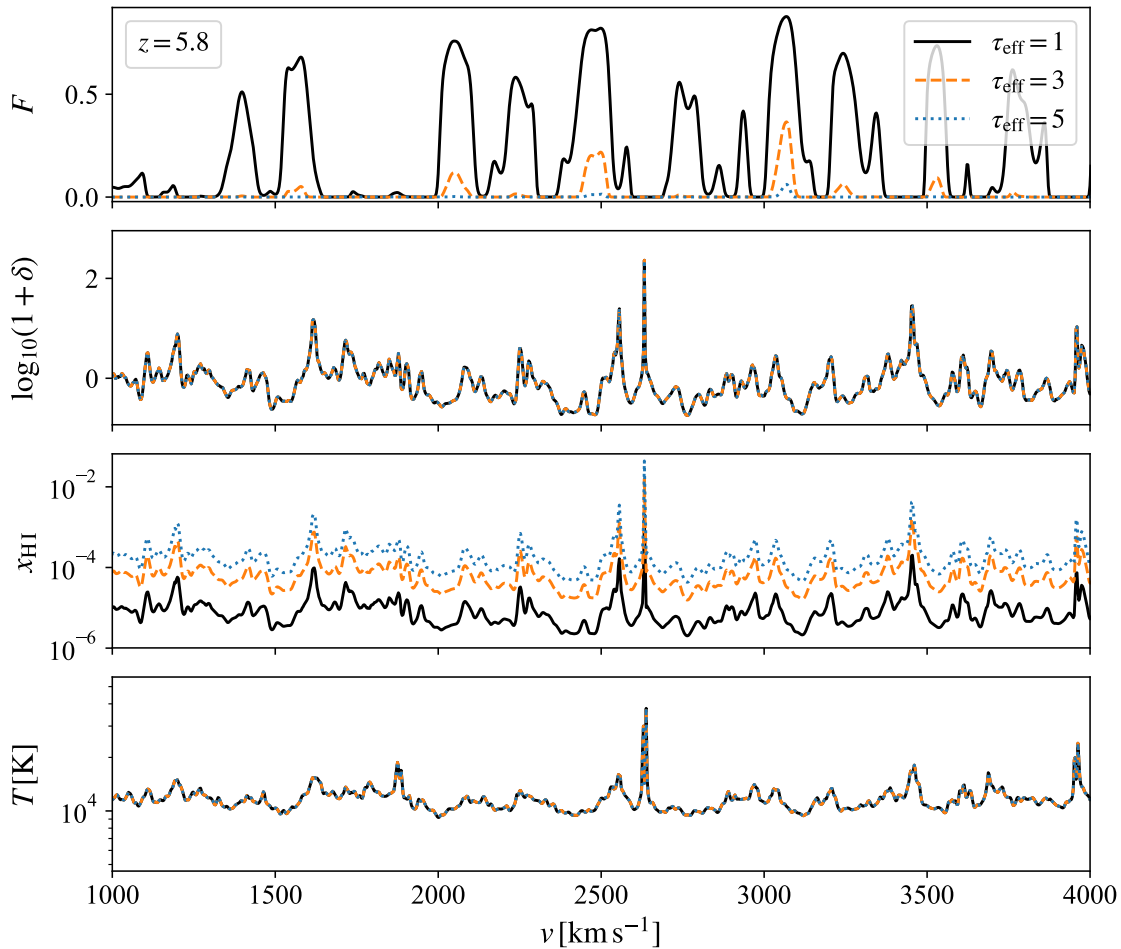


Figure 5.20. Same as Fig. 4.4 except that results are shown for the *default* model scaled to different effective optical depths $\tau_{\text{eff}} = 1$ (black lines), $\tau_{\text{eff}} = 3$ (orange lines), $\tau_{\text{eff}} = 5$ (blue lines). at $z = 5.8$ here. Lower effective optical depths lead to a better sensitivity towards denser regions.

erties. Especially the relation between spike and void widths is indistinguishable between the three scenarios in the investigated redshift range. Moreover, scaling the *default* model to specific mean transmissions lets us conclude that the artificial rescaling of the spectra of models with a homogeneous UVB does influence the spike statistics. Thus, it is required to scale the spectra and the UVB (i.e. photoionization rate) to observed mean transmissions as we did in this work.

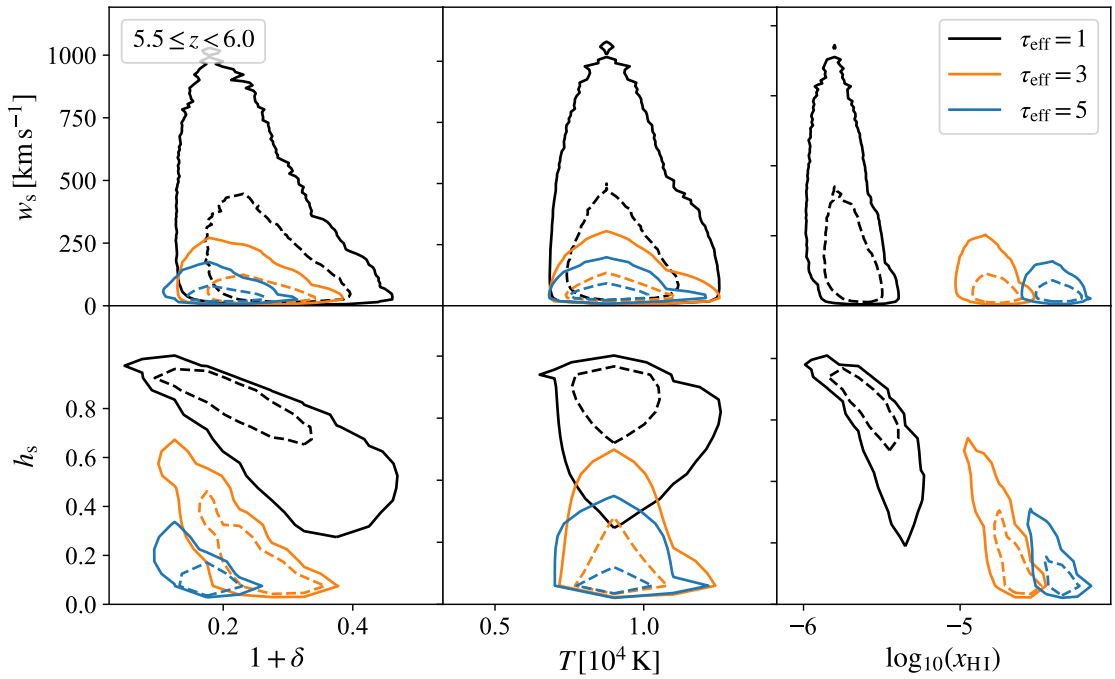


Figure 5.21. Same as Fig. 5.11 except that results are shown for the *default* model scaled to different effective optical depths $\tau_{\text{eff}} = 1$ (black lines), $\tau_{\text{eff}} = 3$ (orange lines), $\tau_{\text{eff}} = 5$ (blue lines) at $5.5 \leq z_2 < 6.0$ here. The results of each model for all three redshift bins are shown in Figs. B.7, B.8, and B.9, respectively, in Appendix B. The correlations between the spike properties and δ and x_{HI} are still present. Thus, spike statistics are unaffected by the rescaling.

5.8 Impact of realistic noise on the results

In Sect. 4.5 we added Poisson and Gaussian noise to the spectra to study the effect of noise as it appears in real spectra on our results. Compared to the analysis of the original, scaled spectra (see Fig. 5.1b), the noisy spectra show the same number density of transmission spikes with $\sim 4 - 6 \times 10^{-6} h^{-1} \text{ cMpc}$ at $z = 5$. It also shows a very similar trend at first. In the *default*, *hot*, and *cold* model, however, the spike density decreases after $z \approx 6.1$ and drops to none immediately at $z \approx 6.4$. In the *homogeneous* model this can already be observed at $z = 6$, although even more drastically. In general, this effect appears at high redshifts since there the noise already exceeds the usual intensity of transmission spikes in the original spectra. Thus, they completely disappear under our detection criteria after the filtering process. In this redshift range, the *patchy* run shows the exact same number density evolution as before as it produces higher spikes than the *homogeneous* model. (For the *homogeneous* model, though, the abrupt drop is also due the next redshift at which data are available being $z = 6.4$.)

The result for a random LOS at $z = 5.4$ of the *patchy* reionization run is shown in Fig. 4.8. This LOS is identical to the one shown in Fig. 4.4. Similarly, the red-shaded rectangles represent the detected spikes (i.e. their width and height) and the blue-shaded regions show the detected underdensities. The black line in the figure's top panel plots the spectrum after noise was added and the red and green lines depict the original and filtered spectra, respectively. Again, the gray, dashed line indicates the underdensity (i.e. spatial pixel) a spike has been connected with. It may be seen that the transmission spikes detected in the original spectrum are still clearly identifiable and get detected at this redshift. This shows that using a Wiener deconvolution reliably reconstructs the original spectrum from the spectrum with noise. In some cases, though, it slightly under- or overestimates the original flux (e.g. at $v \approx (2250, 2400, 2500, 2750, 2900) \text{ km s}^{-1}$). However, these are spikes with a rather low transmission. Hence, this effect only appears to occur if the transmission is low since the flux-to-noise ratio is smaller in these areas.

As the transmission spikes are very close to the original flux, the relation between spike and IGM properties, shown in Fig. 5.23, is also observable as in Sect. 5.3. The spike height still shows a weak correlation with the density contrast and HI fraction. It is also still visible that h_s increases with decreasing redshift. However, this effect is now less clear for w_s , although it is still arguably visible. Overall, though, both Figs. 5.11 and 5.23 show that noise does not significantly affect the results.

This is also to be seen for the relation of spike to underdensity widths, which is shown in Fig. 5.24. Compared to the right column of Fig. 5.12, which shows the results for the original spectra, the outcome is practically identical. However, the bottom panel reveals that the width of detected spikes very slightly increases with redshift.

The synthetic pollution of the spectra with realistic observational noise shows that the measurement of spikes is still possible when fitting the obtained signal. The inferred relation between spike and void widths does not significantly differ from that previously found for the analysis of the original, infinite-S/N spectra. Similarly, the relation between spike width and height and the IGM properties is still clearly visible, although the individual distributions show small discrepancies compared to before. Thus, we conclude that the noise does not significantly alter our results.

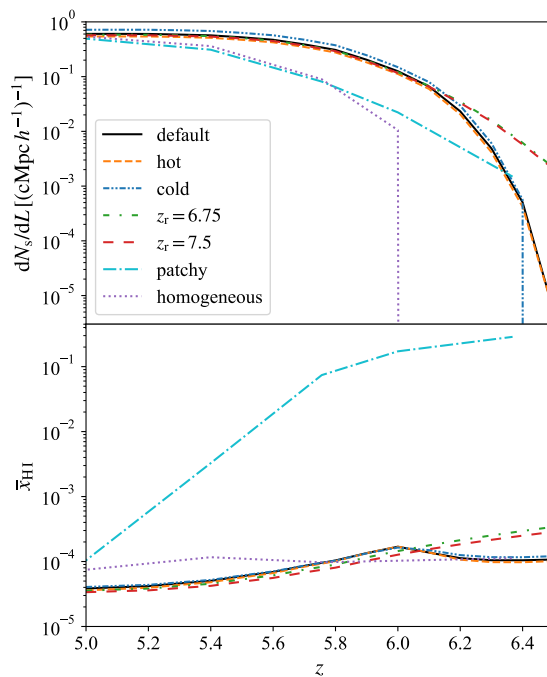


Figure 5.22. Same as Fig. 5.1b except that results are shown for noisy spectra with $S/N = 30$ here. The spike number density evolution is almost identical to the original data at lower redshifts. At a certain redshift, the number density of spikes drops rapidly in each model. This is because the spikes disappear due to their height being similar to or below the noise level.

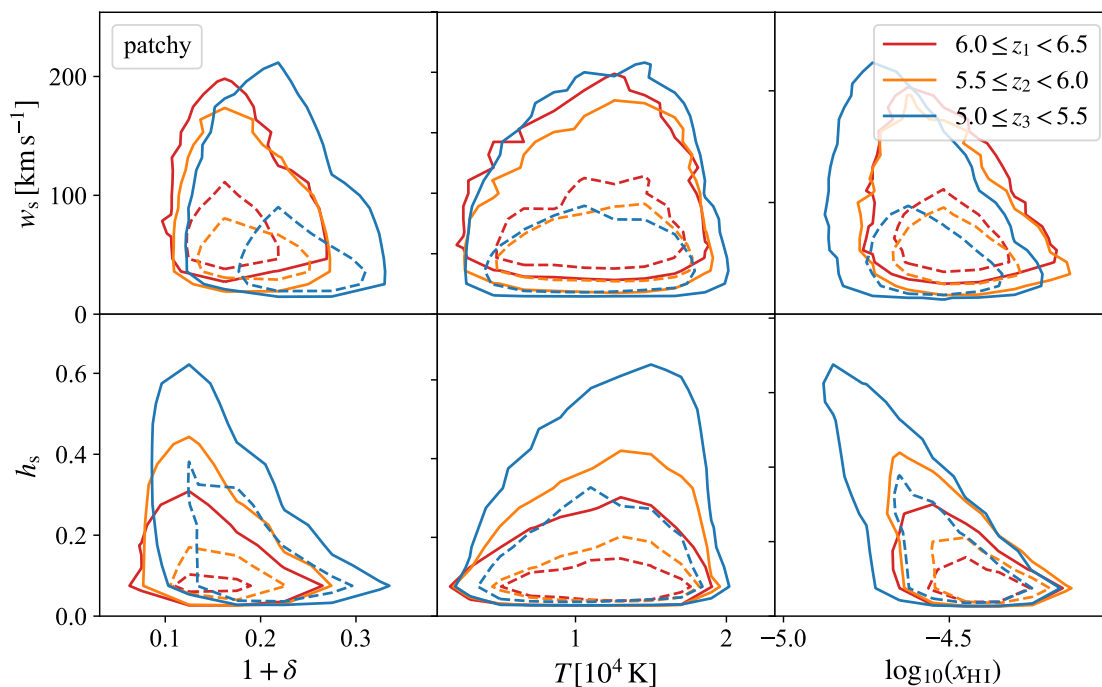


Figure 5.23. Same as Fig. 5.11 except that results are shown for the noisy spectra with $S/N = 30$ here. Although the distributions show small differences compared to the original data, the correlations are unaffected by the noise.

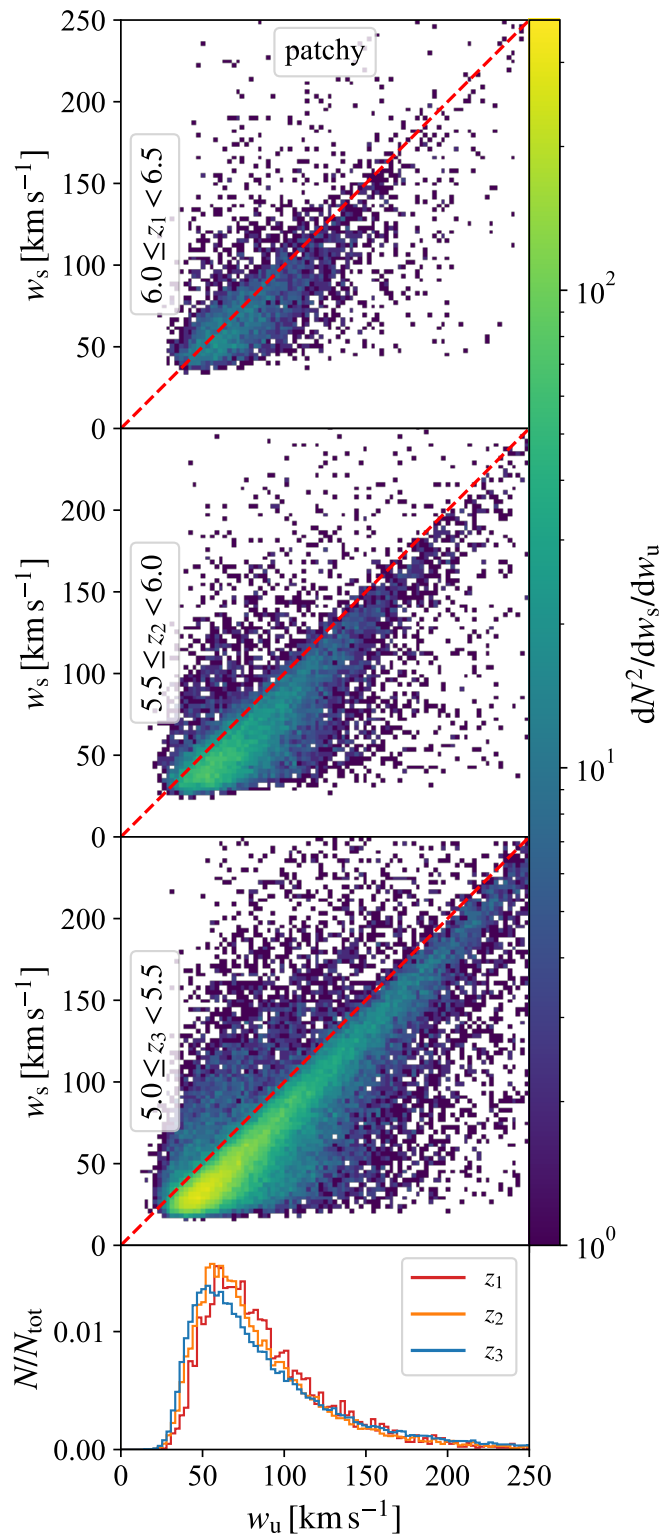


Figure 5.24. Same as Fig. 5.15 except that results are shown for the noisy spectra with S/N = 30 here. There are no visible differences for the correlation between spike and void widths compared to the original data (right column of Fig. 5.12).

Chapter 6

Summary and discussion

Cosmic voids occupy most of the volume in the Universe and directly influence the evolution of the cosmic web. However, the content of voids is difficult to observe. Ly α transmission spikes in high- z QSO spectra, however, potentially allow a direct measurement of the central contents of voids and the ability to constrain information about cosmic reionization and the properties of the IGM. In this work we tested how well the Ly α forest is able to probe the characteristics of voids and their gas contents. We investigated individual LOSs for different runs of the SHERWOOD RELICS simulations, and statistically studied whole simulation runs that deploy different assumptions to compare the effect of these on Ly α transmission spikes. Our main results are as follows:

- (i). The different runs show that a homogeneous UVB model does not produce realistic spectra agreeing with observations at $z \gtrsim z_r$, i.e. during the EoR. Although they show a very similar evolution of $x_{\text{H I}}$, they reveal no transmission spikes at all until very shortly after z_r . On the other hand, the patchy UVB model does show transmission in underdense regions throughout the investigated redshift range. Here, Ly α transmission spikes arise from already highly ionized regions.
- (ii). By studying the contribution of individual pixels to the absorption (i.e. optical depth) in spikes, we find that with increasing IGM temperature the details of the spikes are smoothed due to the resulting pressure smoothing of the density field and thermal broadening of the spectral lines. As a result, the model with a lower IGM temperature shows more separated spikes, which reproduce the density field to a better extent.
- (iii). We probed which areas of the underdensities mainly contribute to absorption at spike peaks. The simulations reveal that the major contribution results from the central region of the void, where the edges only add to the optical depth in rare cases. In addition, overdense regions situated close to underdensities are also able to contribute, although marginally. We therefore confirm that Ly α transmission spikes probe the central contents of cosmic voids.
- (iv). Whilst [Garaldi et al. \(2019\)](#) measured spike and underdensity width at FWHM to investigate spike and IGM properties, we deployed a different method for this purpose: we measured the transmission spike width at a fixed threshold and use the 95th percentile of δ at the spike edges (i.e. the real space pixel that produced the

transmission at the spike edge) at each respective redshift to measure the width of the voids. Using this method, we find a strong linear correlation with slope ~ 1 between spike and underdensity width along all LOSs throughout the investigated redshift range. We therefore conclude that Ly α spikes are a promising tool to study cosmic voids and may allow us to infer the void size distribution from high- z QSO spectra.

- (v). We connected each transmission spike to the respective region which produced it and, thereby, investigated the connection of IGM properties to the spike width and height. The *default*, *hot*, and *cold* IGM model, which employed different photoheating rates and, hence, possess different IGM temperatures during and after reionization, as well as the *patchy* reionization model reveal that the spike width and height increase with T . In addition, we find a weak, negative correlation between spike widths and δ as well as x_{HI} for all investigated models. The spike height, on the other hand, shows a strong, negative correlation to δ and x_{HI} . Hence, as expected, denser regions with higher HI fractions produce smaller and fewer spikes as they cause more absorption. By inferring the exact relation between these quantities, Ly α transmission spikes might enable measuring these gas properties in cosmic voids from Ly α spectra.
- (vi). Comparing models deploying a homogeneous UVB with different photoionization rates lets us conclude that the inferred results are in fact unaffected by the reionization history in the redshift range we investigate here if the instantaneous temperature is similar. Rescaling spectra to arbitrary effective optical depths shows that the scaling alters the results. As a conclusion, we argue that it is necessary to scale simulated spectra to observed mean transmissions.
- (vii). We added Gaussian and Poisson noise to the spectra to reproduce realistic observations with $S/N = 30$. To the resultant spectra we applied a Wiener filter and deconvolution of the line spread function to enable a clear identification and measurement of transmission spikes. The original spectra are well recovered, and we find that noise does not affect our results.

In addition to this, in Figure 4.7 we present another possible application of our method. Here we show that the relation of δ to \overline{F} does not significantly differ in any of the investigated simulation models and is hence almost independent from the initial conditions. Therefore, if the spike width is measured at the same threshold in simulation and real data, Fig. 4.7 might allow one to see at which density contrasts the underdensity extents are measured along an observed LOS. Similarly, Fig. 4.5 might be a starting point in reconstructing the gas density field in voids along the LOS from shapes of transmission spikes in high- z Ly α spectra.

Throughout this work, we have applied our developed technique of spike width measurement at a fixed threshold to measure the elongation of underdensities along specific LOSs. We find that Ly α transmission spikes enable measuring void sizes and their gas contents, and hence allow probing the characteristics of the IGM shortly after and during the tail end of the EoR. In particular, the HI fraction (i.e. the ionization degree) and the density are measurable from spike properties. Thus, Ly α transmission spikes allow to directly probe the underdensest regions of the high-redshift universe.

Acknowledgements

The years 2020 and 2021, of course, were by no means usual. In February 2020, amidst the preparation for my final thesis, my daughter was born – luckily just before the first Corona measures were taken. To afford the additional costs, I simultaneously had to work a part-time job, which was a very stressful situation for me. Nevertheless, due to great consideration by my supervisor Prof. Dr. Christoph Pfrommer and assisting supervisor Dr. Ewald Puchwein, I was still able to focus on my thesis and finish according to my expectations. Especially, I want to thank Ewald for his excellent support throughout the project, who was always extremely helpful and very engaged to tutor me. I am happy for every future student that will be given the opportunity to work under your supervision. Furthermore, I want to thank my wife for supporting me such that I was able to focus on my final thesis. Although the forced long-term home office situation due to the Corona pandemic, I am very happy that I have had the opportunity to spend much valuable time with my new beloved family. Lastly, I want to thank my parents for their great support throughout the past years.

Bibliography

- Alonso D., Hill J. C., Hložek R., Spergel D. N., 2018. Measurement of the thermal Sunyaev-Zel'dovich effect around cosmic voids. *Phys. Rev. D*, **97**, 063514
- Arons J., McCray R., 1970. Photo-Ionization of Intergalactic Hydrogen by Quasars. *Astrophys. Lett.*, **5**, 123
- Aubert D., Teyssier R., 2008. A radiative transfer scheme for cosmological reionization based on a local Eddington tensor. *MNRAS*, **387**, 295
- Barnett R., Warren S. J., Becker G. D., Mortlock D. J., Hewett P. C., McMahon R. G., Simpson C., Venemans B. P., 2017. Observations of the Lyman series forest towards the redshift 7.1 quasar ULAS J1120+0641. *A&A*, **601**, A16
- Becker G. D., Bolton J. S., 2013. New measurements of the ionizing ultraviolet background over $2 < z < 5$ and implications for hydrogen reionization. *MNRAS*, **436**, 1023
- Becker G. D., Bolton J. S., Haehnelt M. G., Sargent W. L. W., 2011. Detection of extended He II reionization in the temperature evolution of the intergalactic medium. *MNRAS*, **410**, 1096
- Becker G. D., Bolton J. S., Madau P., Pettini M., Ryan-Weber E. V., Venemans B. P., 2015. Evidence of patchy hydrogen reionization from an extreme Ly α trough below redshift six. *MNRAS*, **447**, 3402
- Bennett C. L., et al., 2013. Nine-year Wilkinson Microwave Anisotropy Probe (WMAP) Observations: Final Maps and Results. *ApJS*, **208**, 20
- Bernstein R., Shtetman S. A., Gunnels S. M., Mochnacki S., Athey A. E., 2003. in Iye M., Moorwood A. F. M., eds, Society of Photo-Optical Instrumentation Engineers (SPIE) Conference Series Vol. 4841, Instrument Design and Performance for Optical/Infrared Ground-based Telescopes. pp 1694–1704, doi:10.1117/12.461502
- Beygu B., Kreckel K., van de Weygaert R., van der Hulst J. M., van Gorkom J. H., 2013. An Interacting Galaxy System along a Filament in a Void. *AJ*, **145**, 120
- Beygu B., Kreckel K., van der Hulst J. M., Jarrett T. H., Peletier R., van de Weygaert R., van Gorkom J. H., Aragon-Calvo M. A., 2016. The void galaxy survey: Star formation properties. *MNRAS*, **458**, 394

- Beygu B., Peletier R. F., van der Hulst J. M., Jarrett T. H., Kreckel K., van de Weygaert R., van Gorkom J. H., Aragon-Calvo M. A., 2017. The void galaxy survey: photometry, structure and identity of void galaxies. *MNRAS*, **464**, 666
- Biswas R., Alizadeh E., Wandelt B. D., 2010. Voids as a precision probe of dark energy. *Phys. Rev. D*, **82**, 023002
- Blumenthal G. R., Faber S. M., Primack J. R., Rees M. J., 1984. Formation of galaxies and large-scale structure with cold dark matter. *Nature*, **311**, 517
- Boera E., Becker G. D., Bolton J. S., Nasir F., 2019. Revealing Reionization with the Thermal History of the Intergalactic Medium: New Constraints from the Ly α Flux Power Spectrum. *ApJ*, **872**, 101
- Bolton J. S., Haehnelt M. G., Viel M., Springel V., 2005. The Lyman α forest opacity and the metagalactic hydrogen ionization rate at $z \sim 2-4$. *MNRAS*, **357**, 1178
- Bolton J. S., Becker G. D., Haehnelt M. G., Viel M., 2014. A consistent determination of the temperature of the intergalactic medium at redshift $z = 2.4$. *MNRAS*, **438**, 2499
- Bolton J. S., Puchwein E., Sijacki D., Haehnelt M. G., Kim T.-S., Meiksin A., Regan J. A., Viel M., 2017. The Sherwood simulation suite: overview and data comparisons with the Lyman α forest at redshifts $2 \leq z \leq 5$. *MNRAS*, **464**, 897
- Bos E. G. P., van de Weygaert R., Dolag K., Pettorino V., 2012. The darkness that shaped the void: dark energy and cosmic voids. *MNRAS*, **426**, 440
- Bosman S. E. I., Fan X., Jiang L., Reed S., Matsuoka Y., Becker G., Haehnelt M., 2018. New constraints on Lyman- α opacity with a sample of 62 quasars at $z > 5.7$. *MNRAS*, **479**, 1055
- Bouwens R. J., et al., 2015. UV Luminosity Functions at Redshifts $z \sim 4$ to $z \sim 10$: 10,000 Galaxies from HST Legacy Fields. *ApJ*, **803**, 34
- Bowler R. A. A., et al., 2014. The bright end of the galaxy luminosity function at $z \simeq 7$: before the onset of mass quenching. *MNRAS*, **440**, 2810
- Bowler R. A. A., et al., 2015. The galaxy luminosity function at $z \simeq 6$ and evidence for rapid evolution in the bright end from $z \simeq 7$ to 5. *MNRAS*, **452**, 1817
- Boylan-Kolchin M., Springel V., White S. D. M., Jenkins A., Lemson G., 2009. Resolving cosmic structure formation with the Millennium-II Simulation. *MNRAS*, **398**, 1150
- Bromm V., Larson R. B., 2004. The First Stars. *ARA&A*, **42**, 79
- Bromm V., Yoshida N., 2011. The First Galaxies. *ARA&A*, **49**, 373
- Ceccarelli L., Paz D., Lares M., Padilla N., Lambas D. G., 2013. Clues on void evolution - I. Large-scale galaxy distributions around voids. *MNRAS*, **434**, 1435

- Chardin J., Haehnelt M. G., Aubert D., Puchwein E., 2015. Calibrating cosmological radiative transfer simulations with Ly α forest data: evidence for large spatial UV background fluctuations at $z \sim 5.6$ - 5.8 due to rare bright sources. *MNRAS*, **453**, 2943
- Chardin J., Haehnelt M. G., Bosman S. E. I., Puchwein E., 2018. A tale of seven narrow spikes and a long trough: constraining the timing of the percolation of H II bubbles at the tail end of reionization with ULAS J1120+0641. *MNRAS*, **473**, 765
- Ciardi B., Madau P., 2003. Probing beyond the Epoch of Hydrogen Reionization with 21 Centimeter Radiation. *ApJ*, **596**, 1
- Clampitt J., Cai Y.-C., Li B., 2013. Voids in modified gravity: excursion set predictions. *MNRAS*, **431**, 749
- Colberg J. M., Sheth R. K., Diaferio A., Gao L., Yoshida N., 2005. Voids in a Λ CDM universe. *MNRAS*, **360**, 216
- Cooke J., Ryan-Weber E. V., Garel T., Díaz C. G., 2014. Lyman-continuum galaxies and the escape fraction of Lyman-break galaxies. *MNRAS*, **441**, 837
- Davé R., et al., 2001. Baryons in the Warm-Hot Intergalactic Medium. *ApJ*, **552**, 473
- Di Matteo T., Perna R., Abel T., Rees M. J., 2002. Radio Foregrounds for the 21 Centimeter Tomography of the Neutral Intergalactic Medium at High Redshifts. *ApJ*, **564**, 576
- Dicke R. H., Peebles P. J. E., Roll P. G., Wilkinson D. T., 1965. Cosmic Black-Body Radiation. *ApJ*, **142**, 414
- Eide M. B., Graziani L., Ciardi B., Feng Y., Kakiichi K., Di Matteo T., 2018. The epoch of cosmic heating by early sources of X-rays. *MNRAS*, **476**, 1174
- Eilers A.-C., Davies F. B., Hennawi J. F., 2018. The Opacity of the Intergalactic Medium Measured along Quasar Sightlines at $z \sim 6$. *ApJ*, **864**, 53
- Einasto J., Joveer M., Saar E., 1980. Structure of superclusters and supercluster formation. *MNRAS*, **193**, 353
- Einasto M., et al., 2012. Multimodality of rich clusters from the SDSS DR8 within the supercluster-void network. *A&A*, **542**, A36
- Fan X., et al., 2006. Constraining the Evolution of the Ionizing Background and the Epoch of Reionization with $z \sim 6$ Quasars. II. A Sample of 19 Quasars. *AJ*, **132**, 117
- Fan X., et al., 2019. The Discovery of a Gravitationally Lensed Quasar at $z = 6.51$. *ApJ*, **870**, L11
- Faucher-Giguère C.-A., Lidz A., Hernquist L., Zaldarriaga M., 2008. A Flat Photoionization Rate at $2 \leq z \leq 4.2$: Evidence for a Stellar-Dominated UV Background and against a Decline of Cosmic Star Formation beyond $z \sim 3$. *ApJ*, **682**, L9

- Ferrara A., Pandolfi S., 2014. Reionization of the Intergalactic Medium. arXiv e-prints, p. [arXiv:1409.4946](#)
- Finkelstein S. L., et al., 2015. The Evolution of the Galaxy Rest-frame Ultraviolet Luminosity Function over the First Two Billion Years. *ApJ*, **810**, 71
- Fixsen D. J., 2009. The Temperature of the Cosmic Microwave Background. *ApJ*, **707**, 916
- Frebel A., Norris J. E., 2015. Near-Field Cosmology with Extremely Metal-Poor Stars. *ARA&A*, **53**, 631
- Frisch P., Einasto J., Einasto M., Freudling W., Fricke K. J., Gramann M., Saar V., Toomet O., 1995. Evolution of the supercluster-void network.. *A&A*, **296**, 611
- Furlanetto S. R., Oh S. P., 2009. The Temperature-Density Relation of the Intergalactic Medium after Hydrogen Reionization. *ApJ*, **701**, 94
- Furlanetto S. R., Oh S. P., Briggs F. H., 2006. Cosmology at low frequencies: The 21 cm transition and the high-redshift Universe. *Phys. Rep.*, **433**, 181
- Gaikwad P., et al., 2020. Probing the thermal state of the intergalactic medium at $z > 5$ with the transmission spikes in high-resolution Ly α forest spectra. *MNRAS*, **494**, 5091
- Garaldi E., Gnedin N. Y., Madau P., 2019. Constraining the Tail End of Reionization Using Ly α Transmission Spikes. *ApJ*, **876**, 31
- Giallongo E., et al., 2015. Faint AGNs at $z > 4$ in the CANDELS GOODS-S field: looking for contributors to the reionization of the Universe. *A&A*, **578**, A83
- Gnedin N. Y., 2014. Cosmic Reionization on Computers. I. Design and Calibration of Simulations. *ApJ*, **793**, 29
- Gnedin N. Y., Kaurov A. A., 2014. Cosmic Reionization on Computers. II. Reionization History and Its Back-reaction on Early Galaxies. *ApJ*, **793**, 30
- Gnedin N. Y., Kravtsov A. V., Chen H.-W., 2008. Escape of Ionizing Radiation from High-Redshift Galaxies. *ApJ*, **672**, 765
- Goldberg D. M., Jones T. D., Hoyle F., Rojas R. R., Vogeley M. S., Blanton M. R., 2005. The Mass Function of Void Galaxies in the Sloan Digital Sky Survey Data Release 2. *ApJ*, **621**, 643
- Goldwire Henry C. J., 1968. Oscillator Strengths for Electric Dipole Transitions of Hydrogen. *ApJS*, **17**, 445
- Gottlöber S., Łokas E. L., Klypin A., Hoffman Y., 2003. The structure of voids. *MNRAS*, **344**, 715
- Gunn J. E., Peterson B. A., 1965. On the Density of Neutral Hydrogen in Intergalactic Space. *ApJ*, **142**, 1633

- Gurnett D. A., Bhattacharjee A., 2005. Introduction to Plasma Physics
- Haardt F., Madau P., 2012. Radiative Transfer in a Clumpy Universe. IV. New Synthesis Models of the Cosmic UV/X-Ray Background. *ApJ*, 746, 125
- Hamaus N., Sutter P. M., Wandelt B. D., 2014. Universal Density Profile for Cosmic Voids. *Phys. Rev. Lett.*, 112, 251302
- Heisenberg W., 1927. Über den anschaulichen Inhalt der quantentheoretischen Kinematik und Mechanik. *Zeitschrift für Physik*, 43, 172
- Hinshaw G., et al., 2013. Nine-year Wilkinson Microwave Anisotropy Probe (WMAP) Observations: Cosmological Parameter Results. *ApJS*, 208, 19
- Hiss H., Walther M., Hennawi J. F., Oñorbe J., O’Meara J. M., Rorai A., Lukić Z., 2018. A New Measurement of the Temperature-density Relation of the IGM from Voigt Profile Fitting. *ApJ*, 865, 42
- Hjerting F., 1938. Tables Facilitating the Calculation of Line Absorption Coefficients.. *ApJ*, 88, 508
- Hoyle F., Vogeley M. S., 2002. Voids in the Point Source Catalogue Survey and the Updated Zwicky Catalog. *ApJ*, 566, 641
- Hui L., Gnedin N. Y., 1997. Equation of state of the photoionized intergalactic medium. *MNRAS*, 292, 27
- Hummer D. G., 1965. The Voigt function: An eight-significant-figure table and generating procedure. *MmRAS*, 70, 1
- Iwata I., et al., 2009. Detections of Lyman Continuum from Star-Forming Galaxies at $z \sim 3$ through Subaru/Suprime-Cam Narrow-Band Imaging. *ApJ*, 692, 1287
- Johnson J. L., Khochfar S., 2011. The Contribution of Supernovae to Cosmic Reionization. *ApJ*, 743, 126
- Kallenrode M.-B., 2004. Space physics: an introduction to plasmas and particles in the heliosphere and magnetospheres
- Keating L. C., Weinberger L. H., Kulkarni G., Haehnelt M. G., Chardin J., Aubert D., 2020. Long troughs in the Lyman- α forest below redshift 6 due to islands of neutral hydrogen. *MNRAS*, 491, 1736
- Kimm T., Cen R., 2014. Escape Fraction of Ionizing Photons during Reionization: Effects due to Supernova Feedback and Runaway OB Stars. *ApJ*, 788, 121
- Kirshner R. P., Oemler A. J., Schechter P. L., Shectman S. A., 1981. A million cubic megaparsec void in Bootes. *ApJ*, 248, L57
- Kreckel K., et al., 2011. Only the Lonely: H I Imaging of Void Galaxies. *AJ*, 141, 4

- Kreckel K., Platen E., Aragón-Calvo M. A., van Gorkom J. H., van de Weygaert R., van der Hulst J. M., Beygu B., 2012. The Void Galaxy Survey: Optical Properties and H I Morphology and Kinematics. *AJ*, **144**, 16
- Kulkarni G., Keating L. C., Haehnelt M. G., Bosman S. E. I., Puchwein E., Chardin J., Aubert D., 2019a. Large Ly α opacity fluctuations and low CMB τ in models of late reionization with large islands of neutral hydrogen extending to $z < 5.5$. *MNRAS*, **485**, L24
- Kulkarni G., Worseck G., Hennawi J. F., 2019b. Evolution of the AGN UV luminosity function from redshift 7.5. *MNRAS*, **488**, 1035
- Ma X., Kasen D., Hopkins P. F., Faucher-Giguère C.-A., Quataert E., Kereš D., Murray N., 2015. The difficulty of getting high escape fractions of ionizing photons from high-redshift galaxies: a view from the FIRE cosmological simulations. *MNRAS*, **453**, 960
- Madau P., Haardt F., 2015. Cosmic Reionization after Planck: Could Quasars Do It All?. *ApJ*, **813**, L8
- Madau P., Meiksin A., Rees M. J., 1997. 21 Centimeter Tomography of the Intergalactic Medium at High Redshift. *ApJ*, **475**, 429
- Masters D., et al., 2012. Evolution of the Quasar Luminosity Function over $3 < z < 5$ in the COSMOS Survey Field. *ApJ*, **755**, 169
- Mather J. C., et al., 1990. A Preliminary Measurement of the Cosmic Microwave Background Spectrum by the Cosmic Background Explorer (COBE) Satellite. *ApJ*, **354**, L37
- McGreer I. D., Mesinger A., D’Odorico V., 2015. Model-independent evidence in favour of an end to reionization by $z \approx 6$. *MNRAS*, **447**, 499
- McQuinn M., 2016. The Evolution of the Intergalactic Medium. *ARA&A*, **54**, 313
- Meiksin A. A., 2009. The physics of the intergalactic medium. *Reviews of Modern Physics*, **81**, 1405
- Melchior P., Sutter P. M., Sheldon E. S., Krause E., Wandelt B. D., 2014. First measurement of gravitational lensing by cosmic voids in SDSS. *MNRAS*, **440**, 2922
- Mirabel I. F., Dijkstra M., Laurent P., Loeb A., Pritchard J. R., 2011. Stellar black holes at the dawn of the universe. *A&A*, **528**, A149
- Naoz S., Noter S., Barkana R., 2006. The first stars in the Universe. *MNRAS*, **373**, L98
- Nestor D. B., Shapley A. E., Kornei K. A., Steidel C. C., Siana B., 2013. A Refined Estimate of the Ionizing Emissivity from Galaxies at $z \sim 3$: Spectroscopic Follow-up in the SSA22a Field. *ApJ*, **765**, 47
- Nierenberg A. M., Treu T., Wright S. A., Fassnacht C. D., Auger M. W., 2014. Detection of substructure with adaptive optics integral field spectroscopy of the gravitational lens B1422+231. *MNRAS*, **442**, 2434

- Oh S. P., 2001. Reionization by Hard Photons. I. X-Rays from the First Star Clusters. *ApJ*, **553**, 499
- Oh S. P., Mack K. J., 2003. Foregrounds for 21-cm observations of neutral gas at high redshift. *MNRAS*, **346**, 871
- Padovani P., et al., 2017. Active galactic nuclei: what's in a name?. *A&A Rev.*, **25**, 2
- Park C., Choi Y.-Y., Kim J., Gott J. Richard I., Kim S. S., Kim K.-S., 2012. The Challenge of the Largest Structures in the Universe to Cosmology. *ApJ*, **759**, L7
- Paz D., Lares M., Ceccarelli L., Padilla N., Lambas D. G., 2013. Clues on void evolution-II. Measuring density and velocity profiles on SDSS galaxy redshift space distortions. *MNRAS*, **436**, 3480
- Peebles P. J. E., 1968. Recombination of the Primeval Plasma. *ApJ*, **153**, 1
- Peebles P. J. E., 1993. Principles of Physical Cosmology
- Penzias A. A., Wilson R. W., 1965. A Measurement of Excess Antenna Temperature at 4080 Mc/s. *ApJ*, **142**, 419
- Planck Collaboration et al., 2011. Planck early results. I. The Planck mission. *A&A*, **536**, A1
- Planck Collaboration et al., 2014. Planck 2013 results. XVI. Cosmological parameters. *A&A*, **571**, A16
- Planck Collaboration et al., 2016. Planck intermediate results. XLVII. Planck constraints on reionization history. *A&A*, **596**, A108
- Planck Collaboration et al., 2018. Planck 2018 results. VI. Cosmological parameters. arXiv e-prints, p. [arXiv:1807.06209](https://arxiv.org/abs/1807.06209)
- Platen E., van de Weygaert R., Jones B. J. T., 2008. Alignment of voids in the cosmic web. *MNRAS*, **387**, 128
- Plionis M., Basilakos S., 2002. The size and shape of local voids. *MNRAS*, **330**, 399
- Pritchard J. R., Loeb A., 2012. 21 cm cosmology in the 21st century. *Reports on Progress in Physics*, **75**, 086901
- Puchwein E., Bolton J. S., Haehnelt M. G., Madau P., Becker G. D., Haardt F., 2015. The photoheating of the intergalactic medium in synthesis models of the UV background. *MNRAS*, **450**, 4081
- Puchwein E., Haardt F., Haehnelt M. G., Madau P., 2019. Consistent modelling of the meta-galactic UV background and the thermal/ionization history of the intergalactic medium. *MNRAS*, **485**, 47
- Puchwein E., Bolton J., TBD 2021. The Sherwood Relics simulations: overview and modelling the impact of patchy reionization and associated pressure-smoothing on the intergalactic medium. in prep.

- Rauch M., 1998. The Lyman Alpha Forest in the Spectra of QSOs. *ARA&A*, **36**, 267
- Rees M. J., 1997. in Tanvir N. R., Aragon-Salamanca A., Wall J. V., eds, *The Hubble Space Telescope and the High Redshift Universe*. p. 115 ([arXiv:astro-ph/9608196](https://arxiv.org/abs/astro-ph/9608196))
- Rudie G. C., Steidel C. C., Pettini M., 2012. The Temperature-Density Relation in the Intergalactic Medium at Redshift $z = 2.4$. *ApJ*, **757**, L30
- Rybicki G. B., Lightman A. P., 1986. *Radiative Processes in Astrophysics*
- Sachs R. K., Wolfe A. M., 1967. Perturbations of a Cosmological Model and Angular Variations of the Microwave Background. *ApJ*, **147**, 73
- Sánchez C., et al., 2017. Cosmic voids and void lensing in the Dark Energy Survey Science Verification data. *MNRAS*, **465**, 746
- Schechter P., 1976. An analytic expression for the luminosity function for galaxies.. *ApJ*, **203**, 297
- Schroeder J., Mesinger A., Haiman Z., 2013. Evidence of Gunn-Peterson damping wings in high- z quasar spectra: strengthening the case for incomplete reionization at $z \sim 6-7$. *MNRAS*, **428**, 3058
- Seager S., Sasselov D. D., Scott D., 2000. How Exactly Did the Universe Become Neutral?. *ApJS*, **128**, 407
- Shapiro P. R., Giroux M. L., Babul A., 1994. Reionization in a Cold Dark Matter Universe: The Feedback of Galaxy Formation on the Intergalactic Medium. *ApJ*, **427**, 25
- Sheth R. K., van de Weygaert R., 2004. A hierarchy of voids: much ado about nothing. *MNRAS*, **350**, 517
- Shull M., France K., Danforth C., Smith B., Tumlinson J., 2010. Hubble/COS Observations of the Quasar HE 2347-4342: Probing the Epoch of He II Patchy Reionization at Redshifts $z = 2.4-2.9$. arXiv e-prints, p. [arXiv:1008.2957](https://arxiv.org/abs/1008.2957)
- Siana B., et al., 2010. A Deep Hubble Space Telescope Search for Escaping Lyman Continuum Flux at $z \sim 1.3$: Evidence for an Evolving Ionizing Emissivity. *ApJ*, **723**, 241
- Smoot G. F., et al., 1991. Preliminary Results from the COBE Differential Microwave Radiometers: Large Angular Scale Isotropy of the Cosmic Microwave Background. *ApJ*, **371**, L1
- Smoot G. F., et al., 1992. Structure in the COBE Differential Microwave Radiometer First-Year Maps. *ApJ*, **396**, L1
- Springel V., 2005. The cosmological simulation code GADGET-2. *MNRAS*, **364**, 1105
- Springel V., Hernquist L., 2002. Cosmological smoothed particle hydrodynamics simulations: the entropy equation. *MNRAS*, **333**, 649

- Springel V., et al., 2005. Simulations of the formation, evolution and clustering of galaxies and quasars. *Nature*, **435**, 629
- Sunyaev R. A., Zeldovich Y. B., 1972. The Observations of Relic Radiation as a Test of the Nature of X-Ray Radiation from the Clusters of Galaxies. *Comments on Astrophysics and Space Physics*, **4**, 173
- Tepper-García T., 2006. Voigt profile fitting to quasar absorption lines: an analytic approximation to the Voigt-Hjerting function. *MNRAS*, **369**, 2025
- Theuns T., 2007. Post-graduate lectures: The intergalactic medium. *lecture notes*
- Trac H., Cen R., Loeb A., 2008. Imprint of Inhomogeneous Hydrogen Reionization on the Temperature Distribution of the Intergalactic Medium. *ApJ*, **689**, L81
- Tully R. B., Fisher J. R., 1987. Nearby galaxies Atlas
- Tully R. B., Shaya E. J., Karachentsev I. D., Courtois H. M., Kocevski D. D., Rizzi L., Peel A., 2008. Our Peculiar Motion Away from the Local Void. *ApJ*, **676**, 184
- Vegetti S., Koopmans L. V. E., Bolton A., Treu T., Gavazzi R., 2010. Detection of a dark substructure through gravitational imaging. *MNRAS*, **408**, 1969
- Vegetti S., Lagattuta D. J., McKean J. P., Auger M. W., Fassnacht C. D., Koopmans L. V. E., 2012. Gravitational detection of a low-mass dark satellite galaxy at cosmological distance. *Nature*, **481**, 341
- Viel M., Haehnelt M. G., Springel V., 2004. Inferring the dark matter power spectrum from the Lyman- α forest in high-resolution QSO absorption spectra. *MNRAS*, **354**, 684
- Vielzeuf P., et al., 2021. Dark Energy Survey Year 1 results: the lensing imprint of cosmic voids on the cosmic microwave background. *MNRAS*, **500**, 464
- Walther M., Oñorbe J., Hennawi J. F., Lukić Z., 2019. New Constraints on IGM Thermal Evolution from the Ly α Forest Power Spectrum. *ApJ*, **872**, 13
- Weltman A., et al., 2020. Fundamental physics with the Square Kilometre Array. *PASA*, **37**, e002
- Weymann R. J., Carswell R. F., Smith M. G., 1981. Absorption lines in the spectra of Quasi-Stellar Objects.. *ARA&A*, **19**, 41
- Willott C. J., et al., 2010. The Canada-France High-z Quasar Survey: Nine New Quasars and the Luminosity Function at Redshift 6. *AJ*, **139**, 906
- Wise J. H., 2019. An Introductory Review on Cosmic Reionization. arXiv e-prints, [p. arXiv:1907.06653](https://arxiv.org/abs/1907.06653)
- Wise J. H., Cen R., 2009. Ionizing Photon Escape Fractions From High-Redshift Dwarf Galaxies. *ApJ*, **693**, 984

Bibliography

Worseck G., et al., 2011. The End of Helium Reionization at $z \sim 2.7$ Inferred from Cosmic Variance in HST/COS He II Ly α Absorption Spectra. *ApJ*, 733, L24

Worseck G., Prochaska J. X., Hennawi J. F., McQuinn M., 2016. Early and Extended Helium Reionization over More Than 600 Million Years of Cosmic Time. *ApJ*, 825, 144

Zaroubi S., 2013. The Epoch of Reionization. p. 45, [doi:10.1007/978-3-642-32362-1_2](https://doi.org/10.1007/978-3-642-32362-1_2)

van de Weygaert R., Platen E., 2011. in International Journal of Modern Physics Conference Series. pp 41–66 ([arXiv:0912.2997](https://arxiv.org/abs/0912.2997)), [doi:10.1142/S2010194511000092](https://doi.org/10.1142/S2010194511000092)

Appendices

Appendix A

Spike and void width distribution

Figure [A.1](#) shows the distribution of Ly α transmission spike and underdensity widths for the *default*, *intermediate*, and *early* reionization models, where reionization completes at $z_r = 6.2, 6.75,$ and $7.5,$ respectively, retrieved following the procedure described in Section [4.3](#).

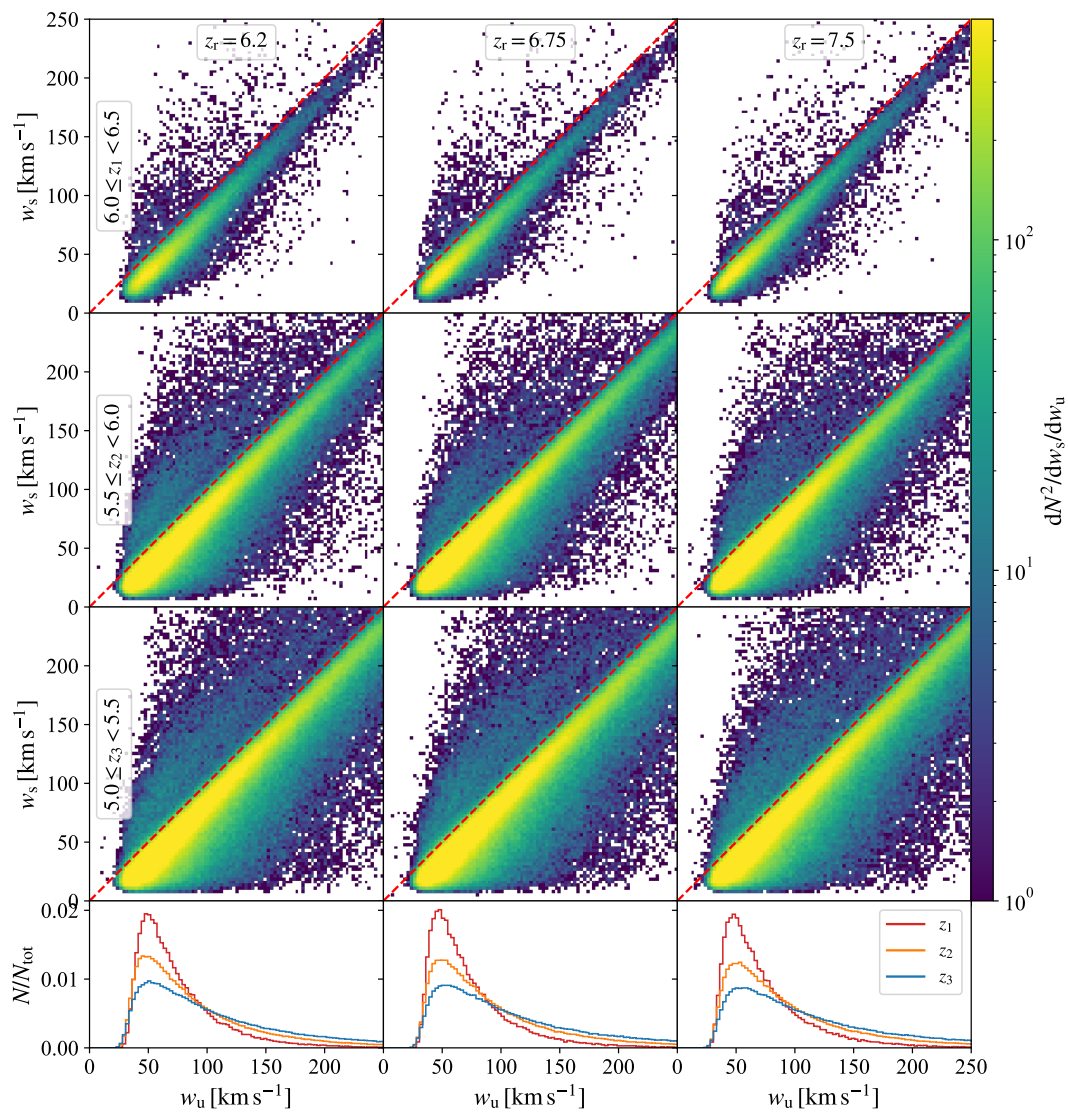


Figure A.1. Same as Fig. 5.15 except that results are here shown for the models with different reionization redshifts $z_r = 6.2$ (*default* model, left column), $z_r = 6.75$ (*intermediate* model, middle column), $z_r = 7.5$ (*early* model, right column). There are no visible differences between the three models.

Appendix B

Relation between spike shapes and gas properties

In Section 4.3 we explained how we connect a Ly α transmission spike to the spike-producing underdensity and its gas properties (i.e. density, temperature, and H I fraction). The following figures show the relation of the spike properties (width and height, where the spike widths are measured at a fixed threshold) to these gas properties for each model and all three redshift bins $6.0 \leq z_1 < 6.5$, $5.5 \leq z_2 < 6.0$, and $5.0 \leq z_3 < 5.5$.

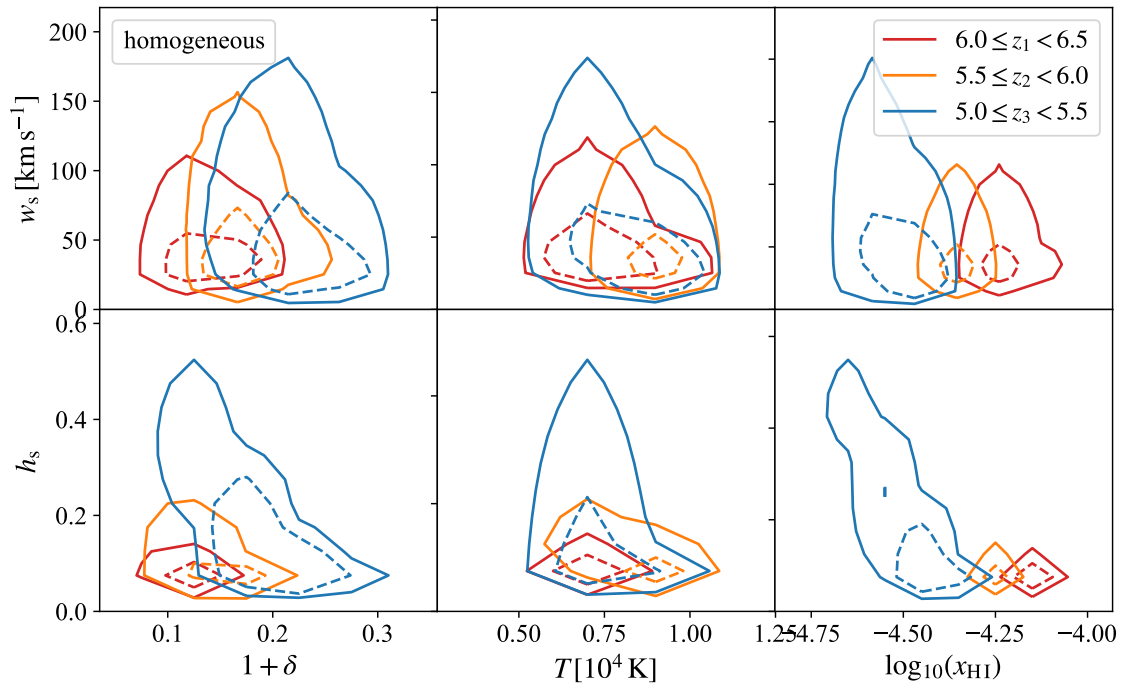


Figure B.1. Same as Fig. 5.11 except that results are shown for the *homogeneous* model here, where reionization finishes at $z_r = 5.2$. The spectra were scaled to the mean transmission of the *patchy* model. At z_1 and z_2 there are very small and narrow spikes. At z_3 , the model again reveals the same correlations between the spike properties and δ and x_{HI} as the other homogeneous UVB models.

Appendix B. Relation between spike shapes and gas properties

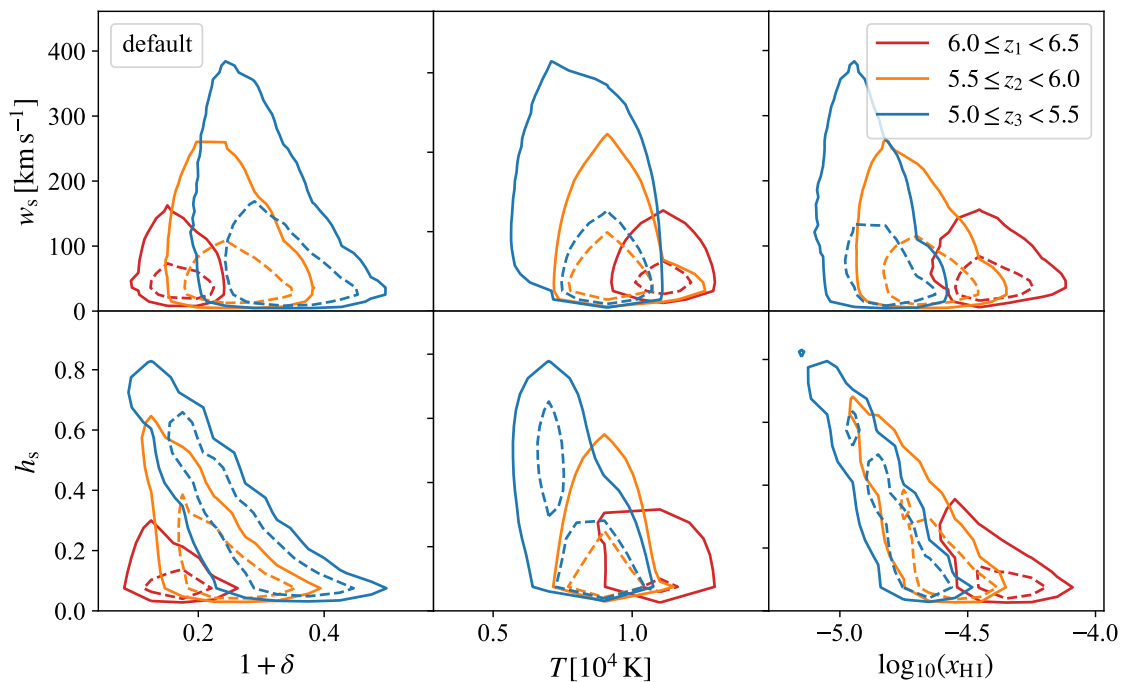


Figure B.2. Same as Fig. 5.11 except that results are shown for the *default* model here. The spectra were scaled to mean transmissions observed by (Boera et al. 2019). The same correlations between the spike properties and δ and x_{HI} as for the underlying *default* model are visible.

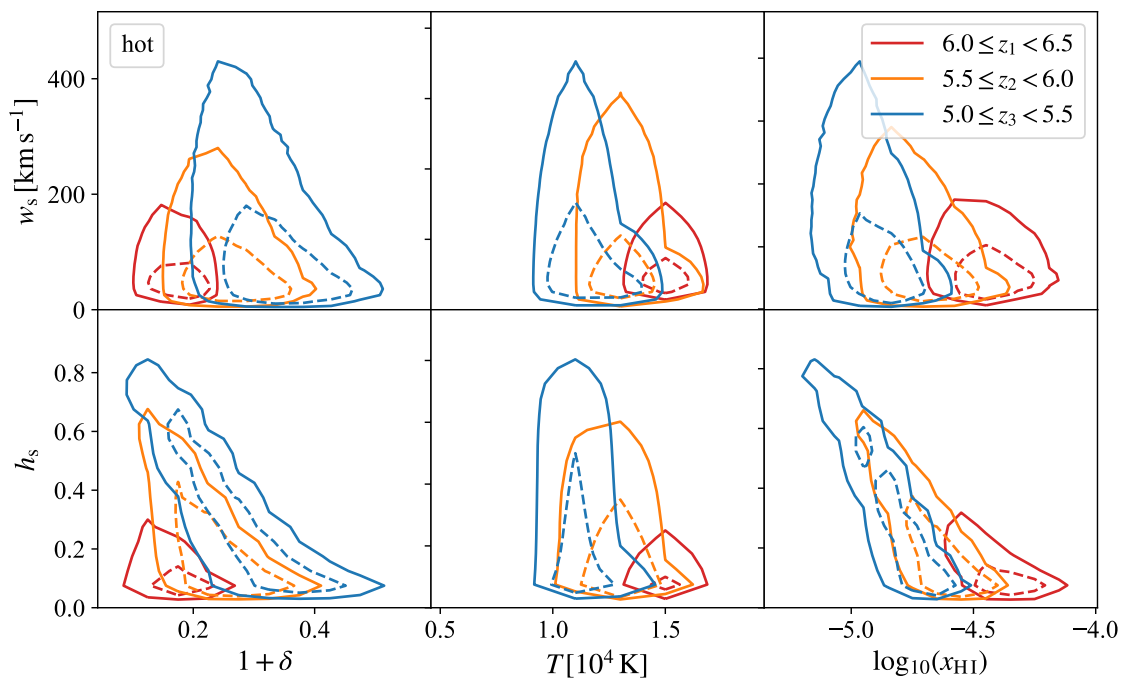


Figure B.3. Same as Fig. 5.11 except that results are shown for the *hot* model here. The spectra were scaled to mean transmissions observed by (Boera et al. 2019). The same correlations between the spike properties and δ and x_{HI} as for the underlying *default* model are visible.

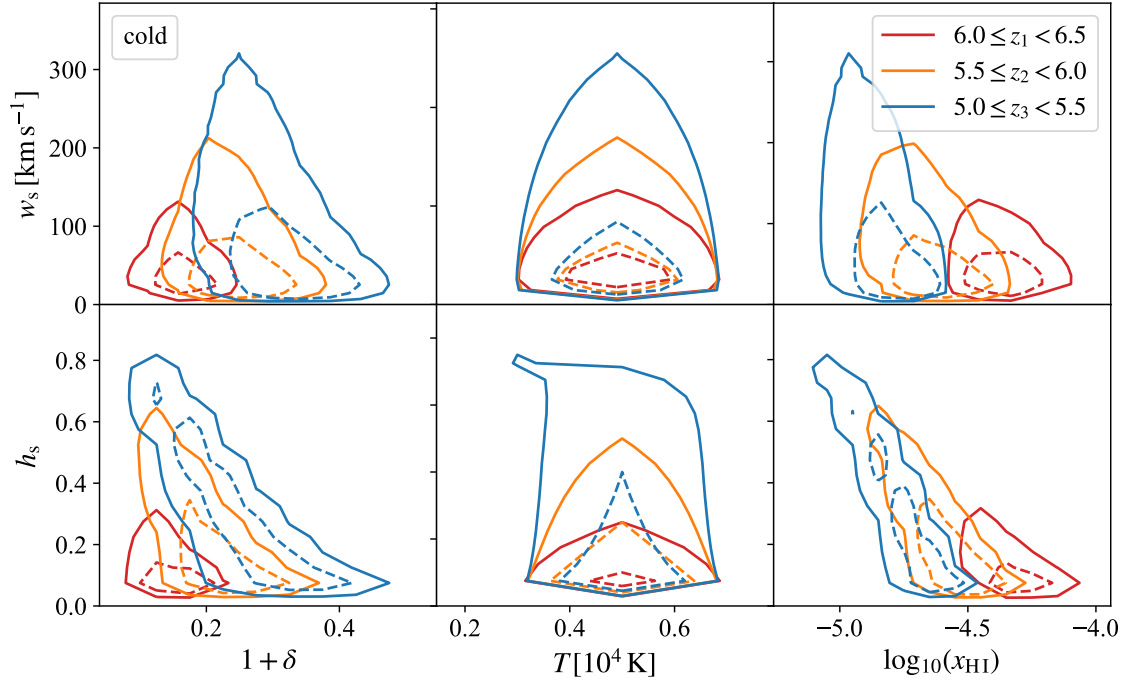


Figure B.4. Same as Fig. 5.11 except that results are shown for the *cold* model here. The spectra were scaled to mean transmissions observed by (Boera et al. 2019). The same correlations between the spike properties and δ and x_{HI} as for the underlying *default* model are visible.

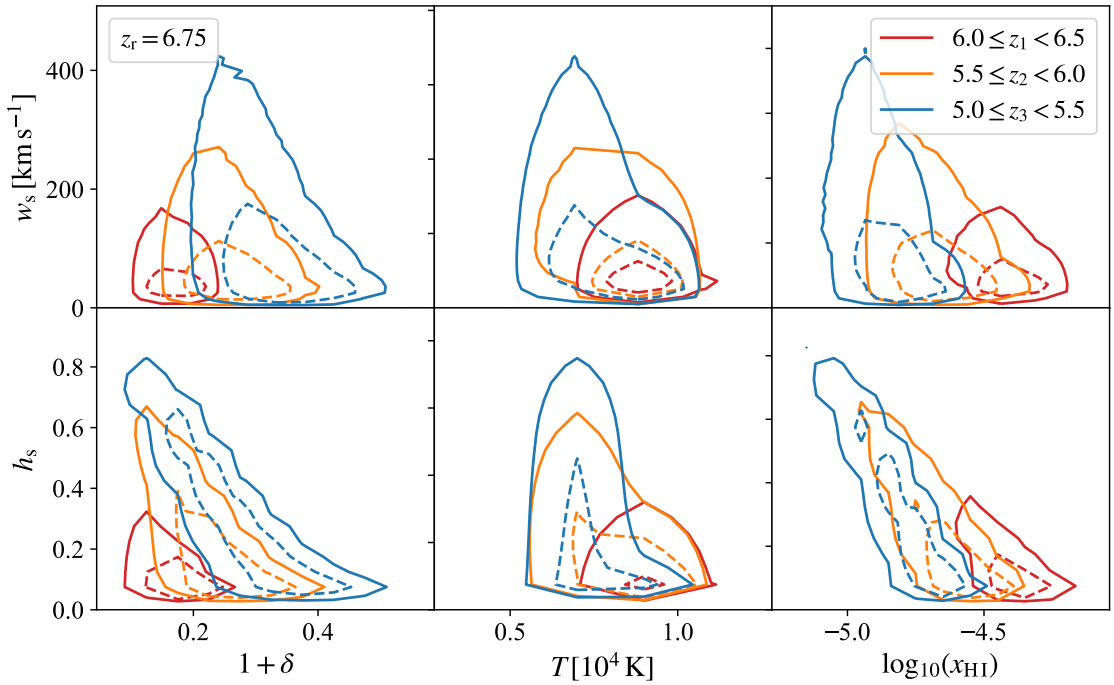


Figure B.5. Same as Fig. 5.11 except that results are shown for the *intermediate* model with $z_r = 6.75$ here. The spectra were scaled to mean transmissions observed by (Boera et al. 2019). The same correlations between the spike properties and δ and x_{HI} as for the default model are visible.

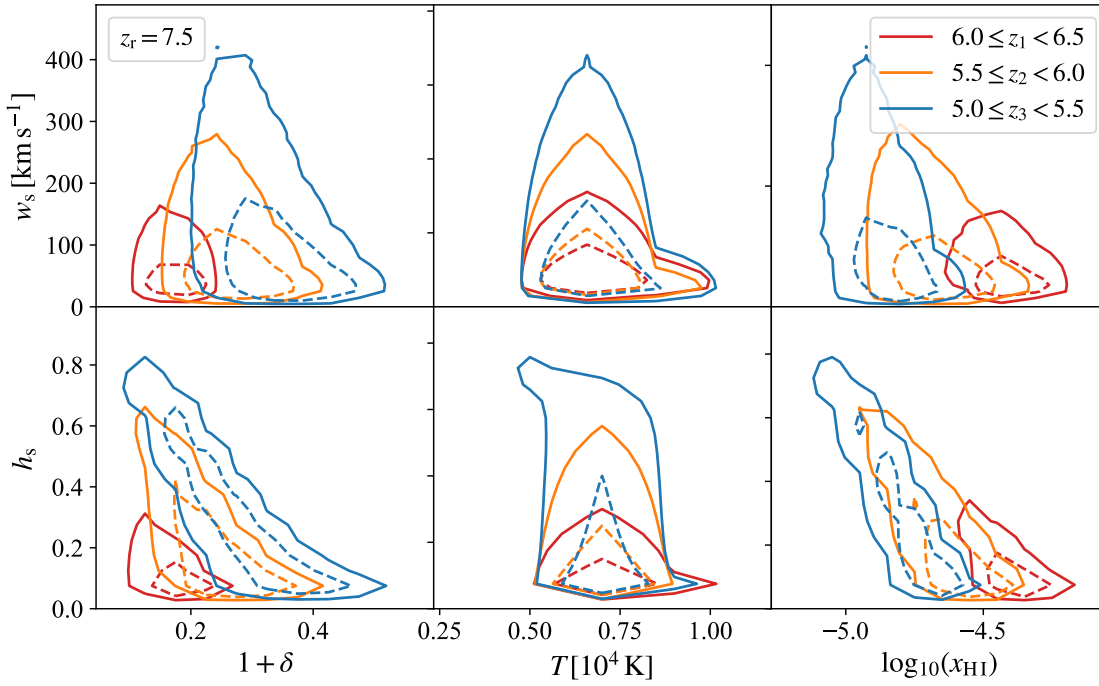


Figure B.6. Same as Fig. 5.11 except that results are shown the *early* model with $z_r = 7.5$ here. The spectra were scaled to mean transmissions observed by (Boera et al. 2019). The same correlations between the spike properties and δ and x_{HI} as for the *default* model are visible.

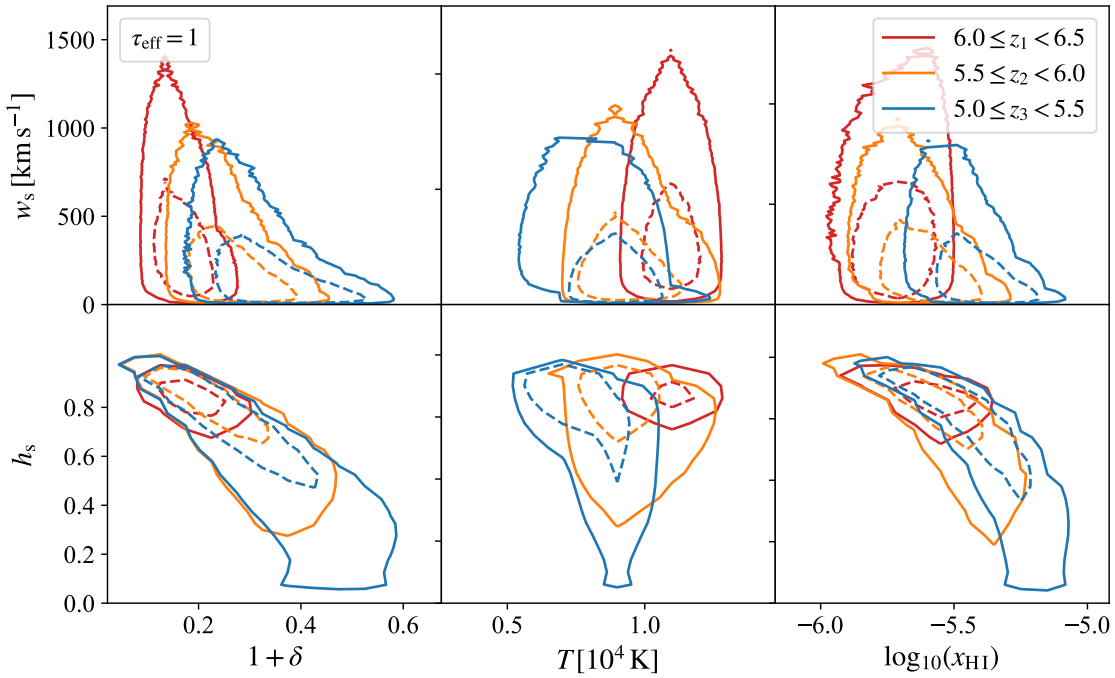


Figure B.7. Same as Fig. 5.11 except that results are shown the *default* model with a scaled effective optical depth $\tau_{\text{eff}} = 1$ here. Similar correlations between the spike properties and δ and x_{HI} as for the underlying *default* model are visible, although almost linear for h_s .

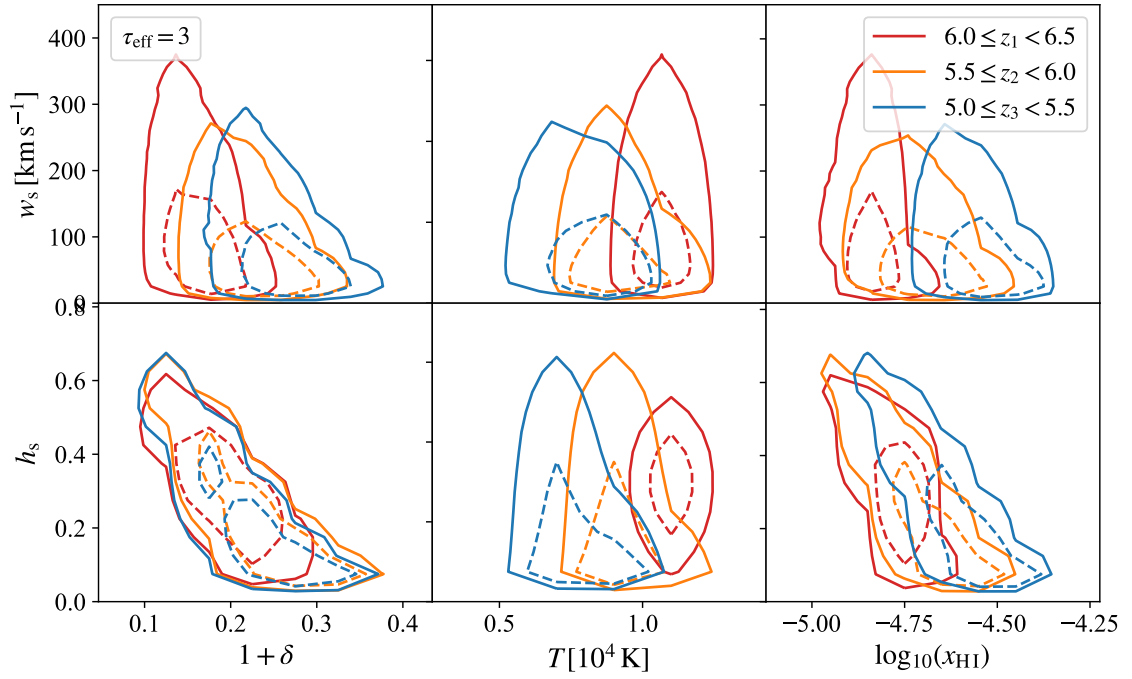


Figure B.8. Same as Fig. 5.11 except that results are shown the *default* model with a scaled effective optical depth $\tau_{\text{eff}} = 3$ here. The same correlations between the spike properties and δ and x_{HI} as for the underlying *default* model at z_3 are visible.

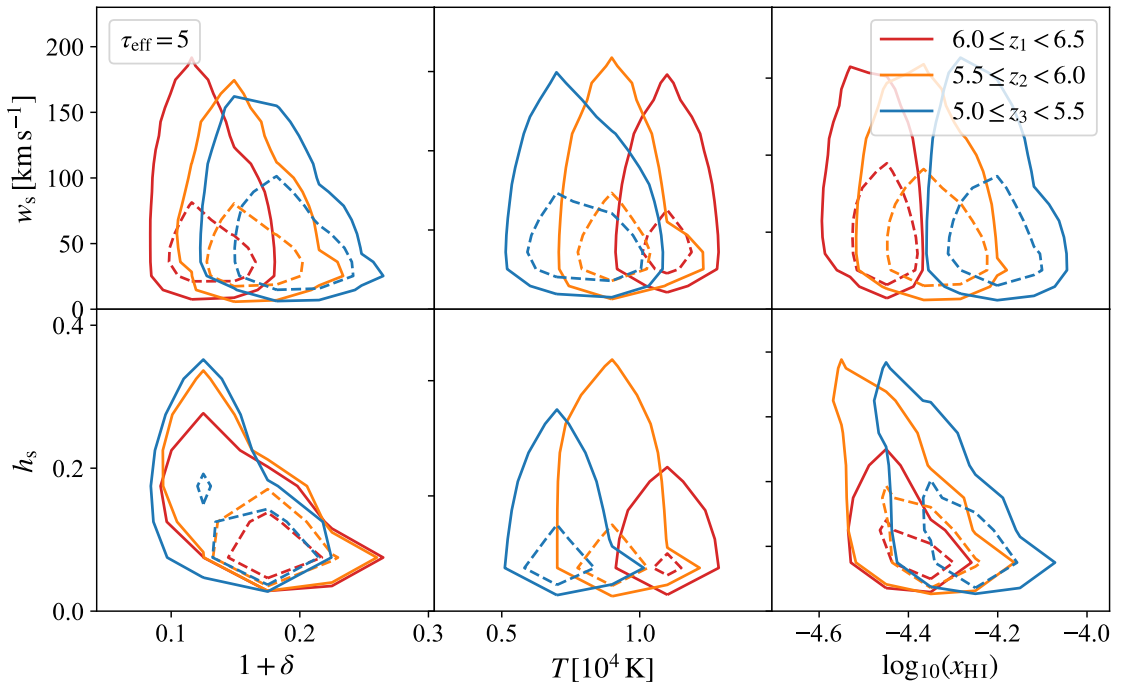


Figure B.9. Same as Fig. 5.11 except that results are shown the *default* model with a scaled effective optical depth $\tau_{\text{eff}} = 5$ here. Here, the correlations between the spike properties and δ and x_{HI} are similar to that observed in the underlying *default* model.

Declaration of Authorship

Hereby, I declare that I have composed the presented paper with the title "Lyman- α transmission spikes as probes of cosmic voids, the intergalactic medium, and reionization" independently on my own and without any other resources than the ones indicated. All thoughts taken directly or indirectly from external sources are properly denoted as such. This paper has neither been previously submitted to another authority or an examination committee nor has it been published yet.

Potsdam, March 5, 2021

F.P. Emmerich
.....